

# **EVALUATION OF OPTICAL TECHNIQUES APPLIED TO ONLINE TURBOMACHINERY BLADE VIBRATION MEASUREMENTS**

---

by  
**Benjamin Gwashavanhu**

Submitted in partial fulfilment of the requirements for the degree Master of Engineering in the  
Faculty of Engineering, Built Environment and Information Technology,

University of Pretoria

Pretoria

**July 2015**

# EVALUATION OF OPTICAL TECHNIQUES APPLIED TO ONLINE TURBOMACHINERY BLADE VIBRATION MEASUREMENTS

Benjamin Gwashavanhu

Supervisors: Professor P.S. Heyns & Dr A.J. Oberholster

University of Pretoria

Department of Mechanical and Aeronautical Engineering

Degree: Master of Engineering

## Abstract

Understanding the dynamic characteristics of blades is important in the online condition monitoring of turbomachinery. Conventionally contact methods are used for this purpose. However improvements in technology now allow for the use of non-contact methods. Contact measurement techniques for turbomachinery blade vibration analysis typically involve the use of strain gauges and accelerometers. These present some complications when analyzing rotating machinery. Being contact in nature, mass loading can affect the integrity of measurements captured. Turbomachines typically operate under the adverse conditions of high temperatures, high flow rates and sometimes wet environments. This significantly reduces the life of contact transducers installed to capture the blade dynamics. Installation of telemetry systems for signal transmission is also necessary. In addition to being invasive and expensive, telemetry systems can introduce electrical noise.

These factors make it desirable to explore the applicability of various optical non-contact methods for analyzing turbomachine blade vibrations, such as Laser Doppler Vibrometry (LDV) and photogrammetry. Both techniques have been successfully used to analyze vibrations of structures. Photogrammetry is a full-field measurement technique which allows for non-intrusive simultaneous measurement of vibrations at different locations on a blade. This is particularly important for the updating of numerically developed models of structures, investigation of structural global dynamics, and more effective localization of damage. Accelerometers have been used to validate a variation of photogrammetry, three dimensional point tracking (3DPT), for rotational applications and discrepancies attributed to the contact nature of accelerometers were observed. To build confidence in the use of 3DPT as a non-contact method for analyzing rotating machines, it is necessary to investigate how well it correlates with various non-contact methods. Through such an investigation aspects that need to be addressed when using 3DPT to analyse turbomachines can be identified. If reliable measurements can be obtained using this technique, further

investigations such as online damage detection and characterization in rotating structures can be conducted.

In this study Tracking Laser Doppler Vibrometry (TLDV) and 3DPT are used as non-contact methods to investigate the online vibrations of a turbomachine test rotor. To employ TLDV on the test rotor, the dynamics of the scanning mirrors of a Polytec Scanning Vibrometer (PSV) are characterized using a frequency response approach. Look-up tables are constructed to provide the necessary phase angle compensation for the two signals supplied to the mirrors, to obtain a circular scanning path. Photogrammetric 3DPT is then validated by tracking the TLDV laser spot focused on one of the test rotor blade using high speed cameras, and comparing the 3DPT measurements to TLDV blade out-of-plane vibration measurements. The correlation between the two non-contact measurement techniques is presented. This establishes the validity of the employed scanning system, and also serves to show how well the two non-contact methods correlate with each other, when investigating dynamics of turbomachinery blades. 3DPT is then used to analyze the responses of the test rotor blades under excitation. Various Operational Deflection Shapes (ODSs) of the blades are identified and the results obtained are presented.

The use of ODSs obtained from 3DPT to investigate irregularities along turbomachinery blades is also presented. This information is used to show that ODSs captured using 3DPT can be used to online detect and localize blade damage in turbomachines.

**Keywords:** *Non-contact vibration analysis; Photogrammetry; 3D point tracking; Digital image correlation; Tracking laser Doppler vibrometry; Turbomachinery blades; Condition monitoring; Finite element modelling; Operational deflection shapes; Damage detection.*

## ACKNOWLEDGEMENTS

I would like to thank following people for their help in the completion of this work:

- My supervisors, Professor P.S. Heyns and Dr A.J. Oberholster, for presenting me with an opportunity to do this work, and for their guidance and assistance throughout the duration of this study.
- Special thanks to Mr Dave Reinecke from CSIR for letting us use their SA4 Photron high speed cameras.
- Mr Breitenbach and Mr Booysen for their assistance in experimental setting up and testing.
- Mr Gautam Ranjit for his assistance during after-hours experimental testing, his assistance in getting required equipment for testing, and his ideas in better experimental testing procedures.
- Mr Dawie Diamond for assistance in developing the experimental setup used for this study.
- My family for the continued support throughout the duration of my studies.

## TABLE OF CONTENTS

|   |     |
|---|-----|
| ACKNOWLEDGEMENTS .....  | iii |
| GLOSSARY .....  | vi  |
| ABBREVIATIONS .....   | vi  |
| SYMBOLS.....  | vi  |
| GREEK SYMBOLS.....  | vii |
| CHAPTER 1: INTRODUCTION.....  | 1   |
| 1.1    PROBLEM STATEMENT.....   | 1   |
| 1.2    LITERATURE STUDY .....   | 3   |
| 1.2.1    CONTACT AND NON-CONTACT METHODS FOR VIBRATION ANALYSIS .....                     | 3   |
| 1.2.2    PHOTOGRAMMETRY .....   | 4   |
| a)    PRINCIPLES OF DIC AND 3DPT .....  | 4   |
| b)    CALIBRATION.....  | 5   |
| c)    USE OF PHOTOGRAMMETRY FOR DYNAMIC ANALYSIS.....                                     | 5   |
| d)    ASPECTS TO CONSIDER WHEN USING PHOTOGRAMMETRY FOR DYNAMIC ANALYSIS .....            | 8   |
| 1.2.3    LASER DOPPLER VIBROMETRY .....   | 9   |
| a)    TRACKING LASER DOPPLER VIBROMETRY .....   | 9   |
| b)    SELF-TRACKING LASER DOPPLER VIBROMETRY (STLDV).....                                 | 11  |
| c)    ASPECTS TO CONSIDER WHEN USING TLDV .....   | 12  |
| 1.2.4    DAMAGE DETECTION AND CHARACTERISATION.....                                       | 15  |
| a)    MODAL BASED APPROACHES FOR DAMAGE DETECTION .....                                   | 15  |
| 1.3    SCOPE OF RESEARCH.....   | 17  |
| 1.4    DOCUMENT OVERVIEW .....  | 19  |
| CHAPTER 2: EXPERIMENTAL SETUP AND FE MODELLING OF A BLADED DISK.....                      | 20  |
| 2.1    INTRODUCTION .....   | 20  |
| 2.2    EXPERIMENTAL SETUP .....   | 20  |
| 2.3    FINITE ELEMENT MODELLING OF THE BLISK.....   | 22  |
| 2.4    FINITE ELEMENT MODEL UPDATING (FEMU) .....   | 23  |
| 2.4.1    COMPARISON OF EXPERIMENTAL MODAL PARAMETERS TO ANALYTICAL MODAL PARAMETERS ..... | 25  |
| 2.4.2    MODEL UPDATING PROCEDURE .....   | 28  |
| 2.4.3    DETERMINATION OF THE EXCITATION FREQUENCIES USING A CAMPBELL DIAGRAM .....       | 32  |
| CHAPTER 3: VERIFICATION OF 3DPT RESULTS USING TLDV .....                                  | 35  |
| 3.1    INTRODUCTION .....   | 35  |

|  |  |    |
|--|--|----|
| 3.2  | CONTROL OF THE POSITION OF THE LASER BEAM.....   | 35 |
| 3.3  | INVESTIGATION OF THE PRESENCE OF MISALIGNMENT .....  | 46 |
| 3.4  | VALIDATION OF 3DPT AS A METHOD FOR CHARACTERIZING THE DYNAMICS OF ROTATING STRUCTURES..... | 49 |
| 3.4.1  | EXPERIMENTAL SETUP .....   | 49 |
| 3.4.2  | PHOTOGRAMMETRIC DISPLACEMENT MEASUREMENTS OF A LASER DOT FOCUSED ON A ROTATING BLADE ..... | 53 |
| 3.4.3  | TLDV DISPLACEMENT MEASUREMENTS .....   | 56 |
| 3.4.4  | COMPARISON OF 3DPT DISPLACEMENT MEASUREMENTS TO TLDV DISPLACEMENTS.....                    | 57 |
| CHAPTER 4: USE OF 3DPT FOR ANALYSING THE DYNAMICS OF A ROTATING BLISK .....  |  | 64 |
| 4.1  | INTRODUCTION .....   | 64 |
| 4.2  | BLISK DYNAMIC ANALYSIS USING 3DPT.....   | 64 |
| 4.3  | INVESTIGATION OF RESPONSE IRREGULARITIES ALONG A BLADE DUE TO LOCALIZED EXCITATION .....   | 68 |
| 4.4  | USE OF ODSs TO DETECT IRREGULARITIES ALONG BLADES .....                                    | 72 |
| CHAPTER 5: CONCLUSIONS AND RECOMMENDATIONS.....                              |  | 76 |
| 5.1  | CONCLUSIONS .....  | 76 |
| 5.2  | RECOMMENDATIONS AND FUTURE WORK.....   | 77 |
| REFERENCES .....   |  | 78 |
| APPENDIX A: MODAL 2 BLISK NATURAL FREQUENCIES AND DAMPING FACTORS.....       |  | 82 |
| APPENDIX B: VARIATIONS OF MODE NATURAL FREQUENCIES WITH YOUNG'S MODULUS..... |  | 83 |
| APPENDIX C: VARIATIONS OF MODE NATURAL FREQUENCIES WITH DENSITY .....        |  | 84 |
| APPENDIX D: VARIATIONS OF MODE NATURAL FREQUENCIES WITH POISSON'S RATIO..... |  | 85 |

## GLOSSARY

### ABBREVIATIONS

| <b>Abbreviation</b> | <b>Description</b>                           |
|---------------------|--|
| 3DPT                | Three Dimensional Point Tracking             |
| CSLDV               | Continuous Scanning Laser Doppler Vibrometry |
| DIC                 | Digital Image Correlation                    |
| EO                  | Engine order                                 |
| FE                  | Finite Element                               |
| FEM                 | Finite Element Model                         |
| FEMU                | Finite Element Model Updating                |
| FFT                 | Fast Fourier Transform                       |
| FRF                 | Frequency Response Functions                 |
| HCF                 | High Cycle Fatigue                           |
| LCF                 | Low Cycle Fatigue                            |
| LDV                 | Laser Doppler Vibrometry                     |
| MAC                 | Model Assurance Criterion                    |
| ND                  | Nodal Diameter                               |
| N-ODS               | Normalized Operational Deflection Shape      |
| ODS                 | Operational Deflection Shape                 |
| RMS                 | Root Mean Square                             |
| R-ODS               | Residual Operational Deflection Shape        |
| SLDV                | Scanning Laser Doppler Vibrometry            |
| TLDV                | Tracking Laser Doppler Vibrometry            |

### SYMBOLS

| <b>Symbol</b>                       | <b>Description</b>  |
|-------------------------------------|---|
| A                                   | Area  |
| $C(x, y, x^*, y^*)$                 | Normalized cross-correlation  |
| $C_c$                               | Circularity constant  |
| $d_s$                               | Mirror separation distance  |
| $E$                                 | Elastic Modulus   |
| $F(x, y)$                           | Un-deformed grey scale level  |
| $G(x^*, y^*)$                       | Deformed grey scale level   |
| $I$                                 | Moment of Inertia   |
| $L$                                 | Length  |
| $N_b$                               | Number of blades  |
| $\{\Delta p\}$                      | Change in material properties   |
| P                                   | Perimeter   |
| PSV                                 | Polytec Scanning Vibrometer   |
| $R(x, y, x^*, y^*)$                 | Intensity value difference  |
| $r_s$                               | Scanning radius   |
| $\frac{\partial R_j}{\partial P_i}$ | Change in natural frequency associated with mode $j$ with change in parameter $i$ |
| S                                   | Sensitivity matrix  |
| t                                   | Time  |
| $x_{0m}$                            | x-direction translational misalignment  |
| $x_s$                               | x-position of laser beam on target  |
| $(x, y)$                            | Un-deformed point coordinates   |
| $(x^*, y^*)$                        | Deformed point coordinates  |

|          |  |
|----------|--|
| $y_s$    | y-position of laser beam on target     |
| $y_{0m}$ | y-direction translational misalignment |
| $z_0$    | Perpendicular distance from target     |
| $z_s$    | z-position of laser beam on target     |

## GREEK SYMBOLS

| <b>Symbol</b>     | <b>Description</b>                            |
|-------------------|---|
| $\alpha_n$        | Natural frequency boundary condition constant |
| $\{\varepsilon\}$ | Residual                                      |
| $\theta_{sx}(t)$  | X-mirror scanning angle                       |
| $\theta_{sy}(t)$  | Y-mirror scanning angle                       |
| $\theta_{xm}$     | x-direction angular misalignment              |
| $\theta_{ym}$     | y-direction angular misalignment              |
| $\nu$             | Poisson ratio                                 |
| $\rho$            | Density                                       |
| $\phi_C$          | Complex mode shape                            |
| $\phi_R$          | Real mode shape                               |
| $\phi_s$          | Initial phase                                 |
| $\varphi_{sx}(t)$ | X-mirror scanning amplitude                   |
| $\varphi_{sy}(t)$ | Y-mirror scanning amplitude                   |
| $\omega$          | Rotational frequency                          |
| $\omega_i$        | i-th natural circular frequency               |
| $\Omega_s$        | Total rotational frequency of target          |

## CHAPTER 1: INTRODUCTION

In this chapter, background information on turbomachinery and the need for effective condition monitoring techniques is presented. A literature review focusing on contact and non-contact methods for online vibration measurement of turbomachinery blades is also presented. Information on possible damage detection and characterization techniques, that can be exploited using captured structural vibratory data are described. Concluding this chapter is the scope of research and a document overview.

### 1.1 PROBLEM STATEMENT

Turbomachines and rotating machinery form part of a vast number of machines used in the engineering industry. Condition monitoring and maintenance of these machines is inherently important if failures due to blade associated problems are to be avoided. Failures in turbomachines occur due to a number of reasons, which include lightning strikes in wind turbines and bearing associated problems in gas turbines. For these structures, blade failure can result in the total loss of the whole system. Figure 1 shows a typical distribution of damage types encountered in wind turbine power generation from an investigation conducted in 2012 from official or news reports by Chou et al. (2013).

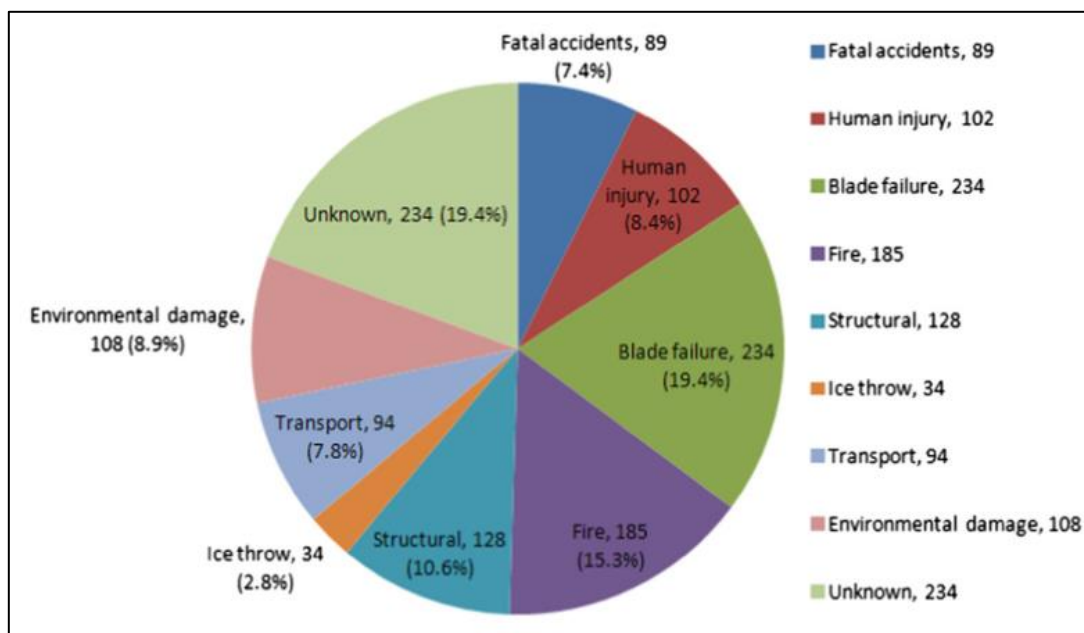


Figure 1: Damage types in wind turbines (Chou et al., 2013)

By looking at the different damage types that can occur in wind turbines as illustrated in Figure 1, blade failure is the most commonly known type of damage (19.4%). This highlights the importance of understanding the dynamics of turbomachinery blades.

According to Kumari et al. (2014), failure in the blades can generally be classified as fatigue failure or creep rupture. The fatigue can either be Low Cycle Fatigue (LCF) or High Cycle Fatigue (HCF). In blades, the fatigue is induced by cyclic loading associated with various forms of excitation that the blades are exposed to as they rotate. Madhavan et al. (2014) reported that as much as 42% of turbine failures are a result of this fatigue. To understand

failure modes resulting from fatigue, development of techniques that can be used to investigate and analyse the vibrations in the blades while they are in operation is necessary.

A wide range of maintenance strategies can be put in place to avoid blade failures. These can either be corrective or preventive strategies. Corrective maintenance is usually not acceptable, since in most cases a blade failure will lead to total structure loss. As alternatives, design out maintenance and preventive maintenance strategies are usually employed. Design out maintenance, entails designing components to ensure that failures are avoided.

Re-designing systems to eliminate turbomachine blade modes of failure requires an understanding of the online dynamics of the systems. This also applies to condition monitoring of rotating machines as part of a preventative maintenance strategy. With Condition Based Maintenance (CBM), not only are downtime related costs and costs due to failure avoided, but also machines are monitored in real-time and maintenance can be scheduled when required.

In light of the advantages inherent to condition monitoring, it is imperative to establish and develop methodologies that can be used to acquire the information pertaining to the integrity of blades. This information can be obtained by investigating the dynamics associated with turbomachines as they operate. A number of techniques have previously been developed and successfully implemented for these purposes. Traditionally these have been contact measurement techniques using accelerometers and strain gauges. Although these techniques can be adequately used for vibration analysis with limited costs, they present significant complications, particularly in online condition monitoring applications.

With advancements in technology, non-contact methods for vibration analysis are now available and are becoming increasingly popular. Among these methods are blade-tip timing techniques, Laser Vibrometry, and the use of high speed cameras. Although these techniques have been available for quite some time now, a significant amount of research still needs to be conducted to establish the applicability and accuracy of some of these techniques. The extent to which these methods can be used to investigate the dynamics of rotating machines is currently receiving substantial attention, as there is always a necessity to formulate more robust and easier approaches that simplify the condition monitoring of machines. The amount of information that can be extracted from measurements conducted using these non-contact methods, and how they correlate with other measurement techniques is the focus of this research. This has been done with the aim of developing and exploring non-contact methodologies for dynamic analysis, specifically applied to rotating turbomachinery blades.

## 1.2 LITERATURE STUDY

### 1.2.1 CONTACT AND NON-CONTACT METHODS FOR VIBRATION ANALYSIS

Determining the vibration characteristics of rotating turbine blades can be achieved by using contact or non-contact methods. Contact methods include the use of accelerometers and strain gauges, mounted onto the blades. These contact methods are becoming less popular in investigating rotating structures, primarily due to disadvantages which include: mass loading of the structure, possible introduction of noise when transmitting the signals, and limited sensor lifespan. In addition, the complex installation procedures involved, such as the telemetry of the slip ring systems used for strain gauges, are likely to interfere with the turbine blade assembly.

Conversely, non-contact methods are non-intrusive, and they do not require telemetry systems for the data transmission, which potentially make them suitable alternatives. Castellini et al. (2006) investigated the effect of mass loading when accelerometers were used to capture data. The damping factors and natural frequencies obtained from accelerometer and Scanning Laser Doppler Vibrometry (SLDV) measurements were compared during a modal analysis of an automotive engine cover. It was observed that due to the mass loading and local stiffening introduced by the accelerometers, a frequency shift of 0.7% for one of the modes resulted.

Non-contact optical methods for vibration measurement have become very popular over the years. A considerable amount of research is currently being done to improve a number of these optical techniques. Measurements captured are either targeted at properties such as light intensity, or other aspects like distance from an optical sensor. This then means that a clear line of sight from the instruments to the target under investigation is required. These optical based techniques include photogrammetry, Laser Doppler Vibrometry (LDV), laser interferometry, Moiré techniques, and white-light interferometry, among others. Whilst specific techniques are more suited for various situations, photogrammetry applications are most popular in cases where full-field measurements need to be captured. Displacement measurements for a number of points can be simultaneously captured using 3DPT if circular markers are attached to the surface of a structure. If however a speckle pattern is applied to the surface of the structure strain distributions on the surface can be obtained through Digital Image Correlation (DIC). In literature, DIC is commonly used to refer to either of the variations of photogrammetry (DIC and 3DPT).

Non-contact techniques are also applicable to most tests involving complex material types and configurations. Very light structures can be analysed without any mass loading, and measurements can be captured by simply applying a pattern on delicate surfaces such as human skin. A full-field measurement approach can be easily adopted, without the need for one to know the locations of the nodes or nodal lines of a structure before conducting an analysis. This is a prerequisite when accelerometers are to be attached to a structure, as attachment of a sensor on a nodal line will result in no data capture by that sensor.

3DPT and TLDV are two non-contact optical techniques that can be used to investigate rotating structures. To illustrate how these techniques are used, and how widely they have been of assistance in the monitoring of structures, both techniques will be described, in detail, in the following sections.

## 1.2.2 PHOTOGRAMMETRY

### a) PRINCIPLES OF DIC AND 3DPT

DIC and 3DPT utilise a stereoscopic setup of two cameras to capture a series of images of a surface of a structure as it vibrates. By positioning the two cameras at a certain distance from each other, stereo photographs of the object can be obtained. Stereo photographs are two photographs of an object from slightly different angles which, when viewed together, will provide a 3D representation of the object. After the images have been captured by the cameras, digital image processing is done. This involves subjecting the numerical representation of the image to operations which typically include changing the contrast and minimising the noise in the images. This forms the initial processing of the image pairs.

The non-contact technique relies on image processing and analysing software being able to either distinguish different pixels on digital images of a structure under investigation (DIC), or detecting circular markers attached to various points on the structure (3DPT). For DIC, typically a random black and white speckle pattern is applied on the surface of the structure. This pattern ensures that the gray scale values of the different pixels are different. In a dynamic analysis, subsequent images as the structure deforms or vibrates are captured using high speed cameras. Assuming that the light intensities on each pixel do not change significantly during the process, the displacement profile of a subset on an image is found by searching for an area with the same light intensity distribution within the subset, in the series of captured images. Thus a correlation process is done to match subsets from one image to the next.

According to Yoneyama & Murawasa (2012), a number of functions exist that can be used to perform this matching process. Typically one can use the following approaches:

1. The magnitude of intensity value difference  $R$  which is normally used.

$$R(x, y, x^*, y^*) = \sum |F(x, y) - G(x^*, y^*)| \quad (1.1)$$

2. The normalized cross-relation  $C$ .

$$C(x, y, x^*, y^*) = \left( \frac{\sum F(x, y)G(x^*, y^*)}{\sqrt{\sum F(x, y)^2 G(x^*, y^*)^2}} \right) \quad (1.2)$$

In the above expressions,  $(x, y)$  and  $(x^*, y^*)$  are the un-deformed and deformed point coordinates respectively.  $F(x, y)$  and  $G(x^*, y^*)$  are the gray scale levels within the subset containing the point. The displacement components are then obtained by extracting the best post deformation coordinates,  $(x^*, y^*)$ , which will either minimize function  $R(x, y, x^*, y^*)$  or maximize  $C(x, y, x^*, y^*)$ .

The correlation scheme in Figure 2 is typically used to perform three-dimensional displacement measurements.

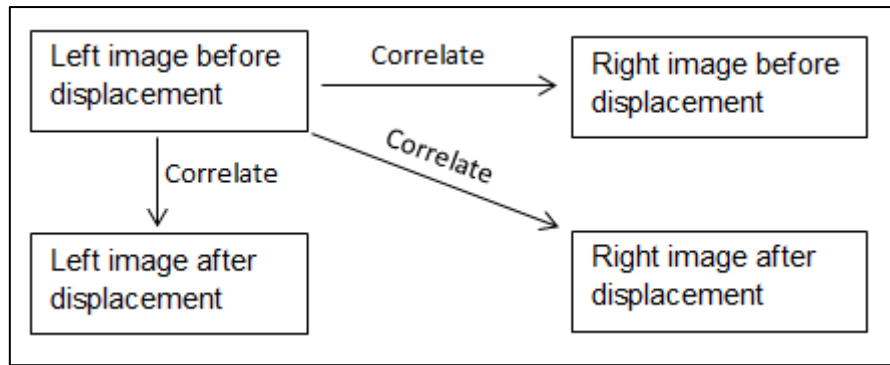


Figure 2: Digital image correlation scheme (Rastogi, 1997)

For 3DPT, the photogrammetry software detect circular markers on the structure, and a stereoscopic analysis approach similar to the one presented in Figure 2 is used to obtain displacement profiles of the points where these markers are attached.

## b) CALIBRATION

A calibration of the two high speed cameras has to be done prior to the application of a loading to the structure of interest. A calibration target is used for the calibration process. This can either be a standard panel developed by the image processing and correlating software developers, or a simple individually developed white panel with black markers on it. After the cameras have been mounted, the calibration target is typically tilted and rotated in the volume of space where the structure of interest will be positioned for investigation. Images of the target are captured, one pair at a time, to obtain various perspective views of the calibration target.

The calibration process establishes the camera's intrinsic parameters, which include the image centre, the image skew and, the scale and distortion parameters. Distortion entails cases similar to that whereby straight lines on the object of interest are depicted as curved lines on the sensors. This typical case of lens distortion is very common in wide-angle lenses. Errors due to lens distortion will affect both the spatial positions of the points under investigation, and the measured displacements (Yoneyama, 2006). This is so because photogrammetry measurements are captured through the detection of movement of a specimen surface.

Also obtained from the calibration are extrinsic parameters. These include the pinhole locations of the cameras and the orientations of the cameras relative to the target. These parameters are also needed for accurate determination of point displacements and structural deformations. After the calibration, the actual structure under investigation can then replace the calibrating panels.

## c) USE OF PHOTOGRAMMETRY FOR DYNAMIC ANALYSIS

Photogrammetry has been used in a wide variety of applications, some of which will be described in this section. Its capabilities in dynamic analysis and how different strategies can be implemented to improve the performance of either DIC or 3DPT are also discussed below.

Compared to other optical methods, photogrammetry does not require a complicated optical system. According to Yoneyama (2006), no phase analysis of fringe patterns and phase unwrapping is required, which is usually the case with other optical methods that focus on

the interference of light waves. Subsequently, measurements are easily obtained with DIC and 3DPT. Using two cameras allows for both the in-plane and out of plane displacement measurement. Also, a full range of strain distribution measurements can be done with very good accuracy. Luyckx et al. (2014) showed that the scatter values of strain measurements on the surface of specimen are typically below 0.3%.

Using this technique, advanced design methods such as Reverse Engineering (RE) in which models of a product are developed by digitally recognizing its physical nature, can be used. According to Alberti et al. (2008), these advanced design methods require acquisition systems that are capable of reproducing geometric profiles with high accuracy and repeatability. These authors were able to show that basic 3D shape measurements of an object can be done using DIC principles and stereoscopic vision. They did this by comparing results obtained through the use of cameras to those obtained through the shadow moiré technique and a conoscopic-holography technique. Thus they illustrated that DIC is a valid technique to compute shapes of complex objects.

As DIC allows contour and displacement measurement of a deforming surface, it can be used to investigate mechanical material properties parameters such strain distribution. According to Siebert et al. (2009), DIC can be successfully and accurately implemented in material testing and fracture mechanics to obtain the location and amplitudes of the maximum strain, the global strain distribution, and the behaviour of crack growth. In these applications, the number of pixels in the captured image limits the precision of the of the measurements and also the spatial resolution (Crammond et al., 2011). Typically, DIC systems will have a dynamic range from static to more than 100 kHz, a micron to a meter displacement range, a micron resolution and about 0.01% strain (Dantecdynamics.com, 2015).

The full-field measurement capabilities of DIC make the approach a superior measurement technique when compared to the conventional modal testing methods. As an alternative to point-wise frequency response functions, Wang et al. (2012) demonstrated that domain-wise responses obtained from DIC measurements can be used to identify modal properties of a structure. Definition of image processing techniques on the planar domains of a specimen allowed them to extract shape features from displacements measured along the surface. By using image decomposition techniques to analyse the captured 3D data, the authors were able to show that the redundant results, from the full-field data, can be discarded and frequency response functions at various points obtained from determined object shape features. In addition to showing how well DIC can represent the raw data efficiently, they showed how the noise in the DIC measurements can be minimized.

According to Warren et al. (2011), although SLDV can be used to capture measurements over a wide frequency range in a non-contact manner, DIC proves to be more appropriate for applications that involve large displacement amplitude vibrations. SLDV is sensitive to large in-plane displacements measurements as it becomes more difficult to pinpoint the laser on a fixed desired target location. Also with continuous SLDV, the higher the scanning rate, the more the speckle noise in the system (Chiariotti et al., 2014). DIC on the other hand favours large displacement, low frequency vibration measurements, which are quite challenging procedures to achieve using either SLDV or even accelerometers. Compared to accelerometers and LDV in general, in which multiple modes are determined over a broad

frequency range, at discrete points, DIC captures the responses of all the points simultaneously.

Helfrick et al. (2009) illustrated that the DIC measuring technique is applicable to rotating turbine blades. The authors used the technique to capture the out-of-plane motion of rotating blades, and illustrated that the approach can be used to capture ODS. For their investigation, they used the ARAMIS DIC system to analyse vibrations of a small desk fan. ARAMIS is image processing software developed by Gesellschaft für Optische Messtechnik (GOM), which yields strain measurements by analysing captured images. The desk fan can be appropriately categorized as a turbomachine. To prevent motion blur resulting from a too long exposure time set on the cameras, the use of a stroboscope synchronized with the cameras proved to be a viable approach. In addition to capturing the ODS, they were also able to determine the out-of-plane displacements as a function of the rotation angle. In the work done by these authors, results were not validated using any other measurement techniques.

Warren et al. (2011) extended the work done on a small desk fan by quantifying the performance of DIC in investigating a 1.17 m diameter rotating wind turbine. In their work, they managed to successfully capture optical measurements for over 10,000 target points. They used LDV in a forced normal mode stationary testing. MAC values of 99.3% were obtained between the DIC and the LDV results in this stationary investigation. For a rotational test, they compared the auto-power spectra of accelerometer results to that of DIC results. Although a good correlation was obtained between the contact and non-contact method, differences were noticed for the high frequencies. They attributed these differences to errors introduced by noise from the slip rings, the optical system noise floor, cross-axis sensitivities of the accelerometers, and also the useful measurement ranges for the two methods. Thus the use of a contact method to investigate the applicability of DIC for analysing turbomachines does influence the correlation of the results captured. Part of this research focuses on the use of a non-contact method to investigate the integrity of the results captured using DIC. Thus in so doing, errors introduced due to use of a contact method can be eliminated, and better information obtained on how well DIC is applicable to online monitoring of turbomachines.

Dynamic point tracking using DIC has also been successfully used by Javad et al. (2013) in analysing helicopter rotors. An operational modal analysis was conducted, and the measured data indicated that for the rotors, harmonics of the blade passage frequency dominated the motion. In a similar investigation Lundstrom et al. (2013) collected operational data of the rotor of a Robinson R44 helicopter, and they managed to prove that three dimensional point tracking (3DPT) and stereophotogrammetry is a robust measurement technique for analysing small rotating structures.

Line of sight of the rotating structure is typically required if the cameras are to be able to track markers attached to the structure. Avitabile et al. (2014) applied DIC in conjunction with real time operating data expansion techniques in predicting full-field dynamic strain. They successfully showed that in cases where there is not a clear line of sight, operating data expansion processes can still be used to capture full-field displacements.

#### d) ASPECTS TO CONSIDER WHEN USING PHOTOGRAMMETRY FOR DYNAMIC ANALYSIS

In addition to motion blur when analysing rotating structures, a few other issues also have to be addressed when using photogrammetry as a vibration analysis technique. When reporting the recent progress made in using DIC, Pan (2010) noted that the errors in measured DIC displacements are closely related to the quality of the speckle pattern applied on the structure. As mentioned earlier, displacement profiles are obtained by searching a deformed image for a subset or target with an intensity pattern which is most similar to that of a reference subset. This implies that adequate intensity variation in the surface subsets is a requirement if reliable and accurate displacement measurements are to be obtained. Good intensity variation will ensure unique and consistent identification of a subset in the captured sequence of images.

A parameter that can be used to globally assess the quality of a speckle pattern is the mean intensity gradient. Pan (2010) suggested Equation (1.3) below for determining this parameter.

$$\delta_f = \frac{\sum_{i=1}^W \sum_{j=1}^H |\nabla f(x_{ij})|}{W \times H} \quad (1.3)$$

In the above expression, W and H are the width and the height of the image in pixels. The local intensity gradient vector modulus  $|\nabla f(x_{ij})|$ , can be determined using Equation (1.4).

$$|\nabla f(x_{ij})| = \sqrt{f_x(x_{ij})^2 + f_y(x_{ij})^2} \quad (1.4)$$

Defined at pixel  $x_{ij}$ , x- and y-direction first order intensity derivatives,  $f_x(x_{ij})$  and  $f_y(x_{ij})$ , are computed using a gradient operator represent. With the mean intensity gradient of the entire speckle pattern, the Sum of Square of Subset Intensity Gradient (SSSIG) within a local subset of N by N pixels can then be estimated using Equation (1.5).

$$SSSIG = \sqrt{\sum_{i=1}^N \sum_{j=1}^N [f_x(x_{ij})]^2} \cong N \times \delta_f \quad (1.5)$$

According to Pan (2010), if the displacement difference between the DIC estimated displacement and the exact displacement pixel  $x_{ij}$  is denoted by  $u_e$ , then the standard deviation of the measured displacement can be estimated using Equation (1.6).

$$std(u_e) \cong \frac{\sqrt{2}\sigma}{SSSIG} \quad (1.6)$$

In the above expression,  $\sigma^2$  is the magnitude of white noise. The DIC displacement standard deviation error is therefore inversely proportional to SSSIG, which is the product of the subset size N and the mean intensity gradient of the speckle pattern. Thus Pan (2010) concluded that the speckle pattern with a large mean intensity gradient produces the least standard deviation error in the captured measurements.

Zappa et al. (2014) categorised the parameters that affect the performance of DIC into static and dynamic parameters. With static parameters, one should consider the image resolution, blurring, lighting conditions, and the parameters, such as the functions maximized or minimized for the correlation, used when processing the images. The dynamic parameters include the motion characteristics of the structure, essentially the instantaneous velocity and the shutter time used when capturing the images. Techniques that one can use to estimate the uncertainty of DIC measurements in a dynamic application are also proposed by these authors.

According to Helfrick et al. (2009), for events requiring a lot of light and a very short shutter time, a stroboscope can be used, as generally the flash duration of a stroboscope is less than the smallest possible shutter speed of a high speed camera.

### 1.2.3 LASER DOPPLER VIBROMETRY

LDV is another optical technique that can be used for the analysis of vibrating structures. It is a non-contact transducer, which functions by directing a laser beam onto a structure and subsequently detecting the reflected scattered beam. Whilst LDVs are usually used to capture velocities through transformation of a frequency shift (Doppler shift) into a voltage which is proportional to velocity, a PSV 300 can directly capture displacements by decoding a phase shift, (Johansmann et al., 2015). According to these authors the phase or displacement noise exhibits white noise characteristics of being constant with frequency, but this is not the case for the velocity noise which increases with frequency. This implies that it is more favourable to use phase demodulation for low frequency measurements, as opposed to frequency demodulation.

For rotating structures LDV can be used in an Eulerian approach, in which the laser beam is fixed in space, and the blades sweep through the beam as they rotate. The shortcoming of using this approach is that one can only acquire a short burst of samples once every revolution of the blade.

According to Oberholster & Heyns (2011), use of time domain and non-harmonic Fourier analysis becomes necessary when an Eulerian approach is used. This approach is necessary, because the short data samples cannot be analysed using standard frequency domain signal processing techniques. Additionally, the relative motion that occurs between the beam and the rotating turbine blade, introduces speckle noise. This is most apparent in the small vibrations associated with low rotational speeds. A change in point of focus of the laser beam results in the photo detector receiving a changing speckle pattern of the reflected signal from the blades. Martarelli & Ewins (2006) stipulated that this will introduce speckle noise in the LDV captured results.

LDV can also be used to analyse rotating structures in a Lagrangian approach. This is described in detail in the following section.

#### a) TRACKING LASER DOPPLER VIBROMETRY

A scanning Laser Vibrometer has two mirrors (X mirror and Y mirror) that are mounted orthogonally to each other. The presence of these two mirrors allows a scanning head to be used for single point scans and also for continuous scanning over the surface of a structure. The scanning capability of a scanning head can be exploited by configuring the laser system to track a specific point on a blade of a turbomachine. This ensures that one obtains

continuous data as a blade rotates through  $360^\circ$ , provided that an unobstructed view of the blades is possible. The use of this Lagrangian reference frame approach is generally known as TLDV. Figure 3 illustrates the functioning principles of the scanning head of a scanning Laser Vibrometer.

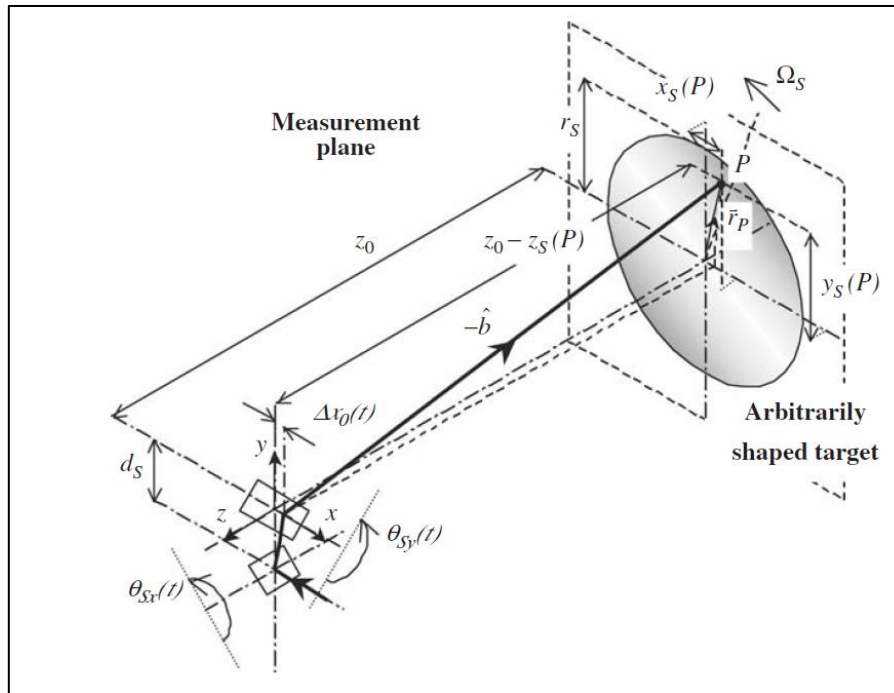


Figure 3: Functionality of a SLDV (Halkon & Rothberg, 2006a)

To obtain a circular scanning path on the target, two sinusoidal voltage signals, which are  $90^\circ$  out of phase, will have to be simultaneously supplied to the mirrors. However, as explained by Halkon & Rothberg (2006a), there is a need to account for the difference in the distances of the two mirrors to the point of interest on the target. Thus they derived Equations (1.7) and (1.8), for calculating the amplitudes of the scan voltages supplied to the X mirror ( $\varphi_{s_x}(t)$ ) and the Y mirror ( $\varphi_{s_y}(t)$ ).

$$\varphi_{s_x}(t) = 0.5 \tan^{-1}\left(\frac{r_s}{z_0 + d_s}\right) \quad (1.7)$$

$$\varphi_{s_y}(t) = 0.5 \tan^{-1}\left(\frac{r_s}{z_0}\right) \quad (1.8)$$

For any particular circular scanning radius  $r_s$ , using a scanning head with mirrors separated by a distance  $d_s$ , and a target that is a perpendicular distance  $z_0$  from the centres of the two mirrors, the scan voltage amplitudes to the mirrors must be unequal.

The circular scan profiles can then be obtained by using drive signals of the form given in Equation (1.9) and (1.10).

$$\theta_{s_x} = -\varphi_{s_x} \cos(\Omega_s t + \phi_s) \quad (1.9)$$

$$\theta_{s_y} = \varphi_{s_y} \cos(\Omega_s t + \phi_s) \quad (1.10)$$

The drive signal to the X mirror is given by  $\theta_{s_x}$  and that to the Y mirror by  $\theta_{s_y}$  for a circular scan of frequency in Hertz given by  $\Omega_s$ . A phase correction in the two signals  $\phi_s$  might also be necessary to get a perfect circular scan.

When this approach is used at high rotational speeds, the response of the X-Y mirrors is such that the circular scanning path is distorted into an elliptical shape. This results from galvanometric motors and mirrors' inertial effects, and also phase delays in the scanning system's drive components responses (Di Maio & Ewins, 2010). After considering these factors which influence the dynamic performance of a scanning system Di Maio & Ewins (2010) stipulated that it is usually necessary to design test setups in which investigations are only done within the rotational speed range suitable for the mirrors. Otherwise the waveform output to one of the scanning mirrors can be tuned to account for the lag and the reduced output angular rotation delivered by the mirrors to achieve a perfect circular scan. Both lag and angular rotation are dependent on the input oscillatory frequency.

Di Maio & Ewins (2010) highlighted the use of a combination of tracking systems and Continuous Scanning Laser Doppler Vibrometry (CSLDV). In addition to point-tracking a specific point on a rotating blade, one can simultaneously scan along the length of the blade (line-tracking) to capture lengthwise blade out-of-plane vibrations. AreaScan-tracking on a rotating blade then involves movement of the laser beam in across the surface of the blade. With this approach, ODSs of an online bladed system were successfully reconstructed from CSLDV measurements and FRFs of various points on the blades successfully determined as well.

A self-tracking system described below can also be used when one wants to perform investigations at scanning frequencies.

#### **b) SELF-TRACKING LASER DOPPLER VIBROMETRY (STLDV)**

As an alternative to rotating the orthogonally positioned mirrors (TLDV), one may also use STLDV. For this approach, the laser beam is focused on a vertex mirror that is attached at the centre of the blades' rotating shaft. A fold mirror is then used to reflect the beam back to a specific point on the rotating blade, as illustrated in the Figure 4.

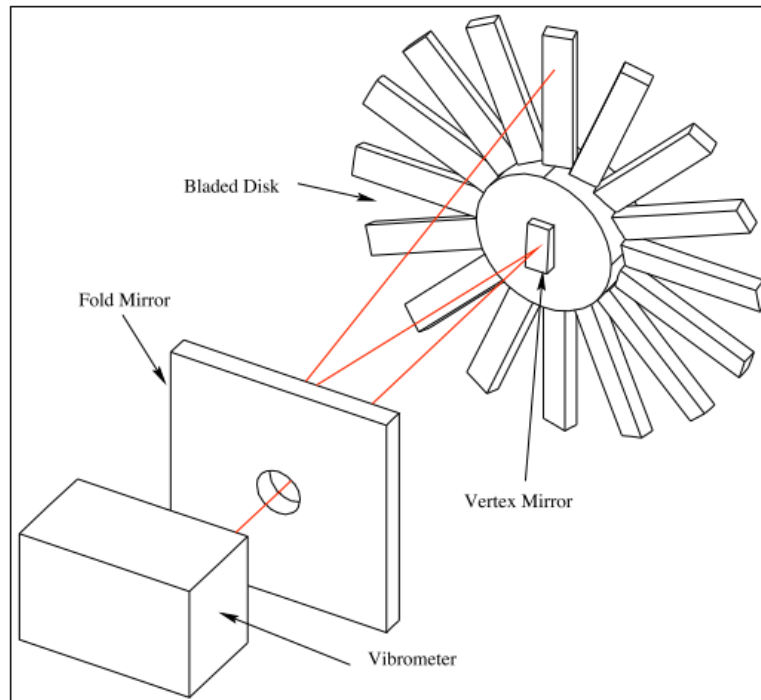


Figure 4: Schematic drawing of a self-tracking system (Lomenzo, 1998)

This self-tracking approach simplifies the synchronization scheme required, by replacing the electro-mechanical link in TLDV by a purely mechanical link, as stipulated by Lomenzo (1998). It is not necessary to know the rotational position of the blade of interest and the instantaneous rotational speed of the shaft. Also, there are no speed limitations. By using the rotating mechanical component of the rotating structure itself to control the position of the laser on the blade, a robust tracking approach can be developed (Zucca et al., 2012). The main drawback of using STLDV is that, additional components are introduced. The misalignment errors become a much more significant problem as one has to ensure that the vertex and the fold mirrors are perfectly positioned and aligned. The laser beam-shaft rotational axis also needs to be perfectly aligned. Although robust, this approach makes it very difficult to change the measurement point on the turbine blade. Due to these factors, some people may resort to characterising the dynamics of the scanning mirrors so that necessary compensations can be implemented to achieve perfect TLDV circular scans, (Halkon & Rothberg, 2006a).

### c) ASPECTS TO CONSIDER WHEN USING TLDV

The two main aspects one should consider for the successful use of TLDV are speckle noise effects and misalignment. These will be discussed in the following subsections.

#### **SPECKLE NOISE**

As indicated by Halkon & Rothberg (2006b), speckle noise is introduced in the measured output whenever the speckle pattern generated changes during the measurement time period. In a circular scan investigation, such changes are expected when the scanning system's frequency is different from the target rotational frequency, when there are distortions in the scan trajectory, and also when there is in-plane target vibratory motion. If the collected speckle pattern change is recurrent in that similar changes are generated

periodically, the speckle induced noise in the measurement is characterised by approximately equal amplitude peaks at the speckle pattern repeat frequency and higher-order harmonics. If this speckle repeat frequency is not expected, then misinterpretation of the obtained results may occur. The recurrent speckle noise associated with a stationary laser beam incident on a rotating target repeats at the target rotational frequency.

In the case of a scanning laser beam incident on a stationary structure, the speckle noise will be repeating at the scanning frequency. Halkon & Rothberg (2006b) suggested that a scanning laser beam used in conjunction with a rotating target will result in the expected speckle noise repeating at a frequency other than the scan or the rotational frequency. The repeat period corresponds to whenever both the target rotation and the laser scan have completed an integer number of cycles.

### MISALIGNMENT

When analysing a rotating structure, misalignment is another facet that affects the usage of TLDV. The axis of the scanning head has to be aligned with that of the shaft to which the blades are attached (translational alignment), and the blades must also be in a plane parallel to the face of the scanning head (rotational alignment). Figure 5 shows the possible translational and angular misalignments that can occur.

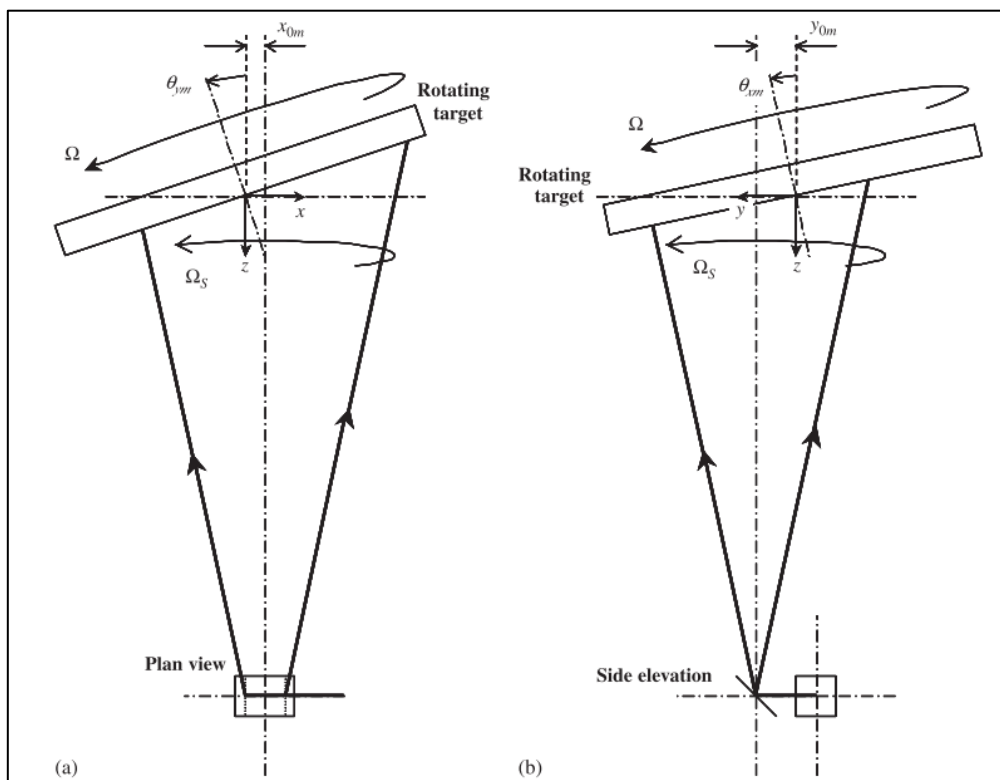


**FIGURE 5: Possible misalignments between the scanning head and target axes of rotation: translational and angular (Halkon & Rothberg, 2006)**

In Figure 5,  $x_{0m}$  and  $y_{0m}$  represent the translational misalignment, and  $\theta_{ym}$  and  $\theta_{xm}$  the possible angular misalignment.

In a circular scan, even small misalignments may introduce quite significant components to the measured velocity values. The misalignments are inevitable and Halkon & Rothberg (2006b) indicate that misalignments in the range of 0.5 mm and  $0.5^\circ$  can result in components of the order 10-20 mm/s in the measurements.

According to Castellini & Paone (2000) misalignment between the optic-axis of the tracking system and the axis of the rotating structure introduces a sinusoidal signal in the TLDV data. This is due to a surface velocity component along the beam direction, caused by the out-of-plane blade movement. The distance between the laser interferometer and target point on the surface of the blade thus changes in a sinusoidal way at a frequency that corresponds to the rotational speed.

Stated below are the sources of noise at the rotational frequency and its harmonics which one should expect to occur in the vibration signal as suggested by Castellini & Paone (2000).

- Mirror scanning system kinematics.
- Misalignment.
- Errors due to the reflection of the beam at the two mirrors at points which are not on the axis of the mirror rotation – a Doppler effect is produced which results in a velocity component that is in the same direction as the laser beam.
- Vibration of the scanning head body induced by the systematic movement of the scanning mirrors inside the measurement head (generally negligible).

Misalignment and imperfections in the scanning profile make the changes in the speckle pattern more significant and hence emphasize the presence of speckle noise. For circular scans, Halkon & Rothberg (2006b) showed that a significant drop in the speckle noise is noticed when one approaches the tracking condition (scan frequency/rotational frequency = 1). This therefore, implies that as a method to try and capture measurements with a higher SNR, one need to use a well-developed and robust tracking system.

Figure 6 illustrates the differences between the spectra of structural vibrations, misalignments and speckle noise, when Laser Vibrometry is applied to investigate the vibrations of a machine tool.

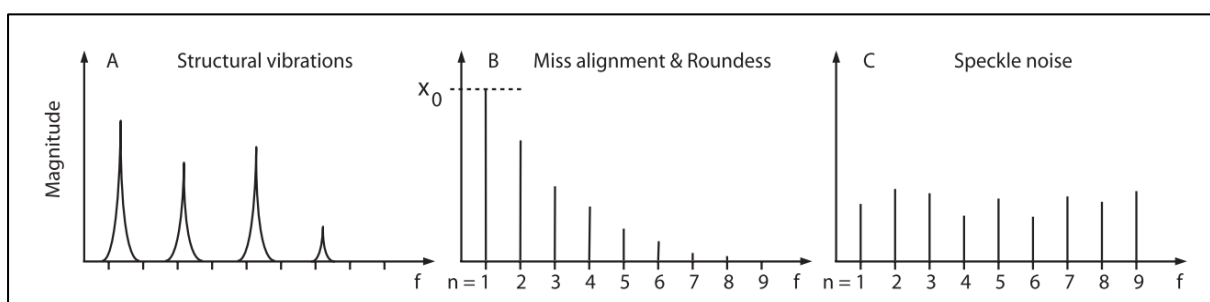


**Figure 6: Differences in spectra associated with structural vibrations, misalignment and speckle noise (Rantatalo, 2006)**

As noted from Figure 6, the presence of speckle noise can be identified in the frequency domain by sharp peaks which are also observed at the higher-order harmonics. Peaks due to misalignment decay as the frequency increases, and peaks due to structural vibrations do not have narrow bases. Thus it is possible to anticipate the appearance of the measured

data analysed in the frequency domain. This is of vital importance when it comes to interpretation of the results.

#### 1.2.4 DAMAGE DETECTION AND CHARACTERISATION

Damage detection and damage characterization in rotating turbine blades is currently one of the important fields in which non-contact measurement techniques are being considered. DIC has been applied to wind turbines to investigate strain distributions and to monitor blades under fatigue testing. It has been successfully employed to directly measure the crack tip displacement field in structures that are loaded in a cyclic manner. Companies such as Dantec Dynamics that supply optical measurement systems, have used DIC to characterise the properties that influence crack paths and also to investigate stress intensity factors and crack propagation laws.

The vibrational characteristics of a structure tend to change due to a decrease in stiffness associated with the presence of the damage. This in turn therefore means that the natural frequencies of the structure decrease as the damage increases. The local loss of stiffness at the point of damage can affect the global dynamic behaviour of the structure.

Various damage detection techniques that can be applied to structures have been highlighted by Ciang et al. (2008). These include the detection of acoustic emission events such as cracking sounds emitted as the damage in a blade progresses. Other techniques are thermal imaging methods, the use of fibre optics, and modal based approaches. For the current research, the modal-based approaches are of interest, and these will be discussed further.

##### a) MODAL BASED APPROACHES FOR DAMAGE DETECTION

According to Ciang et al. (2008), modal-based techniques are the most popular methods used to detect and characterize damage in structures. Various sensors, contact and non-contact, are employed to monitor the structural dynamic responses due to excitation. The approaches are based on the premise that the modal parameters, mode shapes, natural frequencies and modal damping, are functions of the mass and the stiffness of the structure. The physical properties of the structure, especially the damping and the stiffness, change considerably if damage is present. Damage detection is thus based on comparing structural responses of a pre-damaged state to those of a damaged state. Monitoring changes in the modal parameters or properties associated with these quantities can then be achieved.

Although modal based approaches have been successfully used, Doebling et al. (1997) mentioned a number of factors that influence the complexity of a vibration-based damage identification. These include the fact that the standard modal properties identification represents some form of data compression, which may lead to a loss of information pertaining to the state of the structure. Systematic errors such as those that result from the windowing of the data are inherently an issue. With some of the techniques employed, there is usually a finite frequency resolution, such that the identified modal parameters and the functions derived from them are not fully representative of the dynamics of the structure.

The damage in a structure is also a local phenomenon, of which the local responses are initiated at high frequencies. The global responses are excited only at lower frequencies.

According to Doebling et al. (1997), this occasionally presents limitations to the use of vibration-based techniques for damage detection and especially localization, as higher frequency excitations mean higher energy requirements. Methods such as investigating global frequency shifts will only be able to pick up the existence of damage, and will not point out the actual location of the damage.

Different levels of damage identification have been proposed by Rytter et al. (1991), and are stated below.

- Level 1: Ascertaining whether damage is present in a structure
- Level 2: Level 1 plus the determination of the geometric location of the damage
- Level 3: Levels 1 and 2, including quantification of the severity of the damage
- Level 4: Levels 1, 2 and 3, and prediction of the remaining service life of the structure

According to these authors, Level 3 can be achieved if vibration based approaches are coupled with a structural model, and for Level 4, association with the fields of fracture mechanics, fatigue-life analysis or structural design assessment might be necessary.

A typical approach one can use to achieve full damage identification and characterization is that described by Kumar et al. (2007). According to these authors, the use of dynamic properties of a structure to investigate damage typically involves the development of suitable thresholds on frequency changes. The onset of the critical stages of damage can then be detected before a structure or machine fails. In applications where low cycle-fatigue is involved, the accumulation of damage can be characterised based on continuum damage mechanics (CDM). The damage models can be defined in terms of a damage variable  $D$ , given by Equation (1.11), in which  $D = 0$  implies no damage and  $D = 1$  indicate complete failure.

$$D = 1 - \frac{E}{E_0} \quad (1.11)$$

$E_0$  is the initial structure's Young's modulus, and  $E(t)$  the Young's modulus at some time during the operational life of the structure.

To achieve a Level 2 damage detection requires the localization of the damage. One approach applicable to rotating machinery is the use of operational deflection shapes (ODS) or the residual of a mode shape. Asnaashari & Sinha (2014) used this approach to localize damage in cantilever beams. As mentioned by these authors, a crack in a beam under excitation will open and close in a cyclic manner. This leads to a non-linear behaviour in the dynamics of the structure, which will result in higher exciting frequency harmonic components in the response spectrum. By determining the Normalized Operational Deflection Shape (NODS) of a beam under excitation at a particular frequency, and comparing it to the NODS at higher harmonics of excitation frequency, they managed to locate the crack in the beam. A Residual Operational Deflection Shape (R-ODS) calculated by subtracting two NODSs was used to locate the damage. With the R-ODS, the effect of the ODS shape associated with the first harmonic component of the excitation is eliminated, which usually cannot be distinguished from the components due to damage.

Asnaashari & Sinha (2014) used Equations (1.12) and (1.13) to determine the NODS and the R-ODS.

$$(NODS)_{i,m} = \frac{(ODS_k)_{i,m}}{(MODS)_{i,m}}, \quad i = 1, 2, 3, \dots \quad (1.12)$$

$$(R - ODS)_{p,m} = (NODS)_{p,m} - (NODS)_{1,m}, \quad p = 1, 2, 3, \dots \quad (1.13)$$

$(NODS)_{i,m}$  is the normalised operational deflection at the  $i$ -th harmonic for mode  $m$ ,  $(MODS)_{i,m}$  the maximum ODS value at the  $i$ -th harmonic for mode  $m$ , and  $(R - ODS)_{p,m}$  is the residual operational deflection shape at the  $p$ -th harmonic with respect to the first harmonic. Displacement, velocity or even acceleration data can be used as the ODS input data.

The use of the R-ODS for damage detection requires installation of a number of accelerometers, as far as contact methods are concerned. Use of a full field measurement technique will thus be more favourable where rotating machines are concerned. 3DPT could potentially be exploited as a method for undertaking damage detection in turbine blades through the analysis of ODS.

In applying DIC for damage characterization in turbomachinery blades, LeBlanc et al. (2013) used a surface stitching approach to detect, localize and quantify the damage in statically loaded wind turbine blades. Digital images were captured for different sections of a 9-m blade, and the sections joined together (stitching) to get full-field measurements of the entire blade. These authors managed to demonstrate that DIC can be used to quantifying full-field strains around blade damaged areas. The investigation conducted was however limited to non-rotating blades loaded in a static manner.

### 1.3 SCOPE OF RESEARCH

In this research, non-contact methods are to be investigated for characterizing the online dynamics of a turbomachine. Two methods are of interest namely TLDV and 3DPT. With the knowledge that LDV has been successfully used to obtain reliable vibration measurements in a fixed frame of reference analysis, it is employed in a moving reference frame approach, and then adapted as a technique to validate the photogrammetry results in a scenario when a structure has to be analysed whilst it is rotating.

As mentioned in section 1.2.2c, of the literature survey conducted, correlation between contact methods (e.g. accelerometers) and 3DPT lead to inconsistencies between the two sets of results. These inconsistencies may be attributed to the limitations of using contact methods for analysing rotating structures, namely mass loading, errors introduced by telemetry systems and errors due to accelerometer cross-axis sensitivities. Also using photogrammetry, any structural rigid body motion associated with translational misalignment between the blades and the cameras is embedded in the measurements, which is not the case with contact transducers. This means more discrepancies in the results are expected between the techniques, since perfect photogrammetry system alignment with the blades is almost impossible. Thus to accurately establish the validity of photogrammetry as a non-

contact method for dynamic analysis of rotating structures, another non-contact technique has to be employed. TLDV is employed as that technique in this study.

Whilst the correlation between DIC and LDV has been investigated for stationary applications by Avitabile et al. (2010) and Warren et al. (2011), this work focuses on the investigation of the correlation between the two techniques in a rotational application, and ultimately the validation of DIC using TLDV. Through this investigation, experimental and post processing procedures that can be confidently used to accurately capture turbomachinery blade dynamics using 3DPT are established. Subsequently, the applicability of 3DPT captured blade ODSs for damage detection and localization is evaluated.

3DPT validation is done by comparing the out-of-plane captured 3DPT displacement profiles of a laser spot focused on a turbomachine blade to the TLDV displacements measured by the scanning system. Displacement demodulation with a LDV is more suited for this typically low frequency investigation, as mentioned in section 1.2.3. In addition, results being captured have to be correlated to directly measured 3DPT displacements. This means that possible introduction of errors into the results through frequency domain integration of velocities to displacements can be avoided using the LDV to measure displacements directly, rather than measuring velocities.

A frequency analysis approach is used to characterize the dynamics of the scanning mirrors of a LDV. This is done in light of the fact that the quality of the circular scanning path changes with the scanning frequency. The responses of the mirrors to external signals are investigated by using the position of the laser spot as an output of the system, in which the inputs are the voltage signals supplied to the mirrors. Using this approach, a technique to obtain nearly perfect circular scans with different scanning heads is developed. Thus instead of adapting information documented for one laser scanning head, a more reliable and practical way is presented with which characteristics specific to particular scanning head mirrors can be experimentally determined. The characterization process allows for the development of lookup tables that can be used for extracting signal properties (phase differences and magnitudes) necessary to accomplish a nearly perfect circular scan at a particular frequency of rotation of the laser beam.

Investigations done on damage characterization from ODSs have been on cantilever beams using accelerometer captured data, and non-rotating turbine blades using DIC, as described in section 1.2.4. As an extension of the work done on damage detection in cantilever beams by Asnaashari & Sinha (2014), this study also focuses on the implementation of similar procedures to rotating turbine blades, using ODSs measurements captured using 3DPT. Different signal parameters that can be used to detect and localize irregularities along rotating blades are investigated, and how well they each localize these irregularities evaluated. Conclusions drawn from this investigation serve to illustrate how robust 3DPT can be used as a technique for Structural Health Monitoring (SHM) of turbomachinery blades, using displacements captured at arbitrarily chosen rotor speeds.

The procedures and techniques presented for the use of 3DPT for turbomachinery blade dynamic analysis present opportunities such as investigating how the entire system of blades, hub and housing assembly, respond to various excitations. This serves as a more viable measuring technique to accelerometers, and contact methods in general, which are conventionally used. The full-field nature of photogrammetry also allows extensive validation

of numerical models of the turbomachinery systems developed using Finite Element (FE) packages.

This study also serves as the basis for the use of modal expansion and reduction strategies to obtain full-field FE results from limited DIC measurement data sets for rotating structures. For investigations on blade dynamic responses to impact loading of twisted, staggered blades, this becomes especially important as the camera's line of sight is lost on impact, and images of entire blade surfaces cannot be captured due to the blade twist.

## 1.4 DOCUMENT OVERVIEW

In this dissertation an extensive literature review, focused on optical methods for vibration analysis, is conducted and given in Chapter 1. Detailed descriptions pertaining to the operating principles of photogrammetry are also given. Typical applications where it has been used successfully are highlighted. Principles of LDV are described, with explanations on the adaptability of using a scanning head with two scanning mirrors to extend this approach to TLDV.

The experimental setup developed for use in this research is described in Chapter 2, and so is the FE modelling of the bladed disk (bisk). A bisk, which comprises of blades and disk manufactured from the same piece of material, is considered in this study. The modal analysis done on the bisk is described. This is done with the purpose of updating the developed Finite Element Model (FEM), so that the rotational speeds necessary to excite particular modes of the bisk could be established. The updated FEM is then used to develop a numerical Campbell diagram from which necessary bisk excitation and response information can be obtained.

Verification of the 3DPT using TLDV is then presented in Chapter 3. For this correlation investigation, the characteristic responses to excitation of the mirrors in a scanning head of a laser Doppler scanning system are first investigated. The development of look-up tables that can provide information necessary to achieve perfect circular scans, at various frequencies of rotation is described. How the implemented TLDV system is used to validate the 3DPT displacement measurements is also presented.

Finally, documented in Chapter 4, is the use of 3DPT to analyse rotating turbine blades by capturing different ODS. Damage detection procedures are implemented to detect and localize irregularities in the responses of various points along the blades due to the localized nature of blade excitation using electromagnets. Conclusions and recommendations for future work are then given in Chapter 5.

## CHAPTER 2: EXPERIMENTAL SETUP AND FE MODELLING OF A BLADED DISK

### 2.1 INTRODUCTION

This chapter gives an overview of the experimental setup used in this research. Design considerations of the setup are made according to the type of investigation at hand and the resources available as well. A blisk to be rotated by a 5.5 kW motor mounted on a test bench was designed. To better understand the designed and manufactured blisk, and also for numerical analysis purposes, a FE model was developed in MSC/Patran. This model was then updated following modal analysis conducted using Modal 2 OROS software, to obtain a numerical model that better represents the physical blisk.

### 2.2 EXPERIMENTAL SETUP

The experimental setup used was designed by Diamond (2015) as part of his studies on blade tip time of arrival on a radial-flow blisk. Given in Figure 7 is the setup.

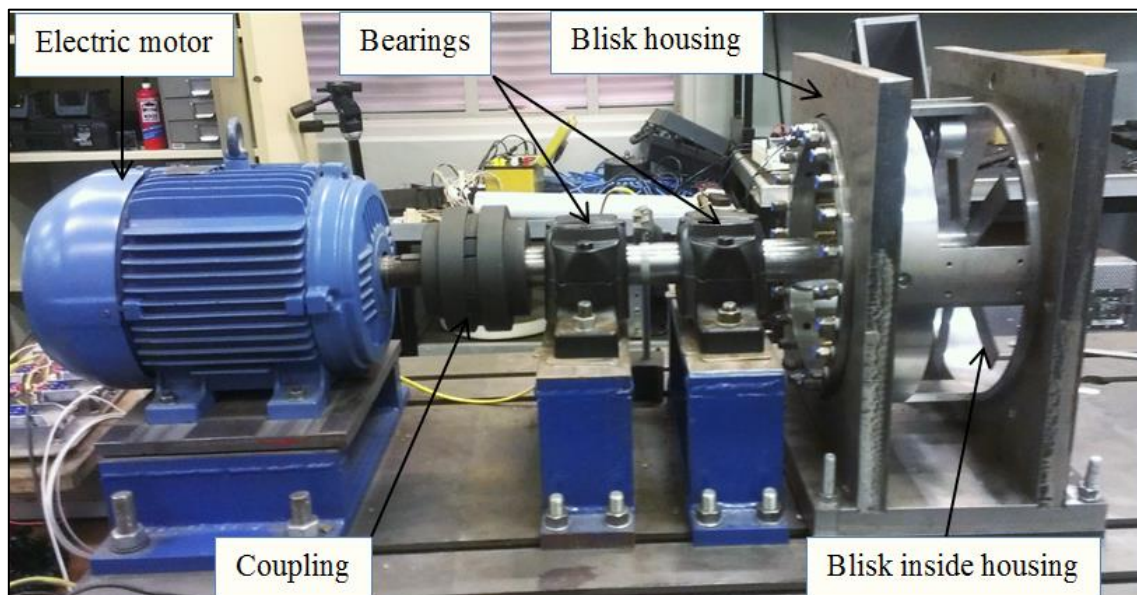
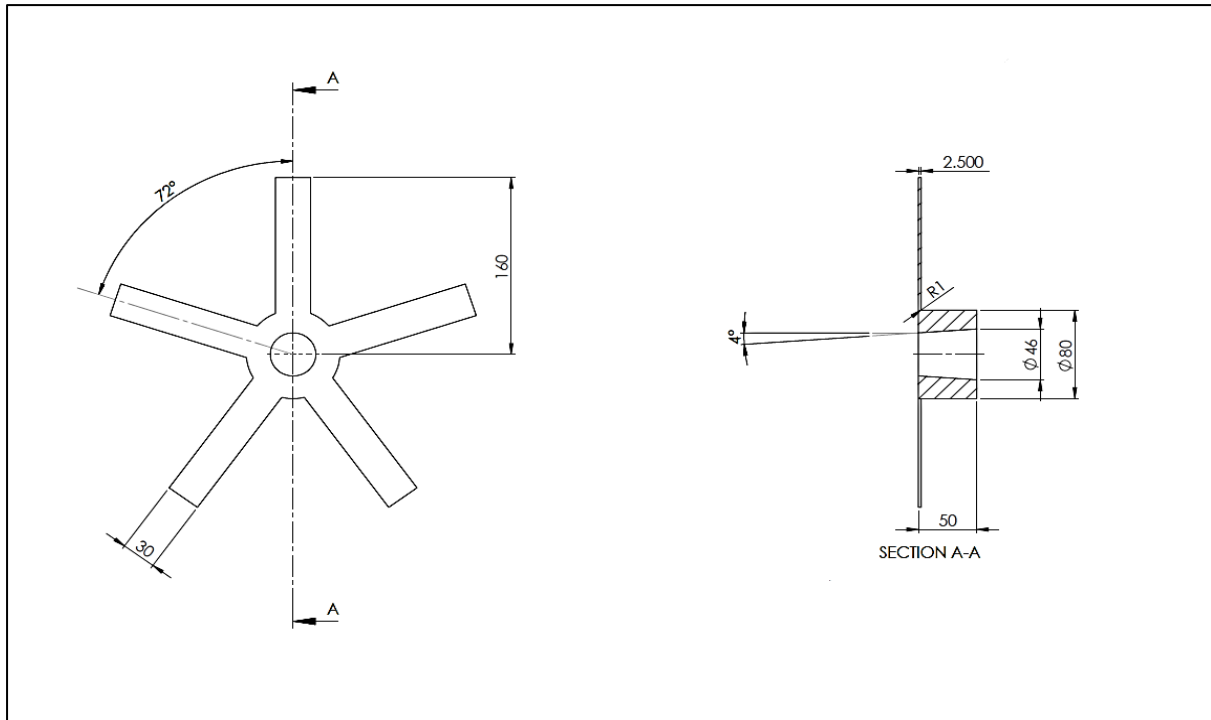


Figure 7: Experimental setup (Diamond, 2015)

An axial-flow blisk ( $0^\circ$  blade stagger angle) was designed by the author of this dissertation. Five blades, with thicknesses of 2.5 mm and lengths of 160 mm were used. The blades and disk were manufactured from a solid billet of mild steel. A blisk was considered in this study to reduce problems such as mistuning which is introduced when other fixture types such as welding and firtree mountings are used. Consequently a blisk is ideal when the effects of variability of the blade mountings on the vibration of the system need to be minimized. Given in Figure 8 are the blisk dimensions in millimetres.



**Figure 8: Blisk dimensional drawing**

Typically in blisks the blades are staggered at an angle or have a twist, and are therefore able to drive some air as they rotate. These kinds of blisks ensure that there is participation of the blades, the disk and also the shaft in the dynamics of the system. This is not the case with axial blades with no twist, where the shaft is uncoupled (no net torque in shaft), or radial blades without twist, where the disk is uncoupled in the sense that there is no net force in the transverse direction.

Purely axial blades with no twist are used in this study as they present the simplest configuration in terms of the cameras being able to capture the entire surface of the blades from the root to the tip. Since the main focus of the research is the development of non-contact methodologies to use for rotating machinery vibration analysis, axial blades were used to avoid unnecessary experimental complications. The manufacturability of the blisk also played an important role in deciding on a purely axial blisk instead of a blisk with staggered blades or with some form of twist.

The available motor used could run at a maximum rotational speed of 1500 RPM, and external excitation of the blades was achieved using electromagnets. The motor and blisk were mounted on top of a sturdy bench with vibration isolators to limit vibration transmission to the floor. The scanning head and the high speed cameras were placed on a different bench to isolate them from the vibrations of the blisk system. For monitoring and control of the rotational speed of the motor, a shaft encoder was used, with a zebra strip that had 79 stripes on it. During set up of the system, the Damalini Easy-Laser D525 shaft alignment kit was used to align the motor, shaft and the bearings.

### 2.3 FINITE ELEMENT MODELLING OF THE BLISK

MSC Marc was used to model the system for finite element analysis (FEA). To establish confidence in the results obtained from the analysis, a simple investigation of a single blisk blade was carried out, and the results obtained were compared to those obtained from theoretical calculations. The following mild steel properties were used (Kutz, 2002).

**Table 1: Assumed material properties**

| Property                          | Value |
|-----------------------------------|-------|
| Young's Modulus (GPa)             | 210   |
| Density (1000 kg/m <sup>3</sup> ) | 7.85  |
| Poisson's ratio                   | 0.3   |

Natural frequencies were calculated numerically, using the formula suggested by Crocker (2007) for rectangular blades. Equation (2.1) however applies to perfectly rectangular cantilever beams, yet the blades are curved at the point of attachment to the hub. Thus the FEM model used assumed that the blades were perfectly rectangular only when the FEM results were being confirmed numerically.

$$\omega_i = \alpha_n^2 \sqrt{\frac{EI}{\rho AL^4}} \quad (2.1)$$

$E$  is the Young's modulus of the material,  $I$  the area moment of inertial of the beam,  $\rho$  the material density,  $A$  the area (width x thickness), and  $L$  the length of the beam. The constants  $\alpha_n$  vary according to the boundary condition, and for cantilever beams, Table 2 values are used.

**Table 2: Constants for determination of  $\omega_n$  of a cantilever beam**

| Bending mode shape number (n)              | 1     | 2     | 3     | 4      |
|--|-------|-------|-------|--------|
| Boundary condition constant ( $\alpha_n$ ) | 1.875 | 4.694 | 7.885 | 10.996 |

For the FEM analysis, Hex20 elements were considered as a first iteration in which a linear distribution of strain through the element is assumed, and the stress state varies in all three dimensions. Reduced integration with assumed strain was used to avoid inaccuracies due to shear-locking, which the Hex elements are likely to suffer from. Convergence to the analytical solution (1.41% error) was obtained when the model was IsoMesh-ed using 4 element nodes along the thickness, 15 along the width, and 60 along the length of the blade. An error of 1.46% was however, obtained for an analysis using Hex8 elements, with a mesh density of 4 element nodes along the thickness, 30 along the width, and 100 along the length of the blade with a solution time three times less than that for the Hex20 elements. Thus, for investigating the bending modes of a beam, Hex8 elements were more economical with an acceptable accuracy. These values were therefore used as general guidelines for meshing the model for FE analysis, to ensure that the mesh was not too coarse such that it yielded unreliable results, or unnecessarily fine as this would require substantial computing power.

The Inverse Power Sweep method was used for the FEM modal analysis, since only a few modes needed to be extracted, instead of the Lanczos method which is optimal for the extraction of several modes. The FE results obtained had good correlation with the analytical solution. It was then surmised that modelling the whole structure with Hex8 elements, and then using a mesh density similar or better than that for the blades, would give accurate results when analysing the blisk.

Figure 9 shows the bending modes calculated analytically and using the FE method.

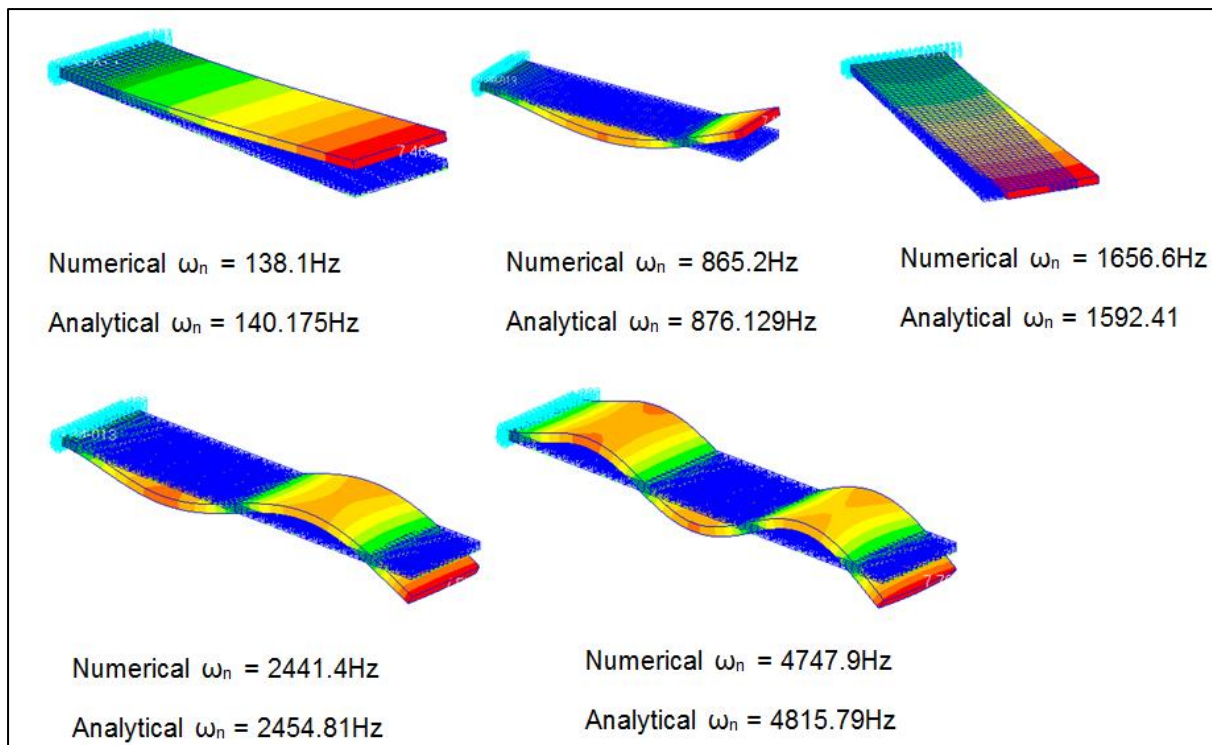


Figure 9: Finite element model verification using analytical results

## 2.4 FINITE ELEMENT MODEL UPDATING (FEMU)

After modelling the blisk using MSC/Patran, FEMU had to be done to verify and validate the model. To do this, hammer impact testing was used to determine input and response vibration measurements. A roving hammer approach was adopted, and the Modal 2 software developed by OROS was used for the data acquisition and analysis. Figure 10 shows the geometry of the blisk created using the impact testing software. A tri-axial accelerometer was attached at location 601. The modes of interest to be investigated were those for the blades. None of the nodes of the blades were expected to be at the reference location 601. Table 3 gives sensitivities of the Dytran 3263A1 tri-axial accelerometer and the PCB 086 C03 impact hammer force transducer used.

**Table 3: Hammer impact testing device sensitivities**

| Device                                | Sensitivity |
|---------------------------------------|-------------|
| Accelerometer x-direction (mV/g)      | 10.29       |
| Accelerometer y-direction (mV/g)      | 10.52       |
| Accelerometer z-direction (mV/g)      | 10.86       |
| Impact hammer force transducer (mV/N) | 2.15        |

Double impact excitations and over-range measurements were rejected. The blisk was placed on a supporting foam rubber during the test.

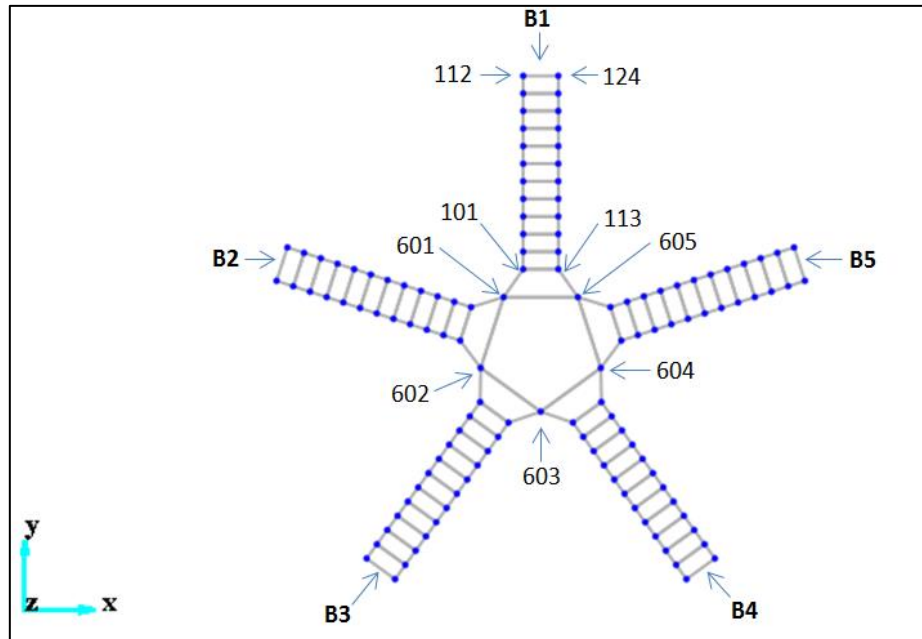


**Figure 10: Blisk geometry FEMU using OROS**

As shown in Figure 10, two columns of measurement points along each blade were used, enabling the torsional deflections of the blisk blades to be captured. The investigations were carried out for a frequency range of 0-5kHz. From the initial FE analysis, out of plane bending modes with a maximum of 3 nodal lines were expected. Using 12 measurement points along the length of the blades ensured that all the modes of interest could be captured suitably without spatial aliasing.

Shown in Figure 11 is the blisk being tested, the markings indicating the locations on the blades and the disk which were excited by the impact hammer.

After impacting the blisk at the locations indicated in Figure 11, and capturing the responses using a tri-axial accelerometer, modal identification was done using Modal 2 software. A total of 24 modes were identified. Shown in Figure 12 are the first three out-of-plane bending modes obtained. The entire list of natural frequencies and damping factors of the obtained modes is given in Appendix A.

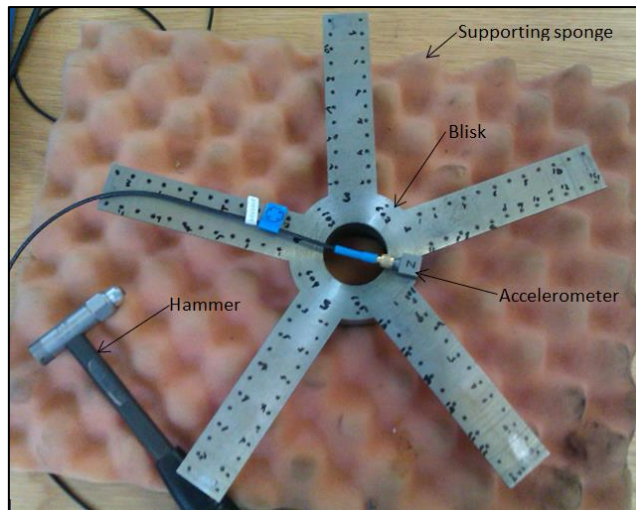


Figure 11: Modal analysis of blisk using the impact test

## 2.4.1 COMPARISON OF EXPERIMENTAL MODAL PARAMETERS TO ANALYTICAL MODAL PARAMETERS

### a) CONVERSION OF COMPLEX MODES TO NORMAL MODES, AND MAC CALCULATIONS

The mode shapes obtained experimentally are complex in nature, and those obtained numerically, using MSC/Marc, are normal modes with the mode shape vectors being described in terms of real numbers. No damping was considered in the FE analysis of the blisk. According to Friswell & Mottershead (1995) the comparison of such a numerical model created without consideration of damping, and the experimental model with unknown damping characteristics can still be carried out by approximating the experimentally determined complex modes with equivalent normal modes.

One of the simplest and most common ways of achieving this, as suggested by these authors, is to obtain the real mode shapes by multiplying the modulus of each element of the complex mode shape by the sign of the cosine of its phase angle. This is an established method for lightly damped structures.

A different approach suggests that a complex transformation be used, to calculate the real mode shape components. The real mode shapes are then obtained using Equation (2.2), details of the derivation which are given by Friswell & Mottershead (1995).

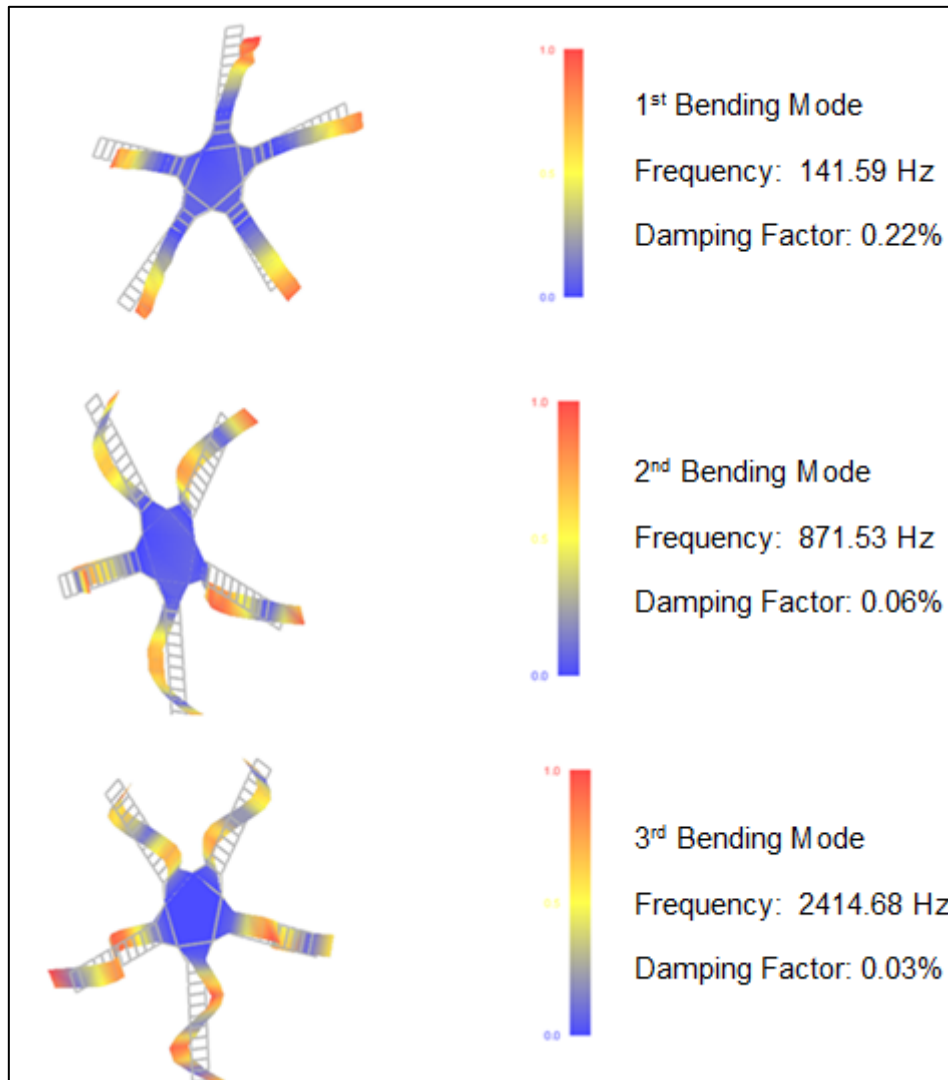
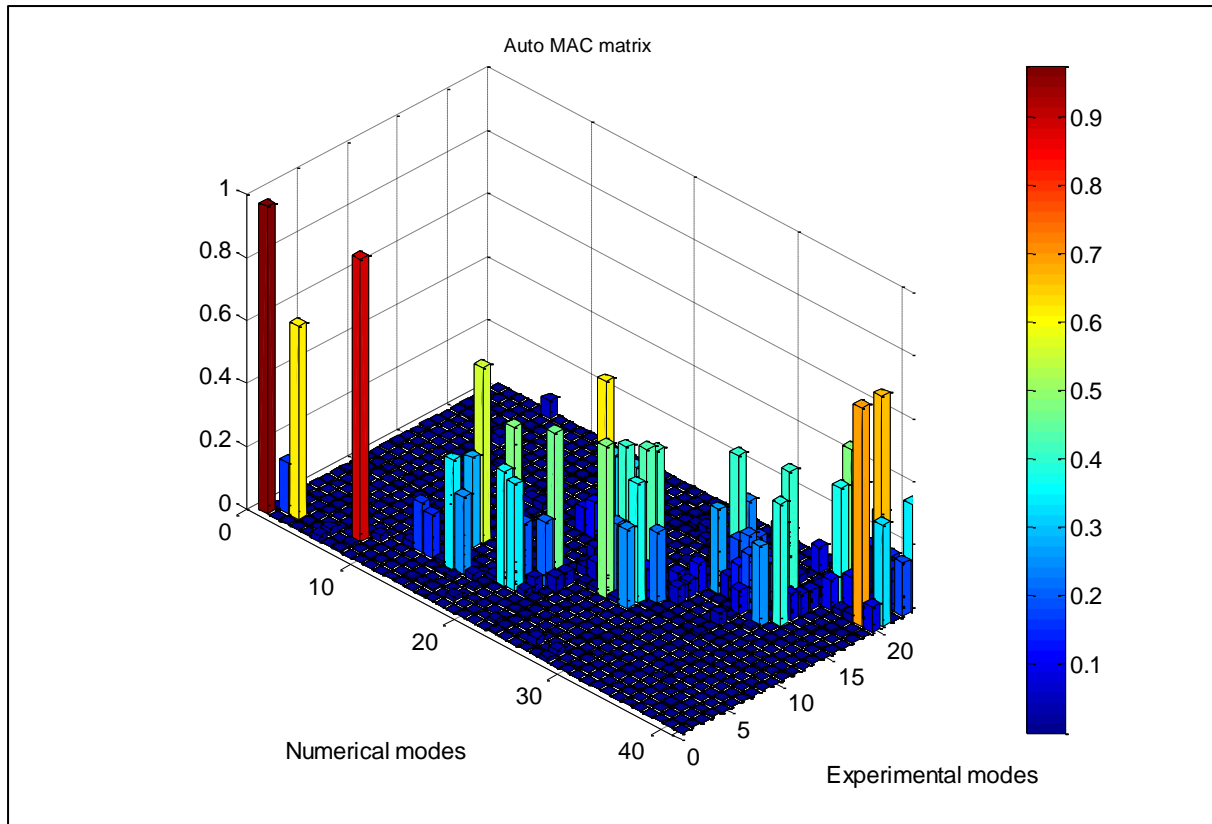


Figure 12: Modal analysis first three bending mode shapes

$$\phi_R = Re(\phi_C) + Im(\phi_C)(Re(\phi_C)^T Re(\phi_C))^{-1} Re(\phi_C)^T Im(\phi_C) \quad (2.2)$$

Thus the real mode shape  $\phi_R$  is determined from the real part,  $Re(\phi_C)$  and the imaginary part,  $Im(\phi_C)$  of the experimentally determined complex mode shape. Using Equation (2.2) to convert the complex mode shapes to normal mode shapes, the Modal Assurance Criteria (MAC) values calculated to evaluate the correlation between the two sets of mode shapes, are indicated in the Figure 13. These MAC values were determined before the numerical model was updated.



**Figure 13: MAC for the blisk before model updating**

It is observed from the results above, that a diagonal does exist in the MAC matrix, although only six of the mode shape pairs have values larger than 0.6 (considered as good correlation between mode shape pairs). To improve the numerical model, updating of the model was done by first investigating the variation of the natural frequencies with changes in the Young's modulus, the density, and the Poisson's ratio.

#### **b) MODAL PAIRING AND NATURAL FREQUENCIES COMPARISON**

The experimentally determined natural frequencies of the blisk were compared to those determined numerically using MSC/Marc. As indicated by Ewins (1984), the most obvious comparison can be drawn by plotting the experimentally measured natural frequencies against the numerically determined values. The points should lie on a straight line or close to a straight line with a slope of 1. If however, the points lie more or less on a line with a different slope, then it is likely that there is an erroneous material property. Widely scattered points along a straight line indicate that major errors exist in the FE model.

41 natural frequencies were determined numerically, and only 24 modes were identified from the experimental data. Mode pairing was done to decide which natural frequencies corresponded to each other, for comparison purposes. This was done by considering similar mode shapes which had natural frequencies close to each other. A total of 18 mode pairs were considered.

Figure 13 shows the numerically determined natural frequencies plotted against the experimentally determined frequencies.

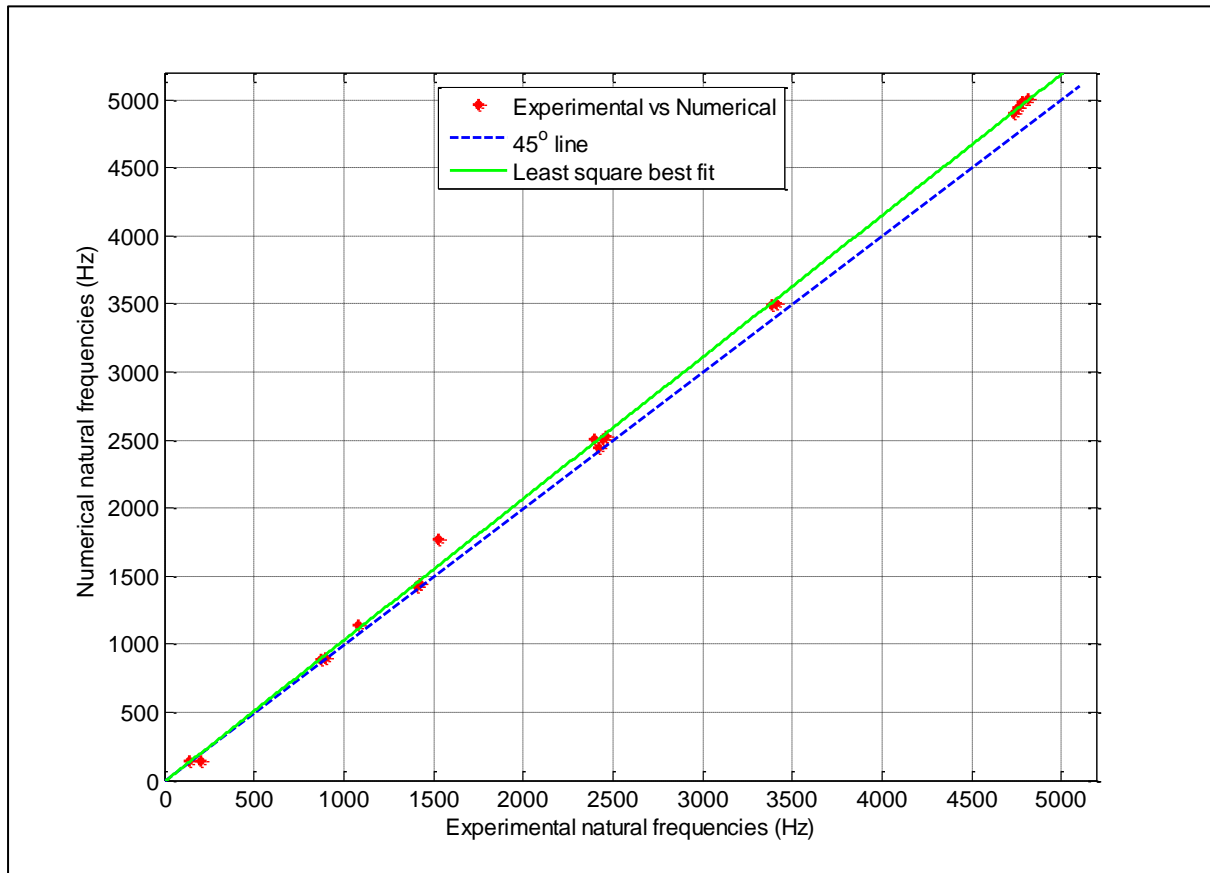


Figure 14: Comparison of the experimental to the analytical natural frequencies

From Figure 14, it is evident that the points lie roughly on a straight line with a slope calculated as 1.040. They are not at all widely scattered along the straight line, meaning that adjusting the material properties, was the only necessary model updating required. Since the model of the blisk is not complicated, errors arising from modelling procedures (boundary conditions and constraints) are unlikely.

#### 2.4.2 MODEL UPDATING PROCEDURE

The model updating procedure, as mentioned previously, was aimed at varying the material properties used for the FE modelling. The ultimate goal was to obtain numerical natural frequencies similar to those measured experimentally. Since the blisk alone is a simple structure, modelling it in MSC/Patran was not a complicated task and no serious errors were expected. The primary concern was however the material properties. Judging from the results obtained from the comparison of the two sets of natural frequencies, updating the model using these parameters had to be done.

Long-standing model updating procedures typically aimed at changing the elemental stiffness and/or the elemental mass matrices, as connections of different components of a structure cannot be perfectly modelled when doing FEA. In this case however the structure is a blisk manufactured from the same block of material. So even though the simulated model in MSC/Patran is constructed from separate blades and a disk to better control the meshing, the Contact Property was used. With this boundary condition, separate parts are

'glued' together, and exceptionally reliable results are usually obtained by doing this. With this in mind, the model updating approach used was focused on the model material properties.

The model updating procedure adopted was that based on a sensitivity analysis, in which the variation in the natural frequency as a result of changes in the Young's modulus ( $E$ ), the density ( $\rho$ ) and the Poisson's ratio ( $\nu$ ) is investigated. These three values were varied, one parameter at a time, and the rates of change of the natural frequencies of the blisk noted. Once the sensitivity matrix ( $S$ ) had been determined, the necessary change in the material properties were calculated according to the procedure outlined by Asgari et al. (2013). Given in Equation (2.3) and (2.4) are the relationships used in the updating procedure.

$$[S]\{\Delta p\} = \{\varepsilon\} \quad (2.3)$$

$$S_{ji} = \frac{\partial R_j}{\partial P_i} \quad (2.4)$$

In the above expressions,  $\partial R_j$  was taken as the change in the natural frequency associated with mode  $j$  and  $\partial P_i$  the change in parameter  $i$ .  $\{\varepsilon\}$  is the residue obtained by calculating the difference between the numerical and the experimental natural frequencies, and  $\{\Delta p\}$  the changes in the proportional parameters one will have to apply to update the model. The finite differences approach was used to determine the elements of the sensitivity matrix. The variations of the modal frequencies with the various material properties for the 18 finite element modes paired successfully to the experimentally determined modes are given in Appendix B to D.

From these results, it was noticed that the natural frequencies, for all the modes investigated, increased with increasing Young's modulus and decreased with increasing density. The various modes have different sensitivities to variations in these parameters as can be noted by the different slopes. For an increase in the Poisson's ratio, however, the modal frequencies increased for some modes, but decreased for the other ones.

To determine  $\{\Delta p\}$ , inverting the  $18 \times 3$   $[S]$  matrix and subsequently multiplying it by  $\{\varepsilon\}$  gave values that, when used to update the material properties, yielded improbable data that could not be further analysed. It is suspected that this was a result of the fact that the sensitivities of the natural frequencies to the Young's modulus and the Poisson's ratio differed considerably, which makes the inversion of  $[S]$  inaccurate. However when only one parameter was updated separately, results given in Equation (2.5) were obtained for initial parameters chosen to be  $E = 210 \text{ GPa}$ ,  $\nu = 0.3$ , and  $\rho = 7850 \text{ kg/m}^3$ .

$$\{\Delta p\} = \begin{Bmatrix} E \\ \rho \\ \nu \end{Bmatrix} = \begin{Bmatrix} -1.315E4 \\ 0.404795 \\ 0.002049 \end{Bmatrix} \quad (2.5)$$

When the values above were used to update the finite element modal properties, Figure 15 shows the results obtained.

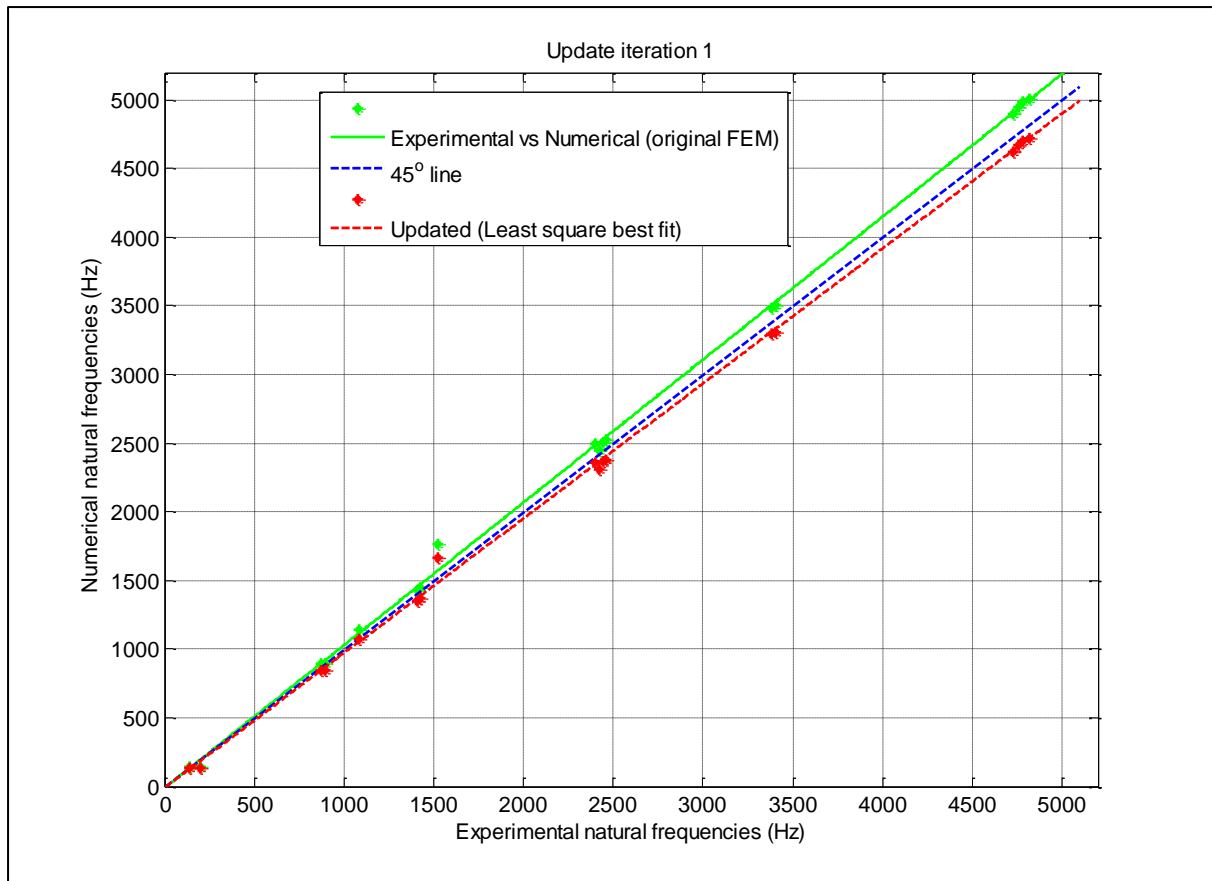


Figure 15: Experimental vs analytical natural frequencies

Analysing Figure 15, it can be observed that the first updating iteration shifted the natural frequency pairs closer to the  $45^\circ$  line as expected, but is still slightly off.

An iterative updating procedure similar to the one suggested by Asgari et al. (2013), which is illustrated in Figure 16, was then implemented in Matlab to update the model.

$\{\Delta p\}$  values were added to the initial parameter values chosen, and another analysis was run to determine the responses of the updated model. The responses obtained were then used to calculate the new residue  $\{\varepsilon\}$ , and using the same, previously defined sensitivity matrix, new updating parameters  $\{\Delta p\}$  were calculated. The proximity of the plots of the two sets of natural frequencies, to the  $45^\circ$  line was monitored, and after 5 iterations, it was concluded that the natural frequencies obtained from the numerical analysis were sufficiently close to those determined experimentally. As indicated in Figure 17, the experimental versus numerical natural frequency plot overlaps the  $45^\circ$  line.

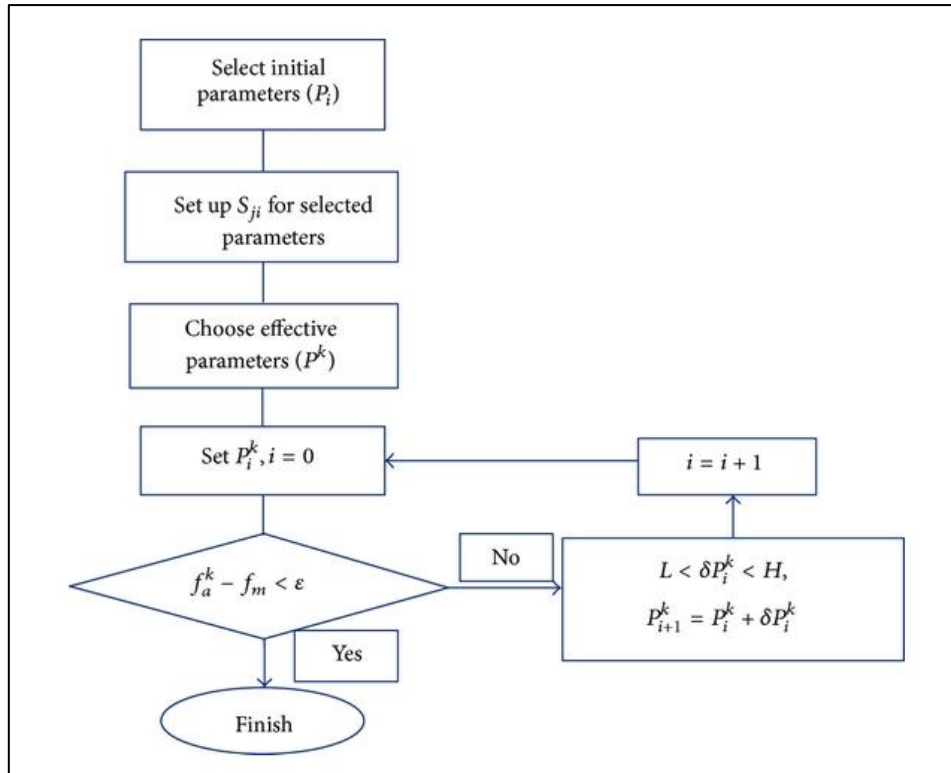


Figure 16: FEMU iterative procedure adopted (Asgari et al., 2013)

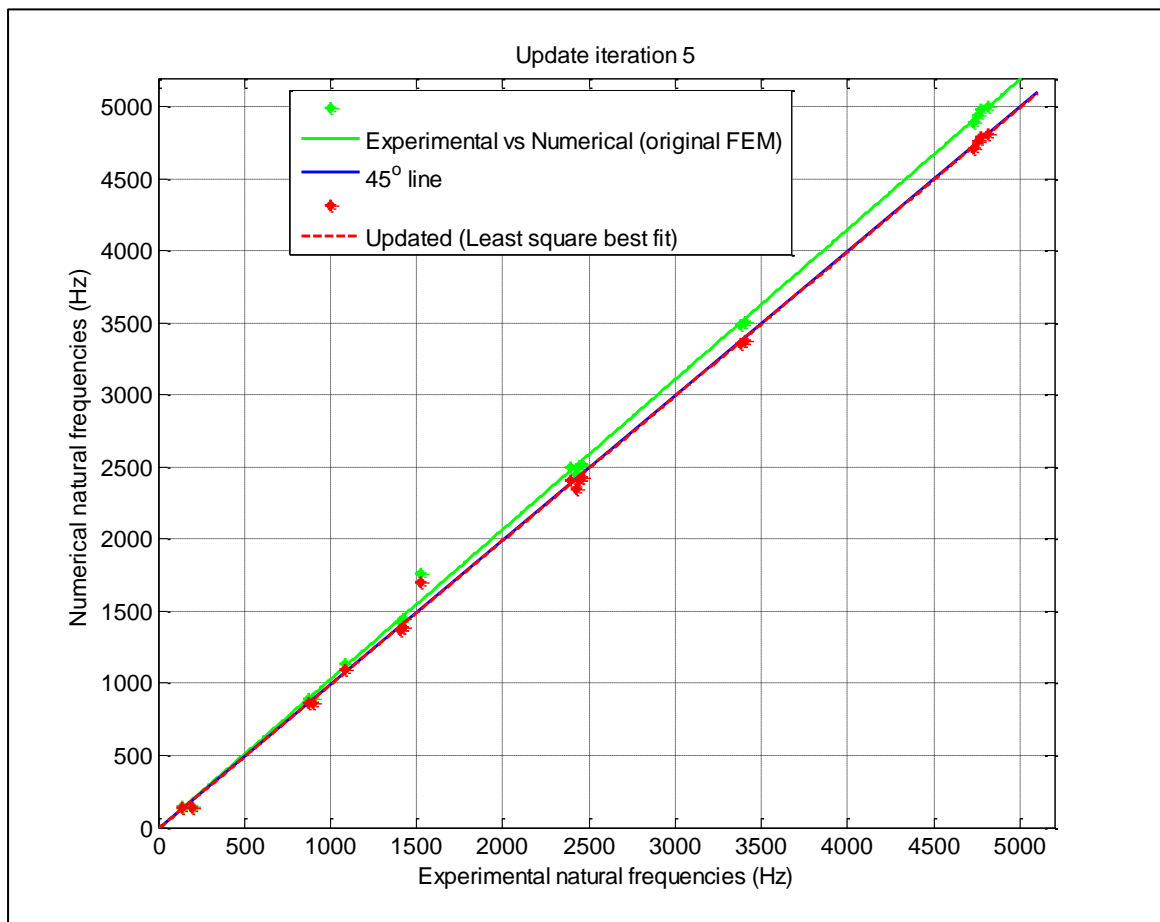


Figure 17: Experimental vs analytical natural frequencies after model updating

Table 4 below gives the material properties which when used in a finite element model analysis will give natural frequency response results that are good enough to represent that of the actual physical blisk.

**Table 4: Updated material properties**

| Property                          | Value   |
|-----------------------------------|---------|
| Young's Modulus (GPa)             | 201.24  |
| Density (1000 kg/m <sup>3</sup> ) | 8.1197  |
| Poisson's ratio                   | 0.29588 |

### 2.4.3 DETERMINATION OF THE EXCITATION FREQUENCIES USING A CAMPBELL DIAGRAM

With the FE model updated, the next step conducted was to determine the various motor speeds at which the blisk was to be rotated to excite particular modes shapes. Shown in Figure 18 are the first three bending modes of the blisk. Attention was paid to these bending modes of the blisk at this point as it was intended to validate measurements from DIC with TLDV when one of these modes was being excited. This validation is illustrated later on in the dissertation.

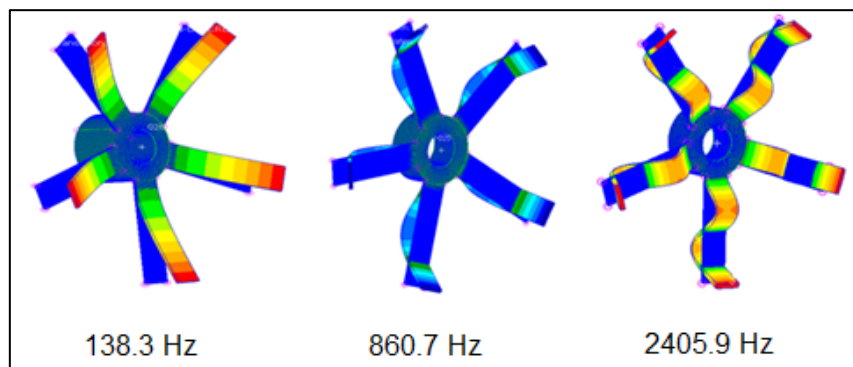


**Figure 18: First 3 bending modes of the blisk**

Figure 18 is given to illustrate the three modes of interest. The natural frequencies given were determined when rotational stiffening effects were not being taken into account. These were however considered in all the other investigations conducted using the updated numerical model.

Since the experiments had to be conducted around the resonance frequencies of the blisk, which results in the modes shown in Figure 18, a numerical Campbell diagram was developed from FE. A numerically constructed Campbell diagram that accounts for rotational stiffening effects could be comfortably used in this case since the numerical model of the structure had already been updated. The mode shapes of interest were those with 0-2 nodal diameters (ND). According to Zucca et al. (2012), the umbrella mode and the mode with 1 nodal diameter are usually not isolated and excitation of multiple resonances is very likely. Also, they involve the responses of the driving shaft and the bearings supporting it. These were however considered as the blades turned out to be too stiff for proper excitation of modes with more nodal diameters. As described by Zucca et al. (2012), any nodal

diameter mode shape of a rotating blisk can be excited by any engine order determined from Equation (2.6).

$$(EO)_{n,ND} = nN_b \pm ND \quad (2.6)$$

In the above expression,  $EO$  is the engine order,  $n$  an integer value ranging from 0 to a value  $N$ , which will correspond to the  $n$ th engine order,  $N_b$  the number of blades on the blisk, and  $ND$  the number of nodal diameters of interest. With 2 electromagnets, EOs which are multiples of 2 could be used to extract rotational speeds at which the motor had to be run to excite the bending modes of interest. A Campbell diagram was developed for the blisk with 5 blades ( $N_b = 5$ ), for integer values chosen from  $n = 0$  to  $n = 500$ . In Figure 19 the blue dots indicate the intersection of the engine order lines and the modes they can excite. The blue dots show all the possible EOs that can be used to excite the modes. For the first three bending modes, EOs of 20, 66, and 102 can be considered. The red dots show these EOs. Rotational speeds extracted from the Campbell diagram are given in Table 5 that follows. For better representation of the Campbell diagram, only order lines corresponding to the EOs 20, 66, and 102 are shown.

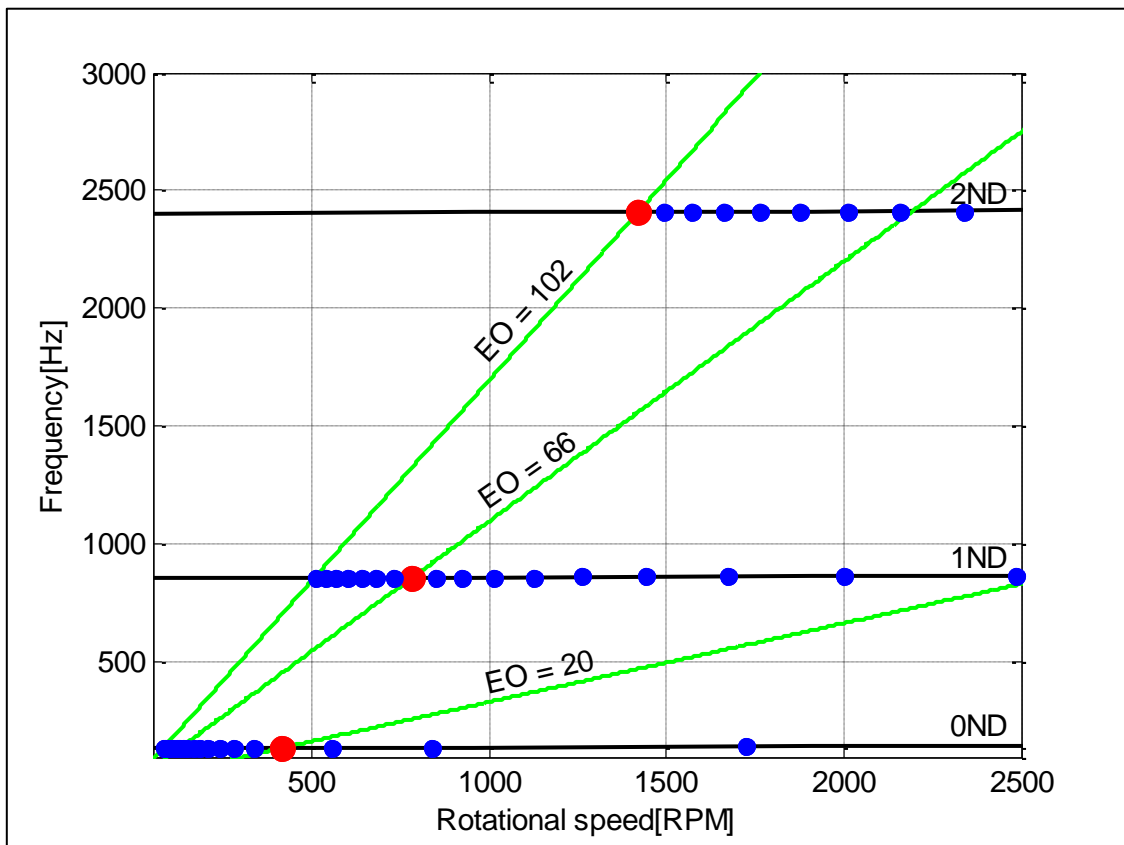


Figure 19: Analytical Campbell diagram

Although not clearly visible in Figure 19, the natural frequencies of the blisk were increasing with increasing rotational speed. Thus even though these effects are slight, rotational stiffening effects were not negligible.

**Table 5: Motor rotational speeds for excitation of various bending modes**

| <b>Nodal diameters</b> | <b>Motor rotational speed (RPM)</b> |
|------------------------|-------------------------------------|
| 0                      | 416.84                              |
| 1                      | 783.45                              |
| 2                      | 1417.11                             |

Thus by rotating the motor at the above mentioned speeds, the respective bending modes can be expected if two electromagnets were exciting the blisk. To capture the different mode shapes distinctively, EOs considered should be such that the rotational speeds they correspond to are well separated from those speeds represented by the EOs of the other modes.

## CHAPTER 3: VERIFICATION OF 3DPT RESULTS USING TLDV

### 3.1 INTRODUCTION

This chapter gives an overview of the verification of 3DPT using TLDV. A procedure that can be used to characterize the dynamics of the mirrors of a scanning Laser Vibrometer is presented. Investigations conducted in which a laser beam focused on a fixed point of a rotating turbomachine blade was being tracked using high speed cameras are given. The correlation between the TLDV and the 3DPT out-of-plane displacement measurements is also investigated, and how well DIC can be used to analyse rotating structures established.

### 3.2 CONTROL OF THE POSITION OF THE LASER BEAM

As discussed in paragraph 1.2.3a, at high frequencies the scanning mirrors of a Laser Vibrometer will not be able to make the laser dot trace a perfect circle. This is due to the inertia of the mirrors, the non-linearity of the galvanometric mirrors which drive the mirrors and the time delay between the input of the waveform into the scanning device and the actual mirror rotation. These factors are frequency dependent, and to characterise the mirror dynamics, a frequency based approach was used. The characterization process involved determining the necessary phase and amplitude compensation parameters that would improve the scanning path when incorporated into the voltage signals supplied to the mirrors. Whilst investigations have been done previously by some researchers to characterize the dynamics of these mirrors, this information cannot be reliably used owing to the possible physical variations from one scanning head to the other. The physical conditions and functionality of the scanning systems (mirrors and galvanometric motors actuating them) of different scanning heads cannot be identical. Therefore characterization of the mirrors of the available PSV 300 was necessary to ensure more reliable definition of scanning paths.

Shown in Figure 20 is the experimental setup which was used for this investigation.

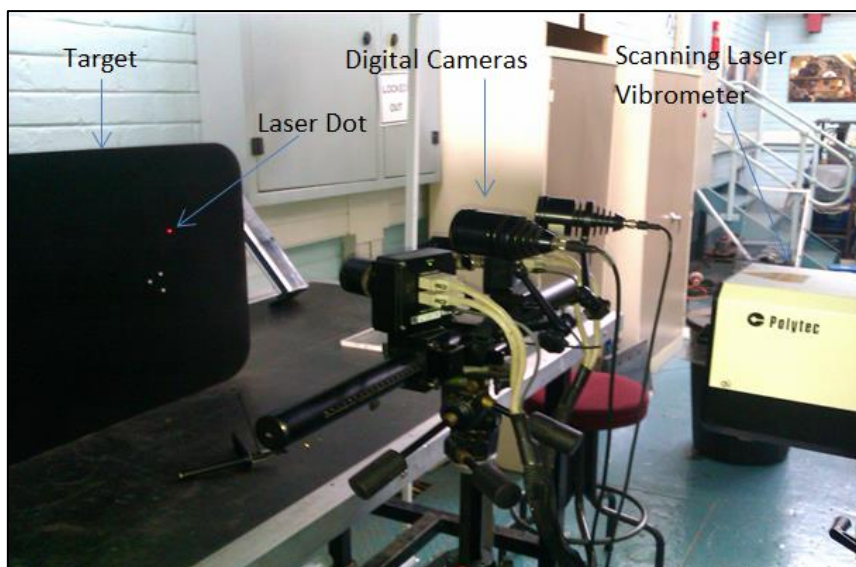
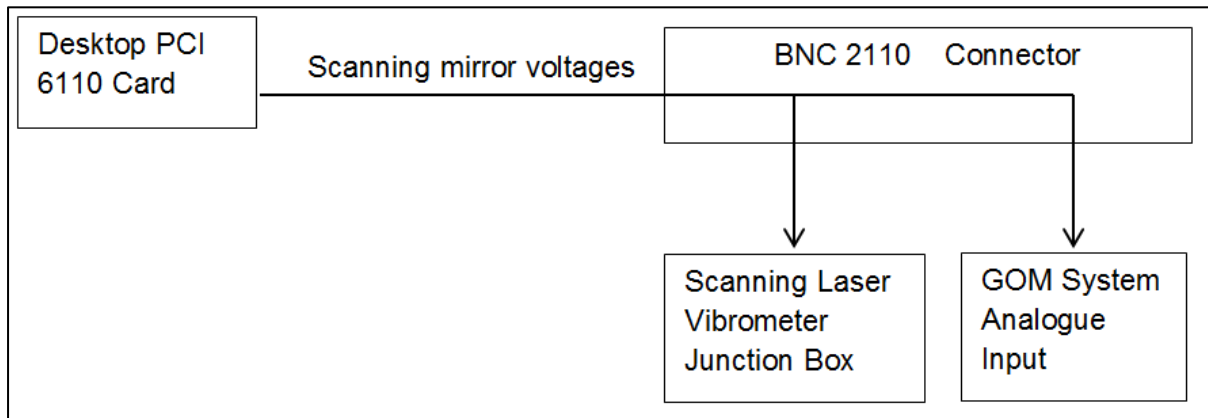


Figure 20: Experimental setup (characterization of the dynamics of scanning mirrors)

A GOM 4 M model stereo videography system was used to track a laser dot focused on a black painted glass panel. This system has an allowable maximum frame rate of 480 Frames per Second (FPS). Owing to the difficulties in controlling the lighting in the laboratory during the testing, a high frame rate was more desirable, as this would mean more images of the dot captured in a period of time. With a high frame rate the laser dot traces a shorter in-plane distance from one image to the next. This aids in the tracking and identification process. So a frame rate of 450 FPS was chosen, with a total of 5000 frames being captured per analysis. At this frame rate the cameras were operating at their minimum resolution.

Given in Figure 21 is a schematic representation of the experimental setup. Two voltage signals were generated using a LabVIEW program developed on the scanning Laser Vibrometer computer system. These scanning mirror voltages were output via the on-board PCI 6110 card on the computer, to a BNC 2110 connector, before being simultaneously supplied to the scanning Laser Vibrometer Junction Box and the GOM system analogue input terminals. Recording of the analogue voltage signals exciting the mirrors was synchronized with the initiation of image capturing with the cameras.



**Figure 21: Schematic representation of experimental setup for characterization of dynamics of scanning mirrors**

Sine sweep signals were supplied to the mirrors and as the laser dot focused on a black painted glass panel rotated, images of the dot were captured using high speed cameras. When capturing images with the high speed cameras, a red coloured laser dot appears white if it is focused on a black panel. Figure 22 shows typical images captured. On the left is an image taken using a conventional camera, and on the right the one from high speed cameras tracking the dot. Whilst just a circular path is captured using a conventional camera, high speed cameras can capture the actual position of the laser dot as long as the following conditions are met:

- the frame rate is high enough compared to the frequency of rotation of the laser dot (at least twice, to avoid aliasing),
- the lighting is good enough for the captured images to represent the laser dot as a point circular enough for the image processing software to be able to identify and track it.

The image given for the high speed cameras in Figure 22 was after an analysis of an image sequence captured at 450 FPS whilst the laser dot was being rotated at 10 Hz. Tracking the laser dot in three dimensions using DIC is referred to as three dimensional Point Tracking (3DPT) in this section.



**Figure 22: Images of a scanning laser dot focused on a black painted glass panel (10 Hz)**

Various sine sweep signals were considered, and it was required that the limit frequency of the sweeps be greater than 25 Hz. 25 Hz was the maximum frequency at which the blisk was to be rotated. For rotational frequencies greater than 20 Hz, images of the laser dot captured by the cameras were not circular enough for the correlating software to be able identify and track the dot throughout the image series sequence, due to streaking. The captured laser dot was too elliptical for proper point identification. Thus the characterization of the dynamics of the mirrors in a frequency manner could only be done using sine sweep signals with an upper frequency limit of only 20 Hz. This presented a problem as the maximum frequency of interest was 25 Hz.

To address this, a characterization in the frequency range 0-20 Hz was conducted, and an approach to check the validity of the characterization for frequencies greater than 20 Hz devised. Since checking the validity of the characterization at any frequency involved implementing the phase and amplitude compensation and then investigating how close the scanning path was to a perfect circle, being able to track the dot at high frequencies was not necessary.

Typically a white circular path such as the one shown in Figure 23 would be obtained when an image is captured with the high speed cameras at 25 Hz laser scanning frequency. Identification points could then be manually added along this scanning path in PONTOS. Manually adding the points has the downside of introducing some inaccuracies in the measurements, although these are generally very small. This made it possible to approximately determine the scanning path the laser spot was describing as it rotated at frequencies greater than 20 Hz. The x-coordinate and y-coordinate positions of these points could then readily be obtained.

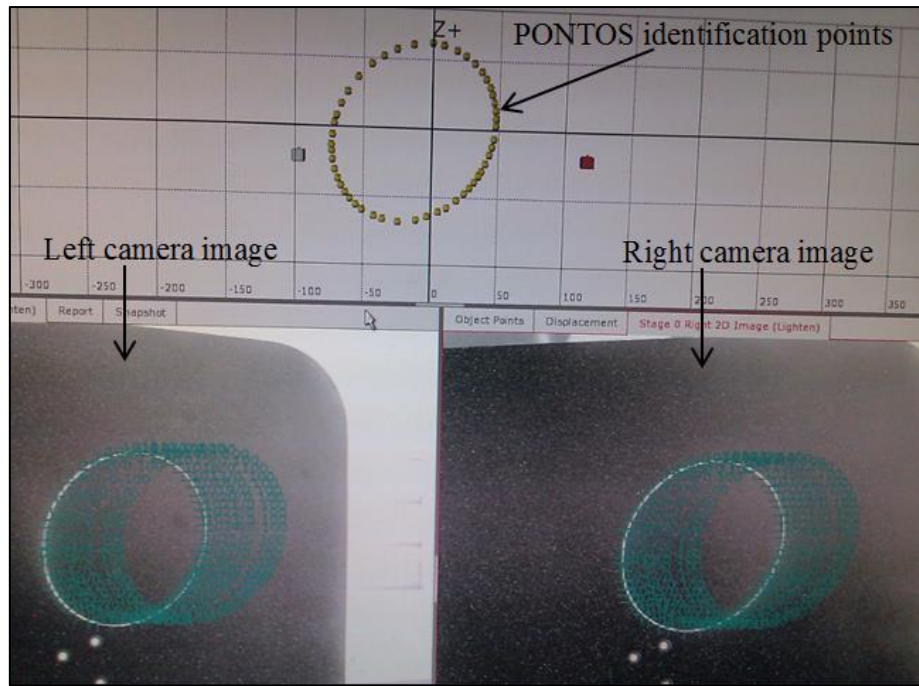


Figure 23: Scanning path investigation approach for high frequencies (25 Hz)

Given in Figure 24 are the voltage signals supplied to the mirrors, which were subsequently recorded by the photogrammetry system during image capturing.

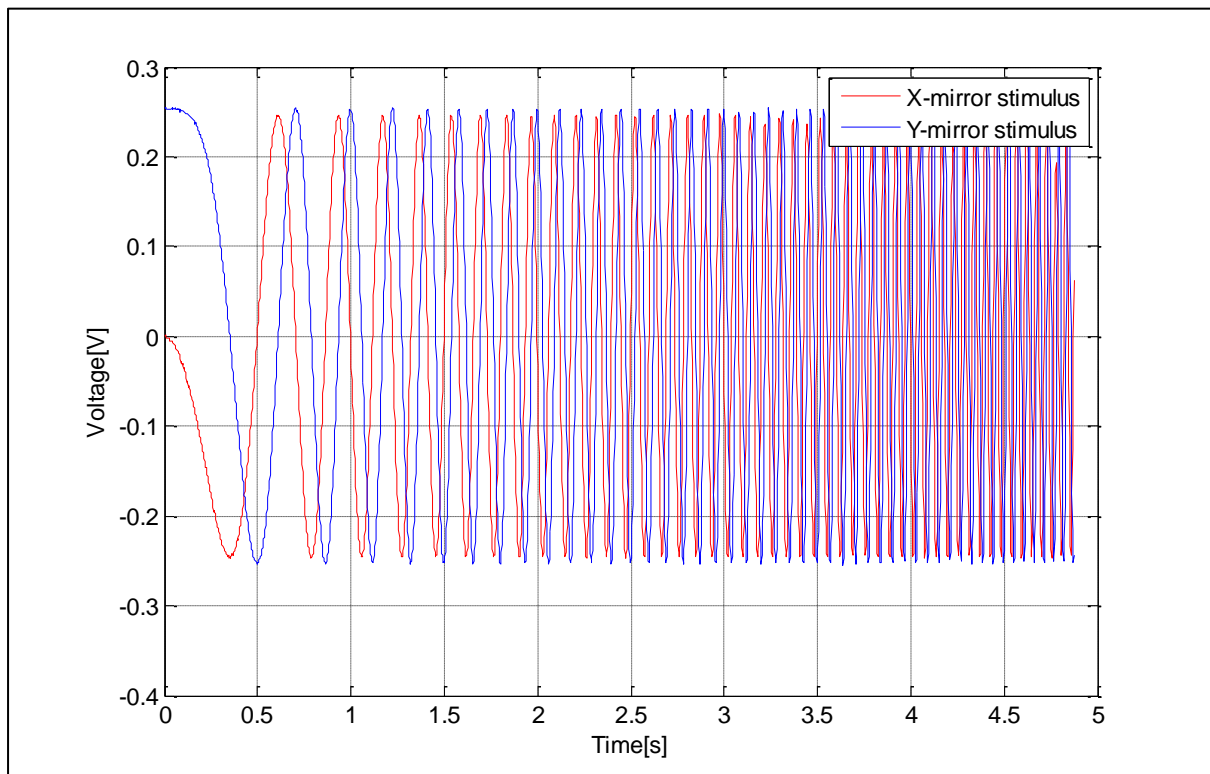
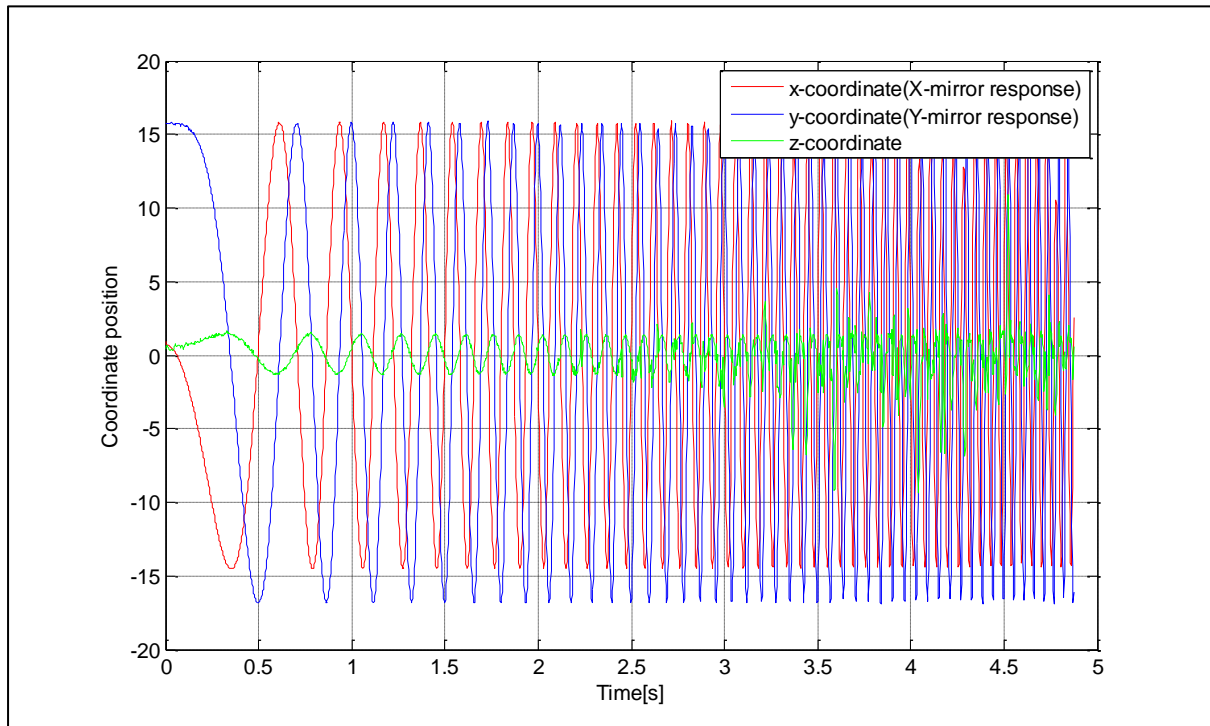


Figure 24: Stimulus signals supplied to the mirrors

Figure 25 shows the x, y, and z coordinates of the laser dot, also recorded by using the DIC system for the same test given in Figure 24.



**Figure 25: Response of the scanning mirrors (position of rotating laser spot)**

For the 0-20 Hz scanning frequency range, even though good tracking of the laser dot was possible, it was not 100% efficient because at some angular positions, the lighting was not good enough for proper point identification using PONTOS. This means that in a couple of instances, the laser dot could not be captured by the cameras. For post processing purposes, it was necessary to have evenly spaced data in time. To achieve this, a spline interpolation technique was used to fit in the missing data points.

Using the voltage signals supplied to the scanning system as the stimulus signal, and the x- and y-coordinate positions of the laser dot as the responses of the X and Y scanning mirrors, the frequency response functions (FRF) of the scanning mirrors were determined using the LabVIEW Virtual Instrument (VI) Frequency Response Function (Mag-Phase).vi. A rectangular window and a frequency resolution of 0.205 Hz determined from time increment of the input time signals were specified. Figure 26 and 27 show the magnitude and phase results obtained for the X and Y mirrors.

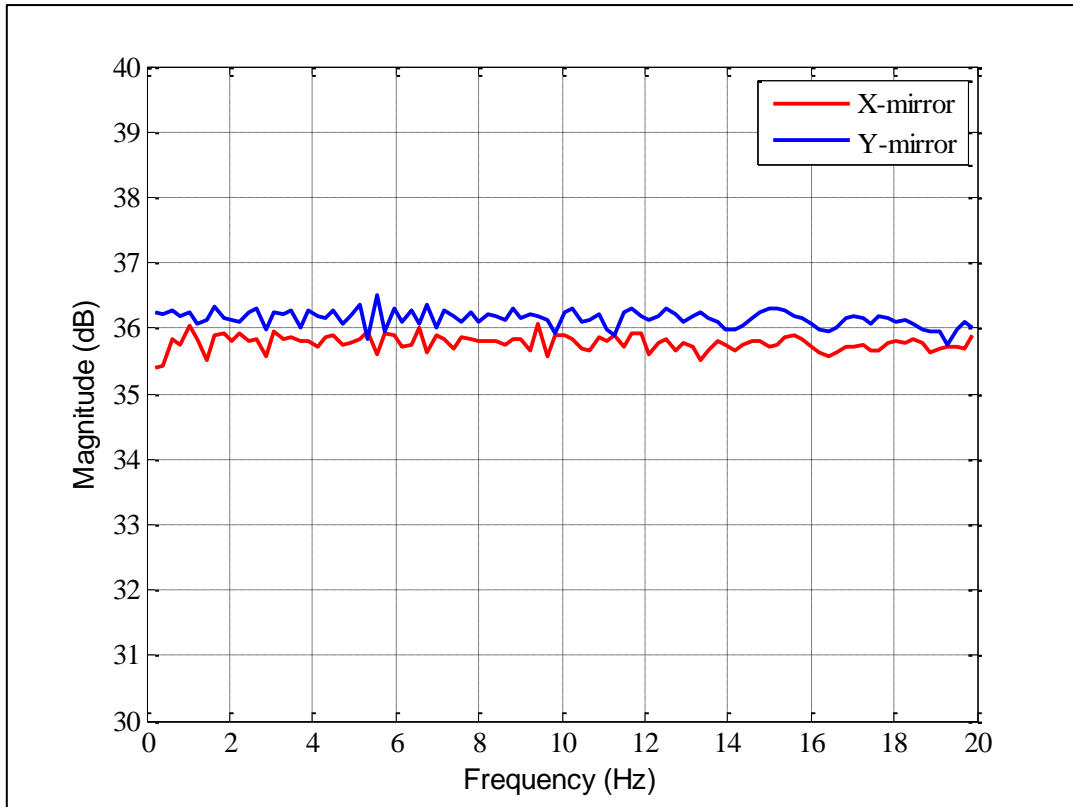


Figure 26: FRF magnitude variation with frequency

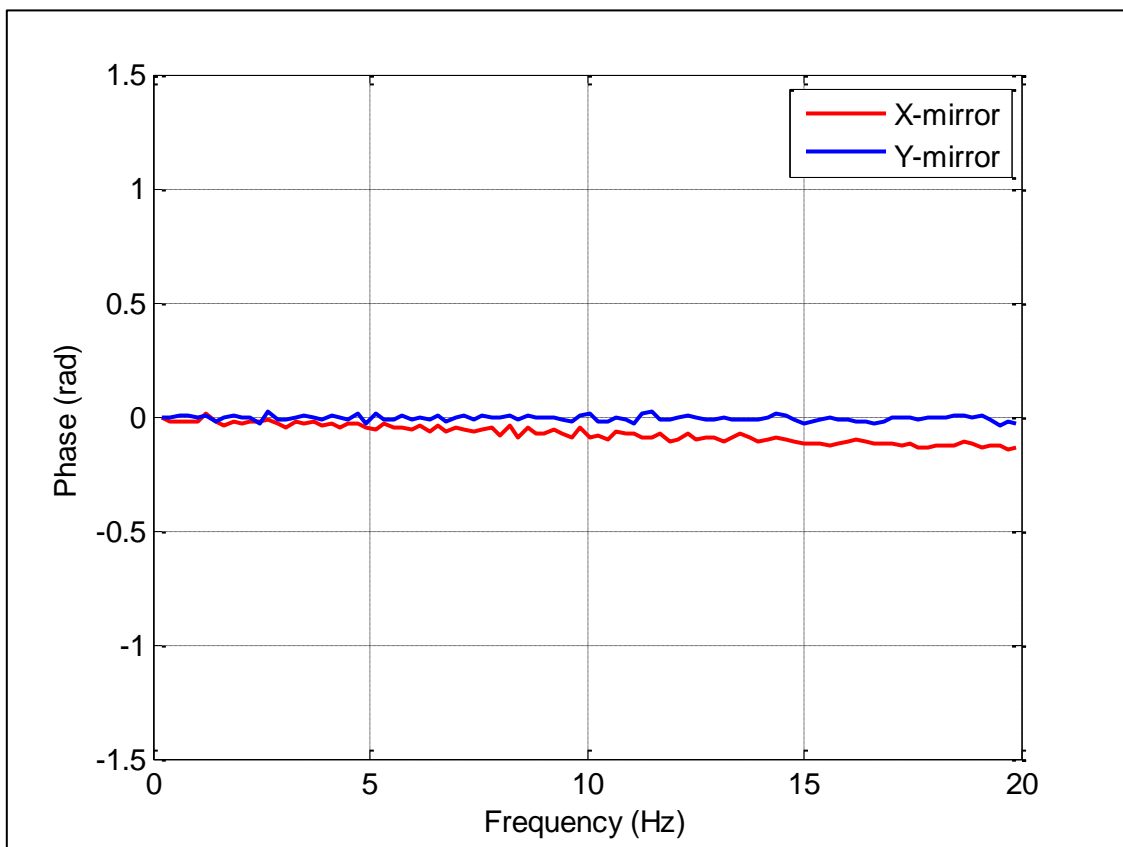


Figure 27: FRF phase variation with frequency for the scanning mirrors

For both mirrors, there is no magnitude variation with frequency, as illustrated in Figure 26. From Figure 27, there is a linear frequency-dependant phase lag for the X scanning mirror.

To change the tracking path from an ellipse to a circle, one can introduce a phase lag value in Equation (1.9) that describes the scanning angle of the X mirror, as described in the literature review. For the frequency range considered, the phase lag changes linearly with the frequency. A line was fitted using the obtained phase results, and an equation of a line given in Equation (3.1) was then used to determine the necessary phase compensation  $\phi_s$  for the X mirror for a particular frequency of rotation  $\omega$ , of the laser beam.

$$\phi_s = -6.597 \times 10^{-3} \omega - 8.802 \times 10^{-3} \quad (3.1)$$

To check the consistency of the responses obtained from the 0-20 Hz sweep, lines were also fitted for 0-10 Hz and 0-15 Hz frequency sweeps. The results are shown in Figure 28 for a frequency range of 0-20 Hz.

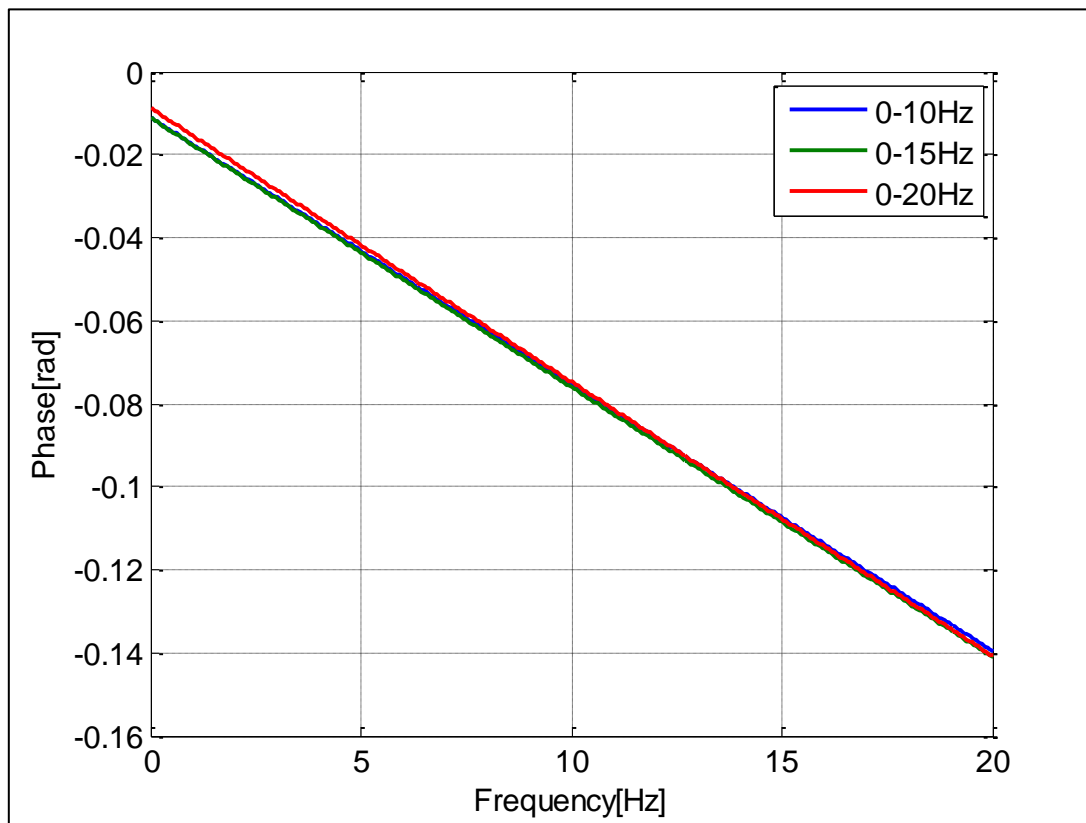


Figure 28: Phase lag variations for different frequency sweeps

From Figure 28 consistent results are obtained for the different frequency sweeps investigated, with a maximum phase lag difference of about 0.0023 rad at 0 Hz between the 0-20 Hz and the 0-10 Hz frequency sweeps. The visible differences can be attributed to variations in the amount of data points PONTOS was able to identify for the different frequency sweep analyses. The number of identified points varied due general changes in the lighting in the room, as the results were not simultaneously captured. For the remainder of the analysis, characterization results obtained from the 0-20 Hz frequency sweep were used to improve the scanning paths.

Figures 29 to 31 illustrate how introducing  $\phi_s$  calculated using Equation (3.1) improves the scanning path for various frequencies. To investigate how robust the employed circular scanning system was, the accuracy of the system was tested at 25 Hz, and also at 40 Hz. This was done to check if the linear phase variation obtained for frequencies up to 20 Hz was applicable to higher frequencies as well. Also shown in these figures are circularity constants,  $C_c$ , determined using the Equation (3.2). The closer  $C_c$  is to unity the better the scanning path approximates a perfect circle. Thus a perfect circle will have a  $C_c$  equal to unity, and as the scanning path becomes increasingly elongated,  $C_c$  approaches zero. In Equation (3.2),  $A$  is the area and  $P$  the perimeter of the scanning path.

$$C_c = \frac{4\pi A}{P^2} \quad (3.2)$$

The areas of the scanning paths were determined using the Matlab function `polyarea.m`, which calculates the area of a closed polygon, and the perimeters from the summation of the lengths of the edges of the scanning paths.

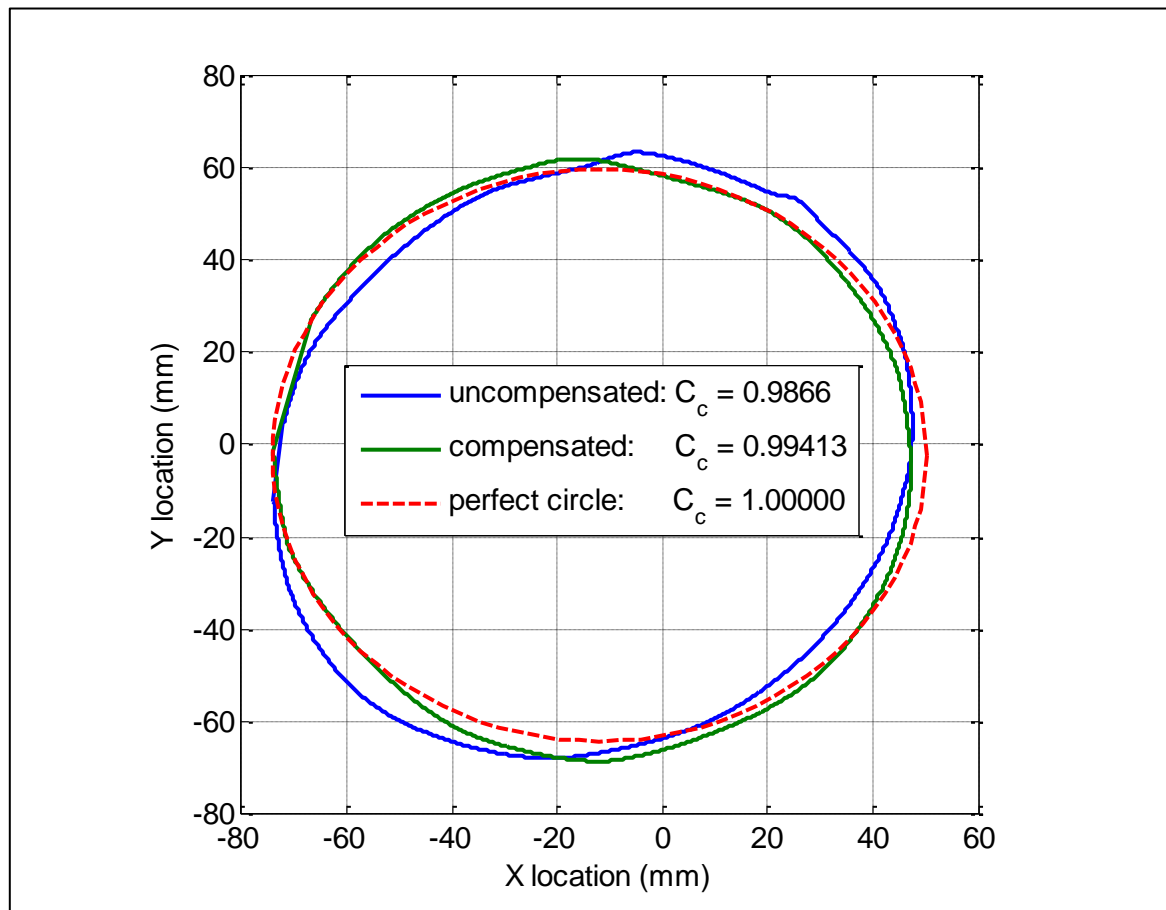


Figure 29: Effect of phase compensation on the laser scanning path (20 Hz)

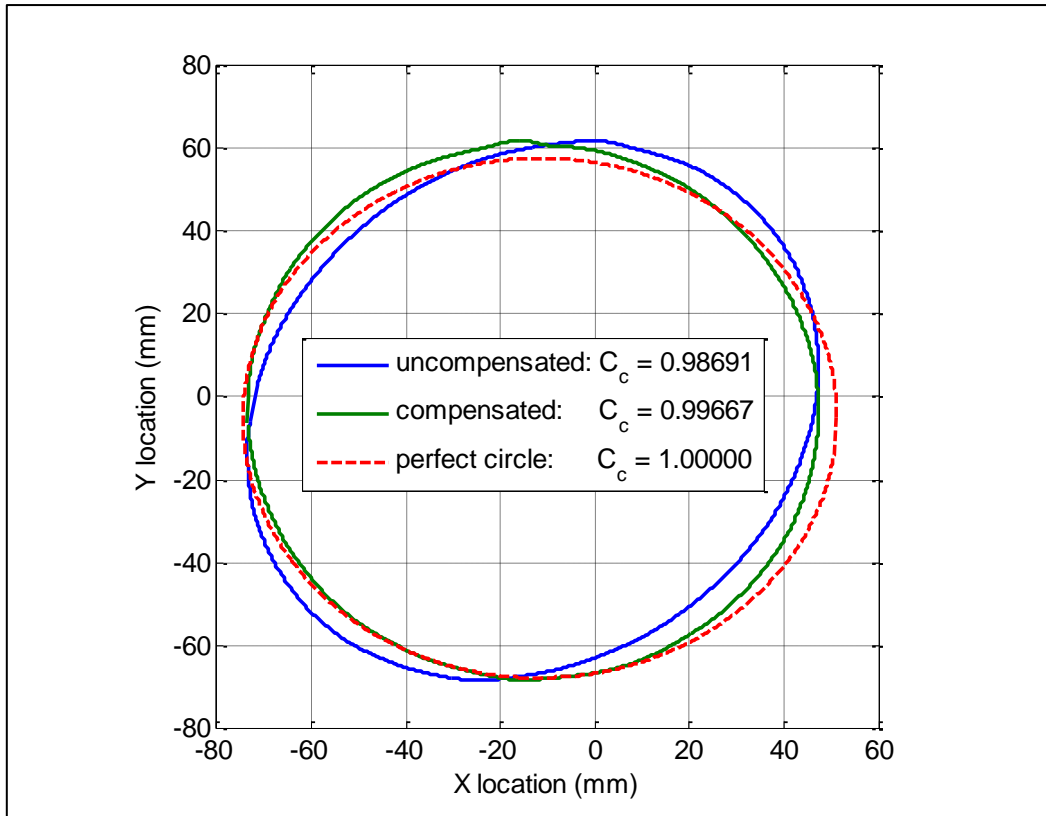


Figure 30: Effect of phase compensation on the laser scanning path (25 Hz)

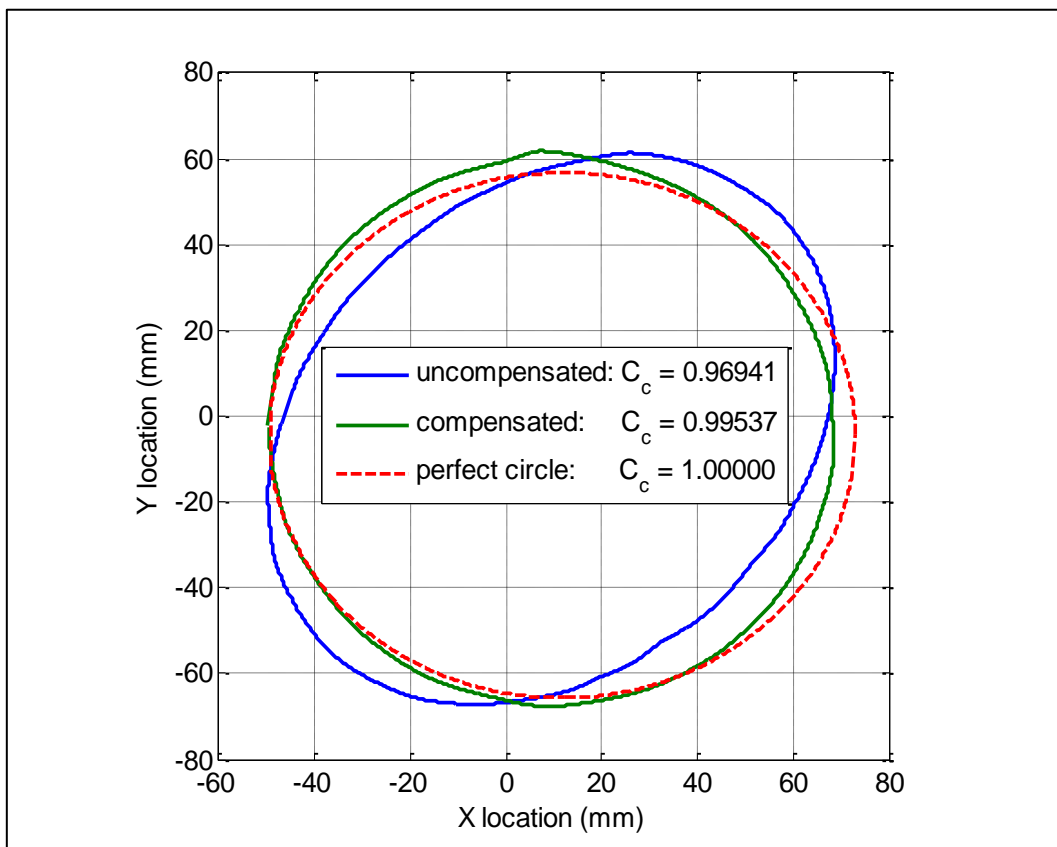


Figure 31: Effect of phase compensation on the laser scanning path (40 Hz)

In the above plots, laser dot scanning paths were all obtained by manually adding identification points in PONTOS, thus the lack of smoothness in the paths noticeable at the top of the graphs. This is in no way an indication of either how accurate the used PONTOS system was, or the performance of the employed mirror dynamic characterization system. The results recorded without manually adding the identification points for 15 Hz scanning frequency, presented in Figure 32, are smooth.

From the results presented above, the uncompensated scanning path becomes more elliptical as the frequency is increased from 20 Hz, to 25 Hz, and finally to 40 Hz. The circularity constants of the uncompensated scanning paths decrease from 0.9866 for 20 Hz to 0.96941 for 40 Hz (about 1.719% decrease in  $C_c$ ). For 20 Hz, the circularity constant is 0.031% less accurate than that for 25 Hz, which conflicts with the expected trend. This can be explained through observing how smooth the 20 Hz and 25 Hz results are, after manually adding identification points in PONTOS. From Figures 29 and 30, it is evident that the inaccuracy in 20 Hz is more than that in 25 Hz, hence the apparent less circular scanning path.

Also from Figures 29 to 31, it can be observed that compensating for the phase of the X mirror creates a more circular scanning path. For all the different scanning frequencies considered, the circularity constant approaches 1 with phase compensation implemented. Using a look-up table generated from characterization of the mirrors done using a frequency sweep up to 20 Hz, it was possible to improve the scanning paths even for a scanning frequency of 40 Hz. This serves to show how robust the employed circular scanning system was. Thus it was valid to assume that the phase frequency response variation of the X mirror is linear for frequencies higher than 20 Hz.

From the results presented above, it is clear that scanning paths obtained after phase compensation did not perfectly agree with reference circles also plotted in the figures. The scanning radii in the y-directions are slightly larger than those in the x-directions. This can be a result of the voltage required to tilt the X mirror by a particular angle not being similar to that required to tilt the Y mirror by the same angle. The same aspect is evident in the FRF magnitude variation with frequency, indicated in Figure 26 presented earlier. The magnitude response of the X mirror is less than that of the Y mirror. Adjusting the amplitude of the voltage signals supplied to the mirrors was thus necessary.

From Figure 26, a ratio of 1.05879 can be calculated for the different mirrors magnitude responses to actuation. Thus if the X-mirror's voltage amplitudes were multiplied by a factor of 1.05879, a better circular scan could be obtained. For the X-mirror, instead of using Equation (1.7) to calculate the amplitude of the actuating voltage signal, Equation (3.3) was then used.

$$\varphi_{s_x}(t) = 0.5294 \tan^{-1}\left(\frac{r_s}{z_0 + d_s}\right) \quad (3.3)$$

Given in Figures 32 to 34 are the results obtained when both amplitude and phase were compensated for.

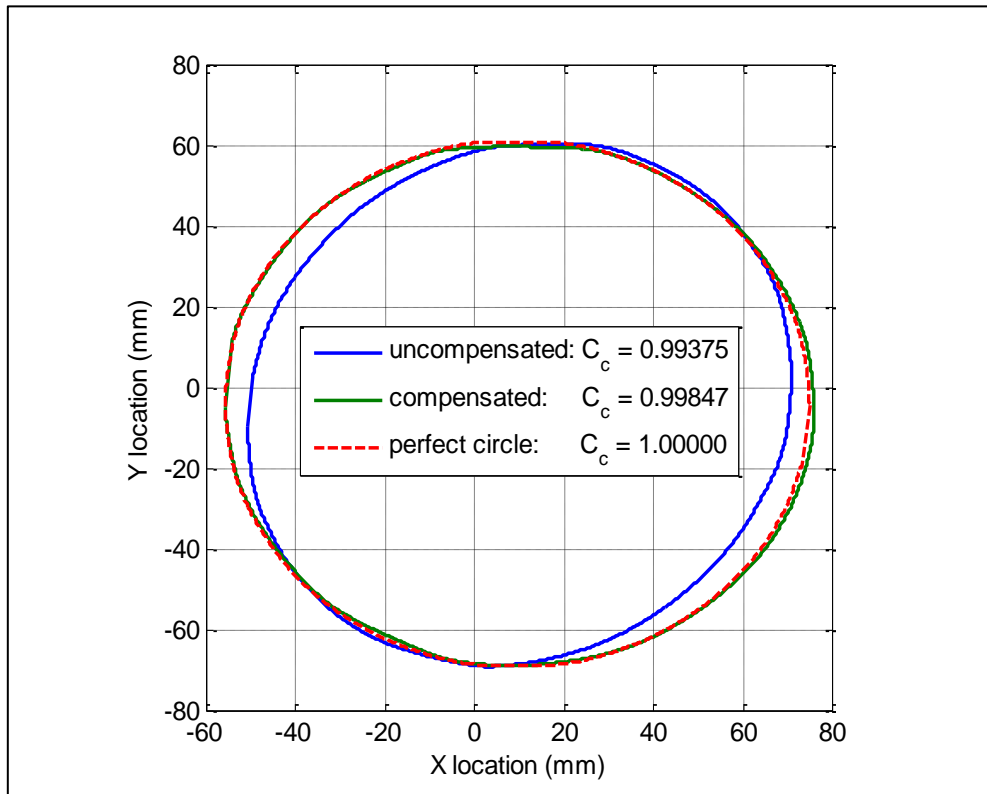


Figure 32: Effect of phase and amplitude compensation on the laser scanning path (15 Hz)

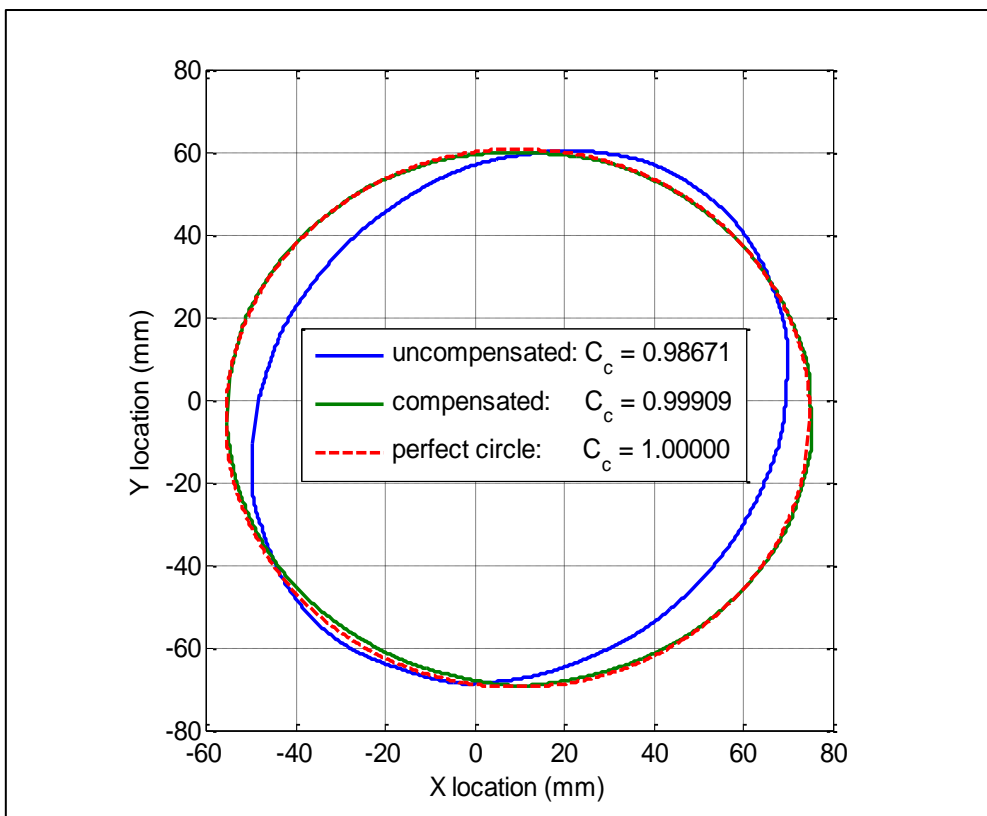
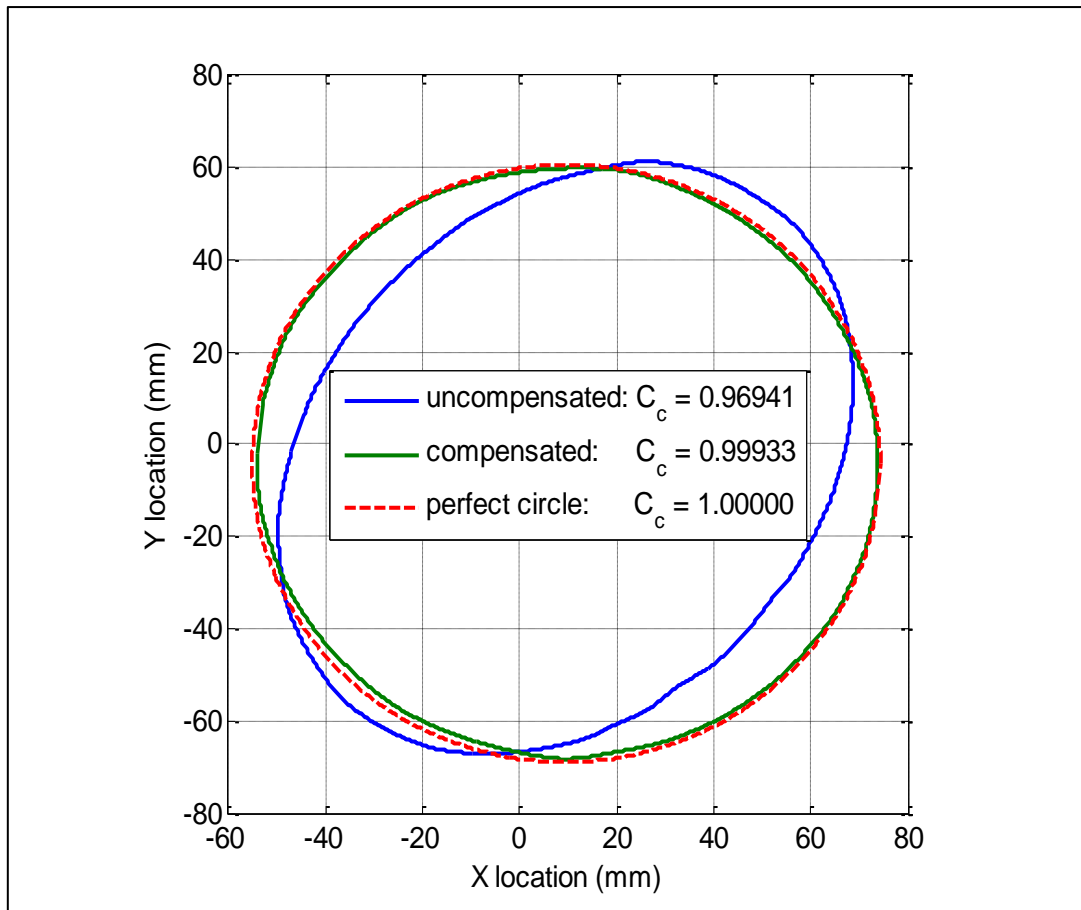


Figure 33: Effect of phase and amplitude compensation on the laser scanning path (25 Hz)



**Figure 34: Effect of phase and amplitude compensation on the laser scanning path (40 Hz)**

The results above indicate that the scanning path now approximates a perfect circle better. For all the three scanning frequencies considered, visually the scanning paths are very close to perfect circle. Table 6 shows how the compensation reduces the circularity constant percentage errors for the three scanning frequencies.

**Table 6: Effect of signal amplitude and phase compensation on circularity constant percentage error**

| Scanning frequency | Uncompensated percentage error (%) | Compensated percentage error (%) |
|--------------------|------------------------------------|----------------------------------|
| 15 Hz              | 0.625                              | 0.0153                           |
| 25 Hz              | 1.329                              | 0.091                            |
| 40 Hz              | 3.059                              | 0.067                            |

### 3.3 INVESTIGATION OF THE PRESENCE OF MISALIGNMENT

Considering Figure 25, it can be noted that some linear misalignment was present when the results were captured, as indicated by the non-constant z-values in the DIC results. A 3D plot of a circular scan is shown in Figure 35(a).

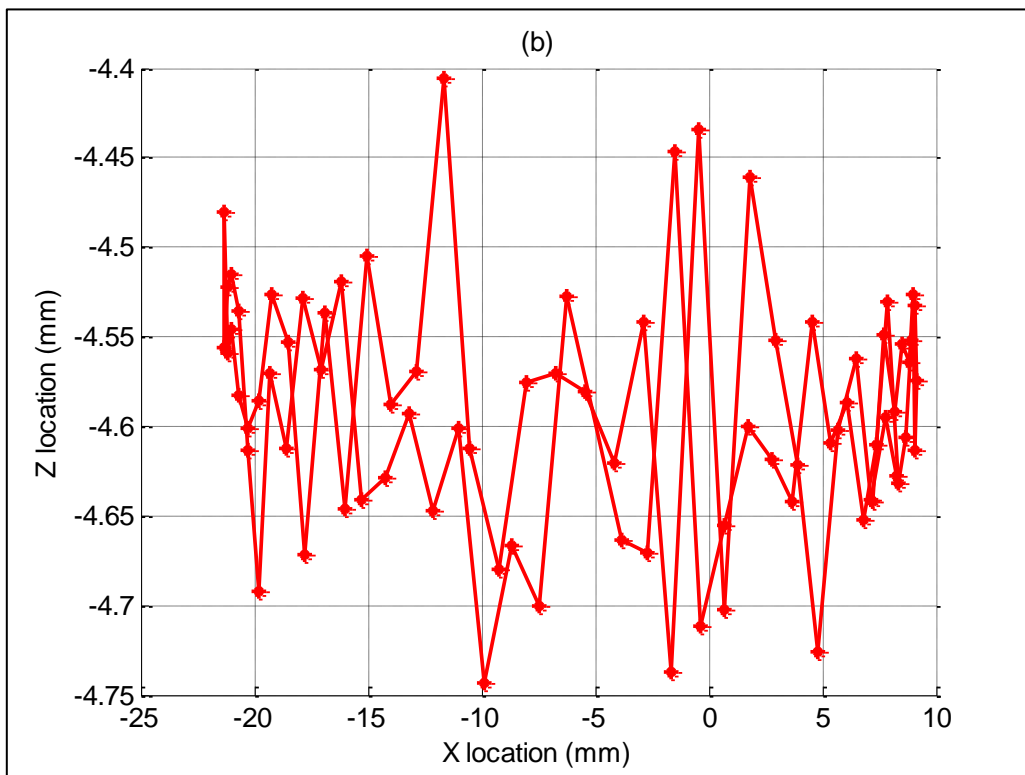
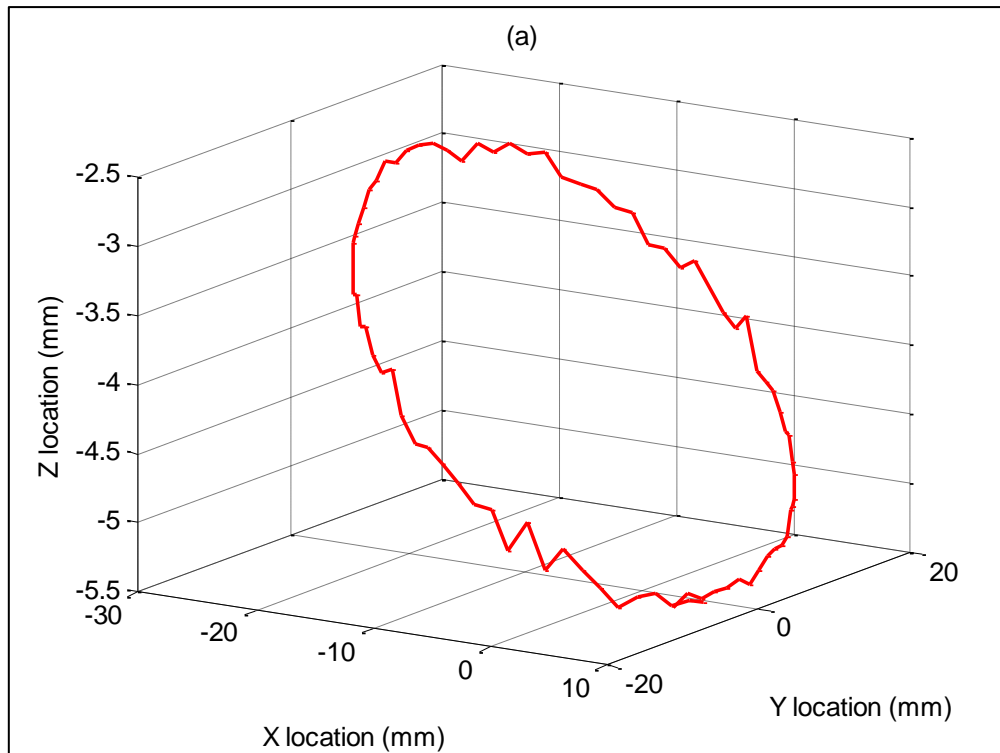


Figure 35: 0-20 Hz frequency sweep (a) scanning head misalignment 3D plot, (b) X-Z view for compensated z-direction misalignment

The non-constant z-values can be clearly observed in Figure 35(a). Figure 35(b) illustrates the noise in the z-direction for the same circular scan, if a compensation for the misalignment is implemented. The noise in the z-direction (a difference of 0.3378 mm

between the maximum and minimum z-displacements) can be attributed to an un-even black paint application on the glass panel.

Since scanning paths were being compared to a perfect reference circle assumed to be perfectly aligned to the Laser Vibrometer scanning head, it was necessary to investigate this misalignment further when testing the performance of the developed TLDV system.

In a perfectly aligned setup in which the scanning path is described in the XY-plane, the z-values must be constant, and an X-Z view of the plot will not be a slanted line, such as the one shown in the top right graph of Figure 36. Looking at the same top right plot, the fact that the paths for the two half circles in the original compensated scan do not lie directly on top of each other in the same X-Z view indicates that the target also needed to be rotated about the x-axis to be perfectly aligned to the scanning head.

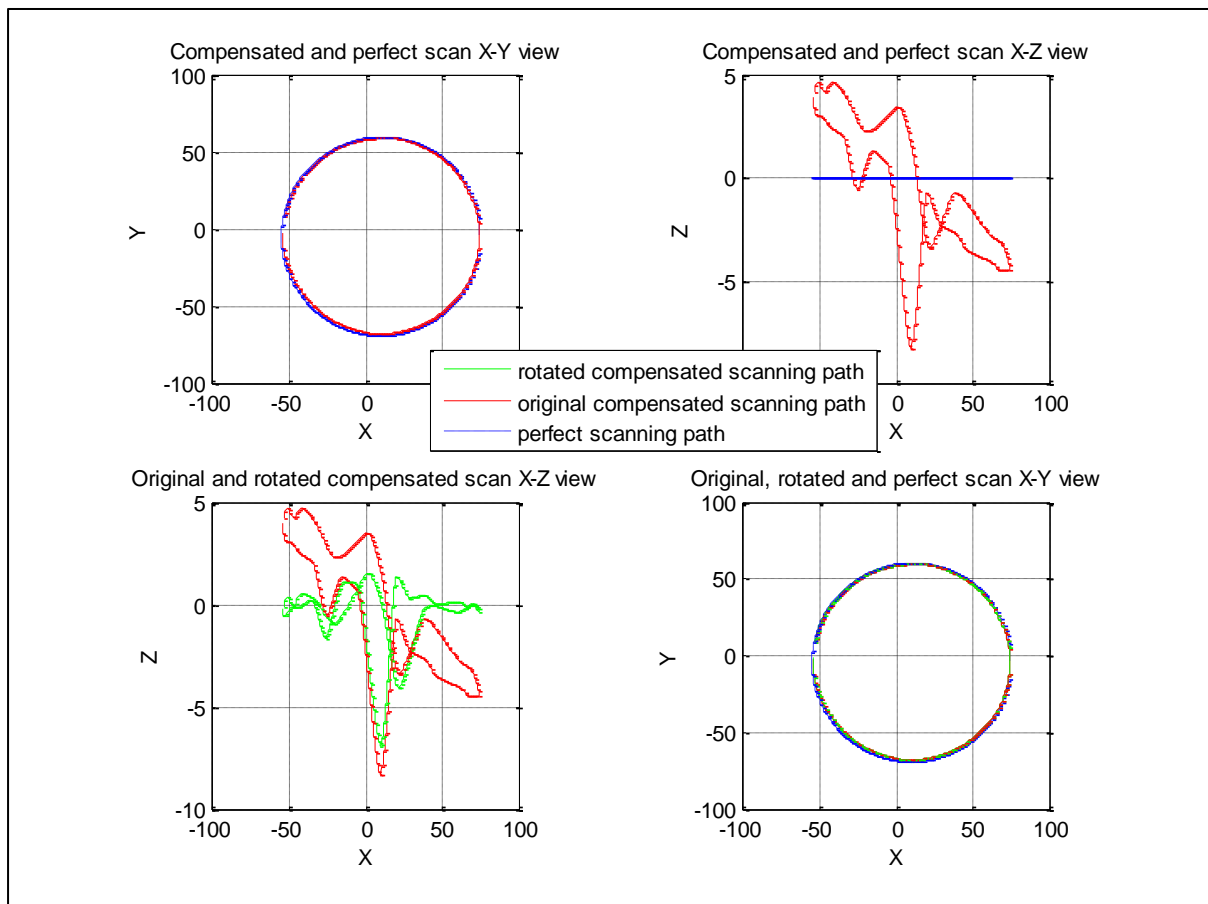


**Figure 36: Investigation and compensation for scanning head misalignment (40 Hz scanning frequency)**

In the Figure 36, the bottom left plot shows that the scanning path can be rotated by approximately  $3.7^\circ$  about the y-axis, and by approximately  $1.3^\circ$  about the x-axis situated at the centre point of the scanning path to obtain results for a perfectly aligned setup. The bottom right graph indicates that the misalignment angles of  $3.7^\circ$  and  $1.3^\circ$  are small enough to consider the setup, used to investigate the dynamics of the scanning system, as adequate to give accurate results with an assumption that the setup is perfectly aligned. In this XY-view, the original scanning path and the calculated scanning path, that accounts for the misalignment lie directly on top of each other.

Figures 35 and 36 can be used to illustrate the effect of manually adding identification points in PONTOS. For Figure 35, identification points were automatically determined by the software, and the z-direction noise in the data is less than that in Figure 36 (top right corner plot) for which identification points were added manually. Thus errors introduced by manually adding identification points are more significant in the z-direction displacements.

### 3.4 VALIDATION OF 3DPT AS A METHOD FOR CHARACTERIZING THE DYNAMICS OF ROTATING STRUCTURES

#### 3.4.1 EXPERIMENTAL SETUP

To validate the 3DPT results using TLDV, Photron FASTCAM SA4 cameras, 16GB memory model were used. The cameras were made available for this investigation by Mr Reinecke, of the CSIR DPSS Landward Sciences group. These have a capability of capturing 3600 FPS at full resolution (1,024 × 1,024 pixels), and 500 000 FPS at minimum resolution (128 × 16 pixels). The cameras were positioned on either side of the laser scanning head, at angles such that the entire housing of the blisk could be captured by both cameras. Clamps were used to ensure that the cameras would not move relative each other during and after calibration of the system. As mentioned previously, the cameras and the scanning head were not on the same bench as the motor and the blisk. This was done to ensure that blisk vibrations were not going to be transmitted to the cameras.

The PSV 300 scanning Laser Vibrometer used had a sensitivity of 5.12 mm/V. Instead of measuring velocities through transformation of a Doppler frequency into a voltage which is proportional to velocity, displacements were being measured directly using the vibrometer. This was more favourable since the results being captured had to be correlated to 3DPT displacements. Thus integration of velocities to displacements could be avoided. Figure 37 is a photo of the setup.



Figure 37: Positioning of the cameras and the laser scanning head

For the measurements, the cameras were set to record at 3600 FPS, with a shutter speed of 1/8000 of a second. With an on-board memory of approximately 16GB, 10918 images could be recorded at maximum resolution. Full resolution had to be used to capture the entire blisk and its housing, and longer measurement duration was understandably required in this case. With a maximum rotational speed of 1500 RPM of the motor, a sampling rate of 3600 FPS was sufficient. This means that the measurement duration was about 3.0328 s. A focal length of 70 mm was set for both of the camera lenses, and FASTCAM software was used to control the cameras. A single laptop was used to monitor both of the cameras through the use of a switch hub. The cameras were synchronized as DIC was to be used to analyse the images using the GOM software PONTOS.

Calibration of the cameras was done using the 350 (Aluminium) standard GOM manufactured calibration panel (ID: CP20/35/D09271). With this panel, a series of external images in conjunction with PONTOS were used to do the calibration. The panel was placed in front of the blisk housing, and images were captured one at a time as the orientation of the panel relative to the cameras was varied.

Shown in Figure 38 is the complete experimental setup.

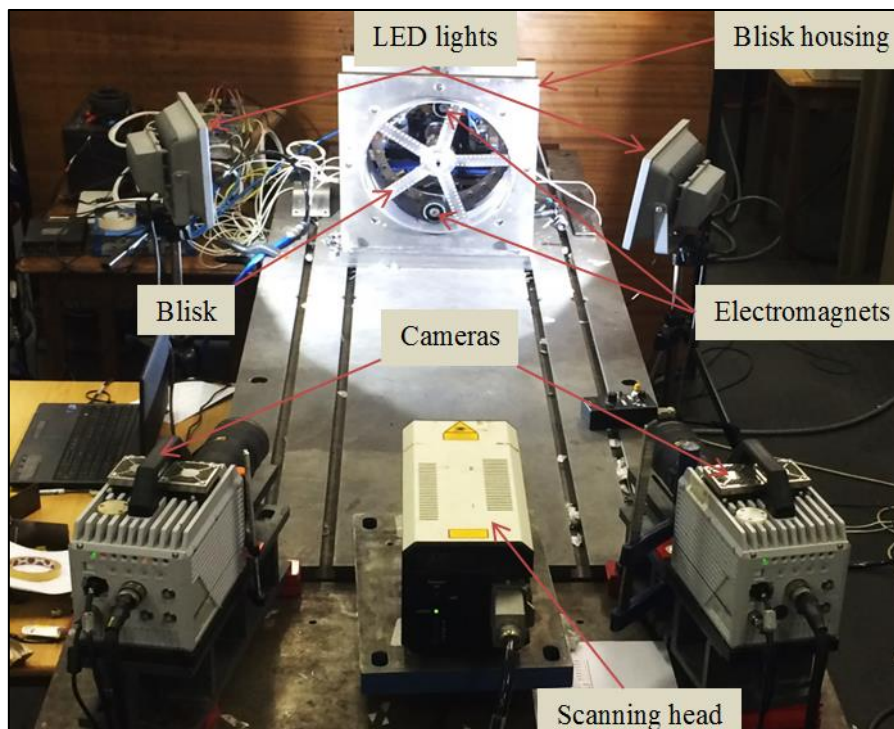
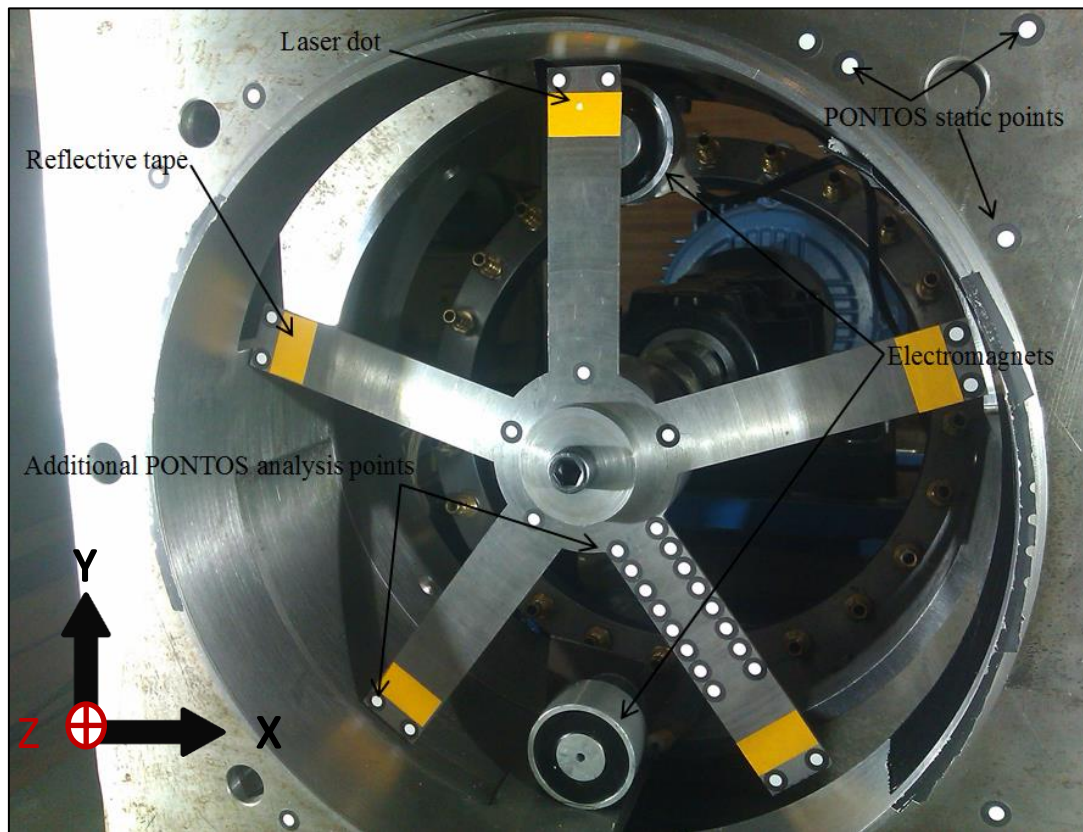


Figure 38: Complete experimental setup

Since the shutter speed was fractional, it was necessary to use the LED lights to enhance the amount of light let through the camera lenses. In the section of the laboratory where the testing was conducted, the windows were painted, thus limiting ambient light. Switching off the overhead lights in the room and using just the LED lights allowed for better control of the lighting.

The laser dot was focused on reflective tape attached to one of the blades. Static points with reference to which displacements are calculated in PONTOS were added to the blisk

housing, and additional analysis points were added to the blisk as at least three points are required by for analysis by the software. Figure 39 is a photo of this setup.



**Figure 39: Blisk and scanning laser dot for 3DPT validation using TLDV**

Two separate computers were used for this investigation. One was used to control the position of the laser, and the other, to control the cameras and record the displacement and velocity measurements from the scanning head. Figure 40 is a schematic drawing of the setup.

The speed of the motor was controlled by a DC voltage, supplied to the motor control unit using a NI cDAQ-9178 that was connected to a computer via a USB cable. The speed of the motor was continuously measured using a shaft encoder. To achieve better synchronization with the frequency of rotation of the laser beam, the measured rotational speed at any instant was used as the frequency of one period on the sinusoidal signals supplied to the scanning mirrors at that instant. Thus before outputting a single period of actuating harmonic signals to the scanning mirrors, the instantaneous speed of the rotor was measured, and this used as the scanning frequency for the mirrors. Measurements could be captured for duration of no longer than 3.0328 s (3600 FPS for the 16 GB Photron SA4 model). Also the measurement process was focused on comparing the TLDV out-of-plane measurements to the 3DPT measurements of the same laser beam, not TLDV measurements of a specific blade position. In light of this, slight movements of the beam on the blade due to non-perfect synchronization between the rotor and the scanning system were acceptable. An open-loop control system was therefore employed to focus the laser beam on the blade. The position of the laser beam as detected by cameras was not used to control the motion of the scanning mirrors. This would have made the system a closed-loop image based tracking system, which was not the focus of this study.

It is worth mentioning that for applications where perfect tracking is needed and TLDV measurements are to be captured for a specific blade position (ODS analysis for instance) one can however use a pulse-train rate from a shaft encoder to dictate the outputting sequence of actuating signals to the mirrors. This would ensure better synchronization in cases of varying rotor speed.

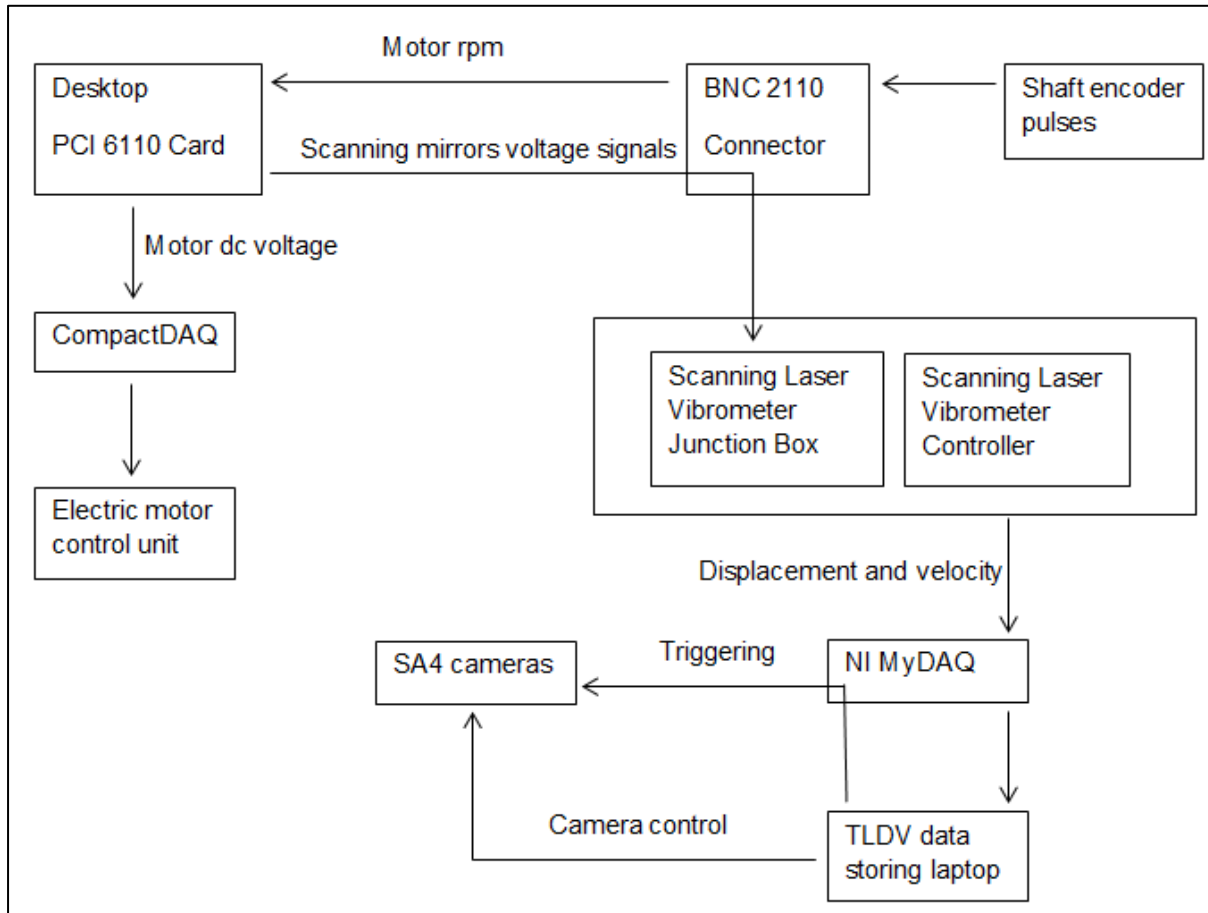


Figure 40: Schematic drawing of experimental setup for 3DPT validation using TLDV

The SA4 Photron cameras were used to track the laser dot focused on one of the blades. The system was synchronized to ensure that displacement signals from the TLDV were recorded starting from the moment the cameras were triggered to capture the images. Thus the same trigger signal was used to initiate data capturing of TLDV displacement voltage signals and to initiate image capturing with the SA4s.

The validation was completed for the scenario where the blades were excited with two electromagnets, and rotating at 992 RPM. At this rotational speed, an ODS similar to the first bending mode of the blisk blades could be obtained, as illustrated from the results presented in the following section.

### 3.4.2 PHOTOGRAMMETRIC DISPLACEMENT MEASUREMENTS OF A LASER DOT FOCUSED ON A ROTATING BLADE

Using the experimental setup described above, a laser dot focused on a rotating blade under excitation was tracked using 3DPT. The analysis procedure and post processing of the results conducted was as follows.

For the setup used, an effort was made to eliminate the misalignment illustrated in Figure 41.

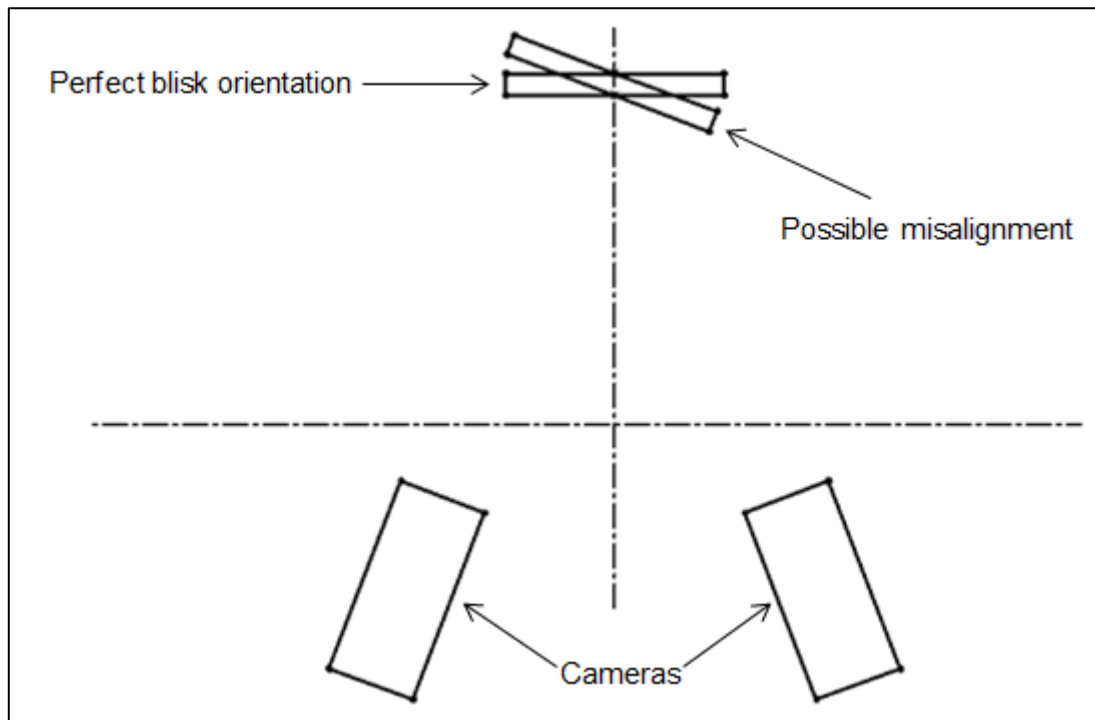
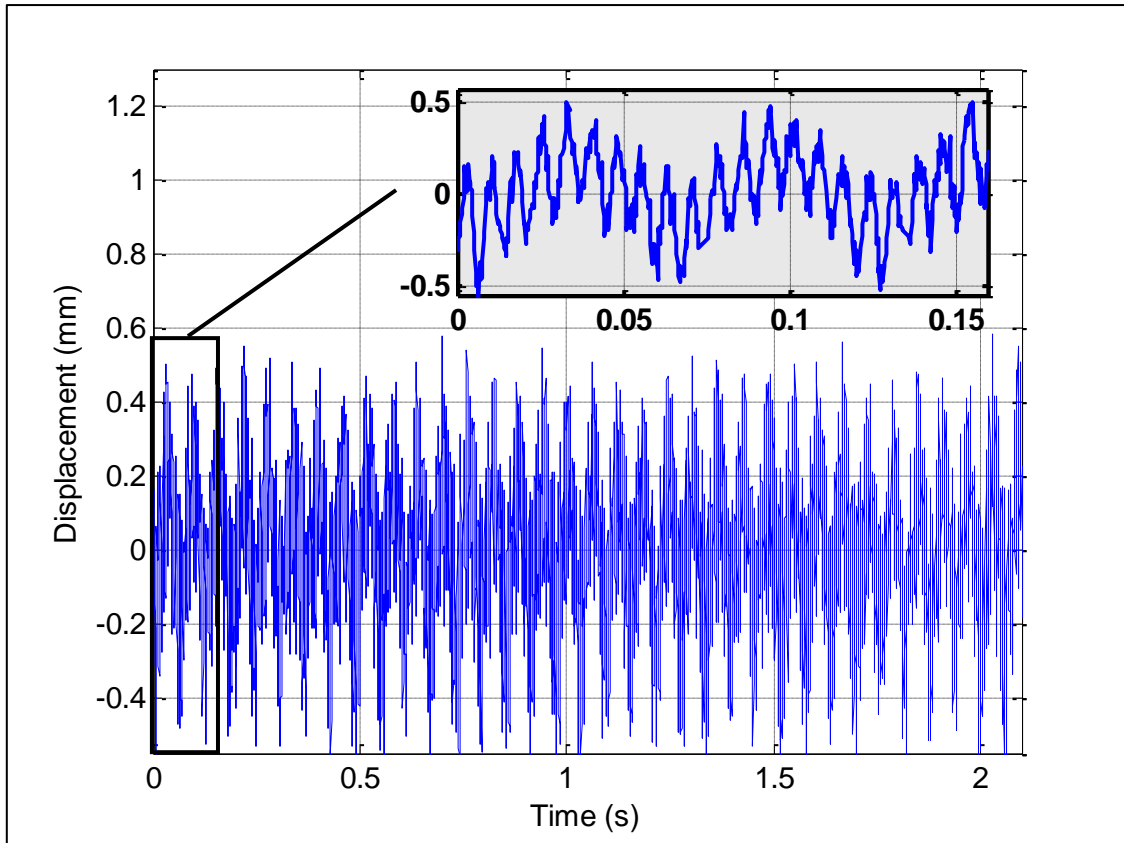


Figure 41: Alignment of the cameras with the blisk

Obviously perfect alignment cannot be achieved, and so a new coordinate system had to be created to transform the captured 3DPT displacements into an x-y plane that coincided with that of the blades. To conduct this transformation, three markers attached to the disk of the blisk, together with static points placed on the housing were used to define the new coordinate system in PONTOS. This was done before exporting displacement profiles from PONTOS for post processing.

When using DIC to analyse dynamic behaviour, usually displacement profiles captured do not include evenly spaced data, as some analysis stages of a point of interest might be missing. This results from the image processing software not being able to track and identify the point of interest in some of the captured stages. This can be addressed by using simple linear interpolation to fit in data at the missing time stages.

With this interpolation conducted, the out-of-plane displacement of the laser dot captured using DIC at 992 RPM blisk rotational speed is shown in Figure 42. A zoomed in section of the displacement profile is also presented.



**Figure 42: 3DPT out-of-plane displacements**

From Figure 42, 3DPT z-displacements of the laser dot had a low frequency sinusoidal component associated with them. From investigations presented in Figure 43, this low frequency was at 16.6 Hz.

To investigate whether this sinusoidal component was also part of the out-of-plane blade vibration, or whether this resulted from misalignment between the cameras and the blisk, in-plane displacements of the laser dot (given as 3DPT y-displacements, direction illustrated in Figure 39) were also analysed in the frequency domain. The Fast Fourier Transform (FFT) spectra of the two signals, displayed in RMS units are given in Figure 43. Since the sampling frequency was 3600 FPS, a frequency band up to 1800 Hz could be obtained, but only a range of 0 – 300 Hz is shown below for better presentation and visualization of the results (no noticeable peaks after 300 Hz).

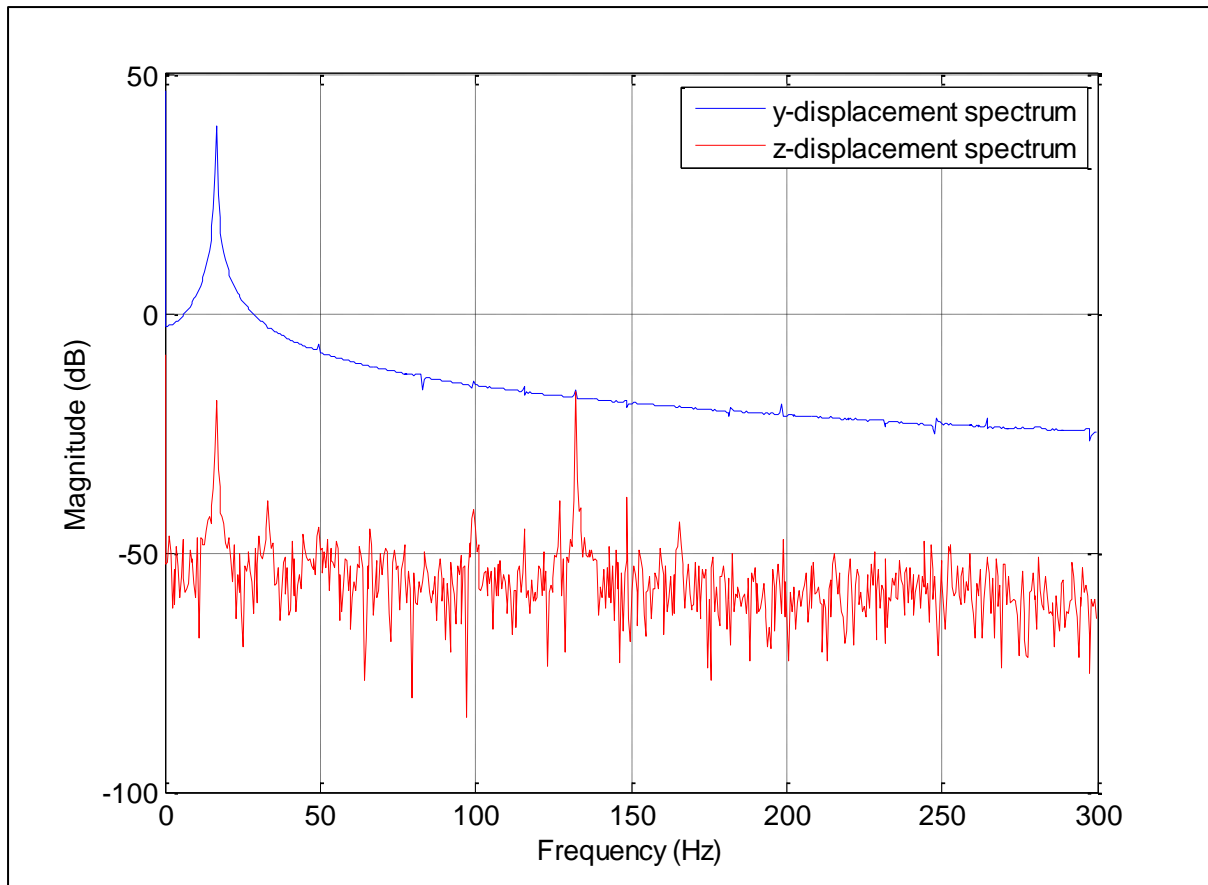


Figure 43: 3DPT y-and z-response spectra

In Figure 43, both y-displacements and z-displacements have a frequency component at approximately 16.6 Hz. This value is very close to the frequency at which the laser dot and the blisk were being rotated (16.533 Hz). Thus the distance between the cameras and laser beam point on the surface of the blade changes in a sinusoidal way at a frequency that corresponds to the rotational speed.

This then implies that this frequency component was a result of translational misalignment between the blisk and the cameras, as it appears in the y-displacement spectrum as well. This indicates that the coordinate transformation implemented during the image processing, to try and compensate for the misalignment, was not 100% effective. It can be concluded that the plane of the blisk casing, where static points used to create a new coordinate system for coordinate transformation in PONTOS, was not parallel to the x-y plane of the blisk.

Also in Figure 43, another peak at 132.2 Hz can be observed in the z-displacement spectrum. From a Finite Element (FE) analysis of a model updated numerical representation of the blisk, a Campbell diagram developed predicted that the first bending mode natural frequency of the blisk (139.6 Hz) can be excited at 837.75 RPM. Thus the peak at 132.2 Hz can be attributed to the out-of-plane vibration of the blade due to excitation from the two electromagnets at 992 RPM rotor rotational speed.

### 3.4.3 TLDV DISPLACEMENT MEASUREMENTS

The out-of-plane displacements captured using the TLDV system are given in Figure 43.

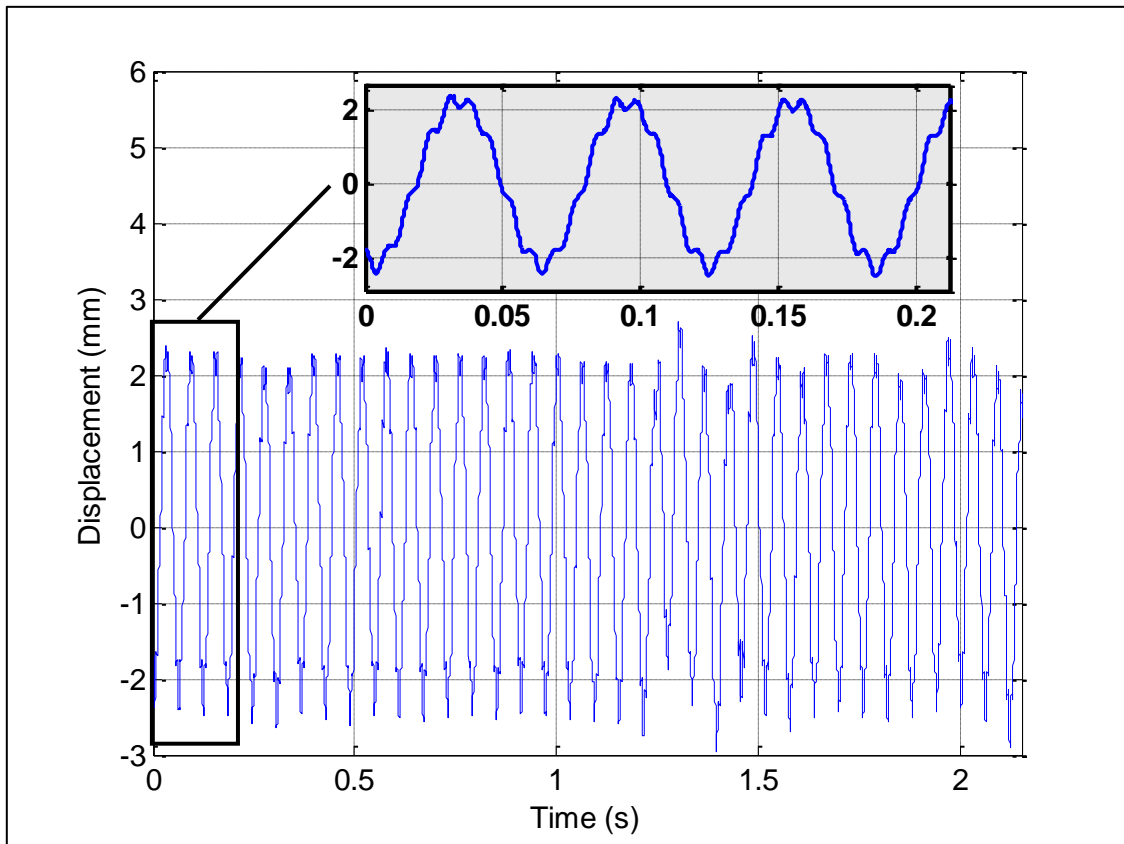


Figure 44: TLDV out-of-plane displacements

Analysing Figure 44, the low frequency sinusoidal nature of the displacement profile indicates that there was also some misalignment between the TLDV scanning head and the blisk. This misalignment was a minor value of approximately 2.5 mm from the blisk plane to a point very close to the tip of the blade (scanning point).

To further investigate this misalignment, TLDV out-of-plane displacements were also captured when there was no excitation from the electromagnets. Results obtained (shown in Figure 45) clearly show this misalignment.

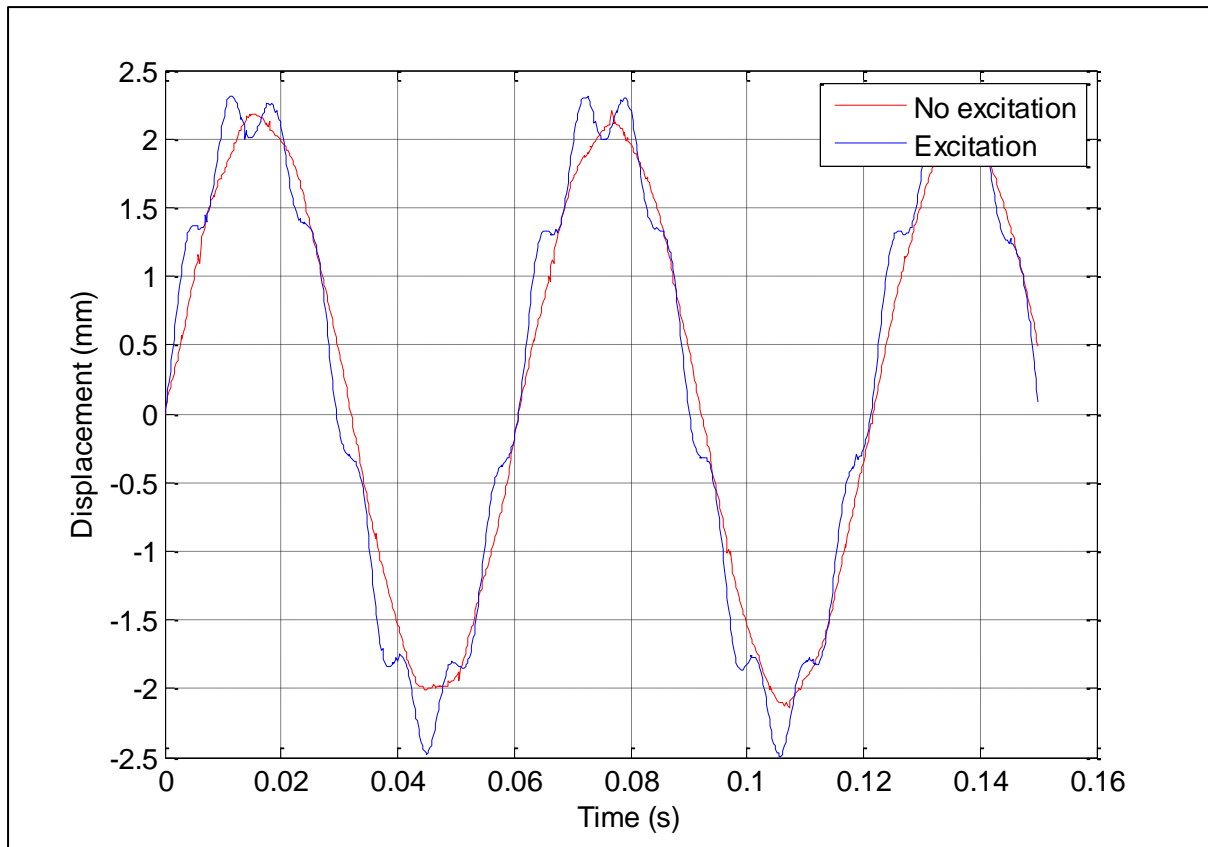


Figure 45: TLDV displacement profiles with and without excitation

The results presented in Figure 45 were captured separately since one scanning head was being used for TLDV measurements. They were then aligned for better representation.

#### 3.4.4 COMPARISON OF 3DPT DISPLACEMENT MEASUREMENTS TO TLDV DISPLACEMENTS

The correlation between 3DPT and TLDV results can be investigated in both the time and the frequency domain. Analysis of the results in the time domain requires that the misalignment in both systems be compensated for. This can be done by filtering out the low frequency components due to the various misalignments. If a designed 10<sup>th</sup> order highpass digital Butterworth filter, with a lower cutoff frequency of 50 Hz (just above the third rotor speed frequency harmonic of 49.6 Hz), is implemented in a zero-phase forward and reverse digital IIR format, 3DPT displacements obtained are given in Figure 46.

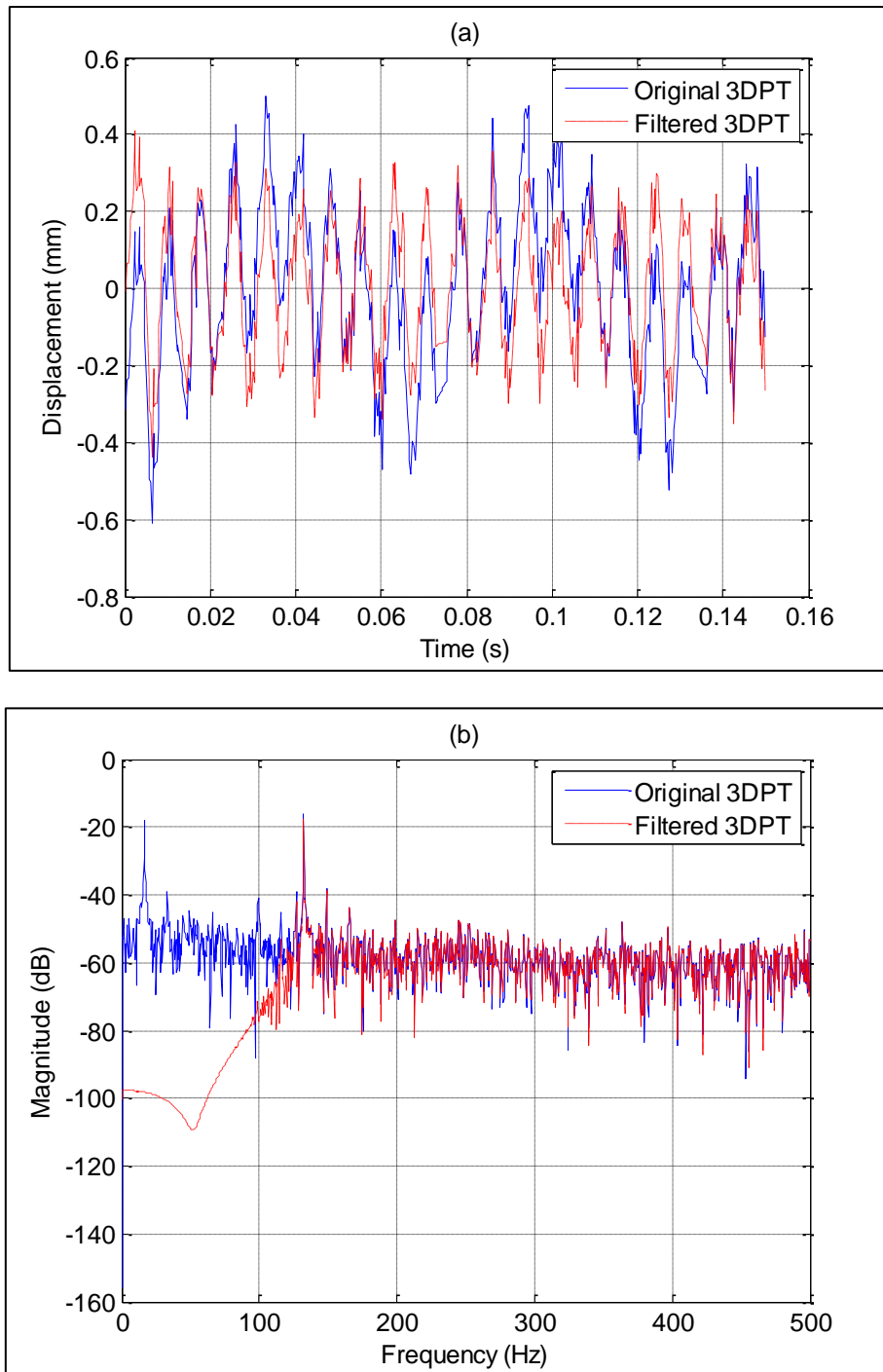


Figure 46: Original and filtered 3DPT displacement profiles, (a) time domain signals (b) frequency domain signals

When the same filter was used to get rid of misalignment effects in the TLDV displacements, the results obtained are presented in Figure 47.

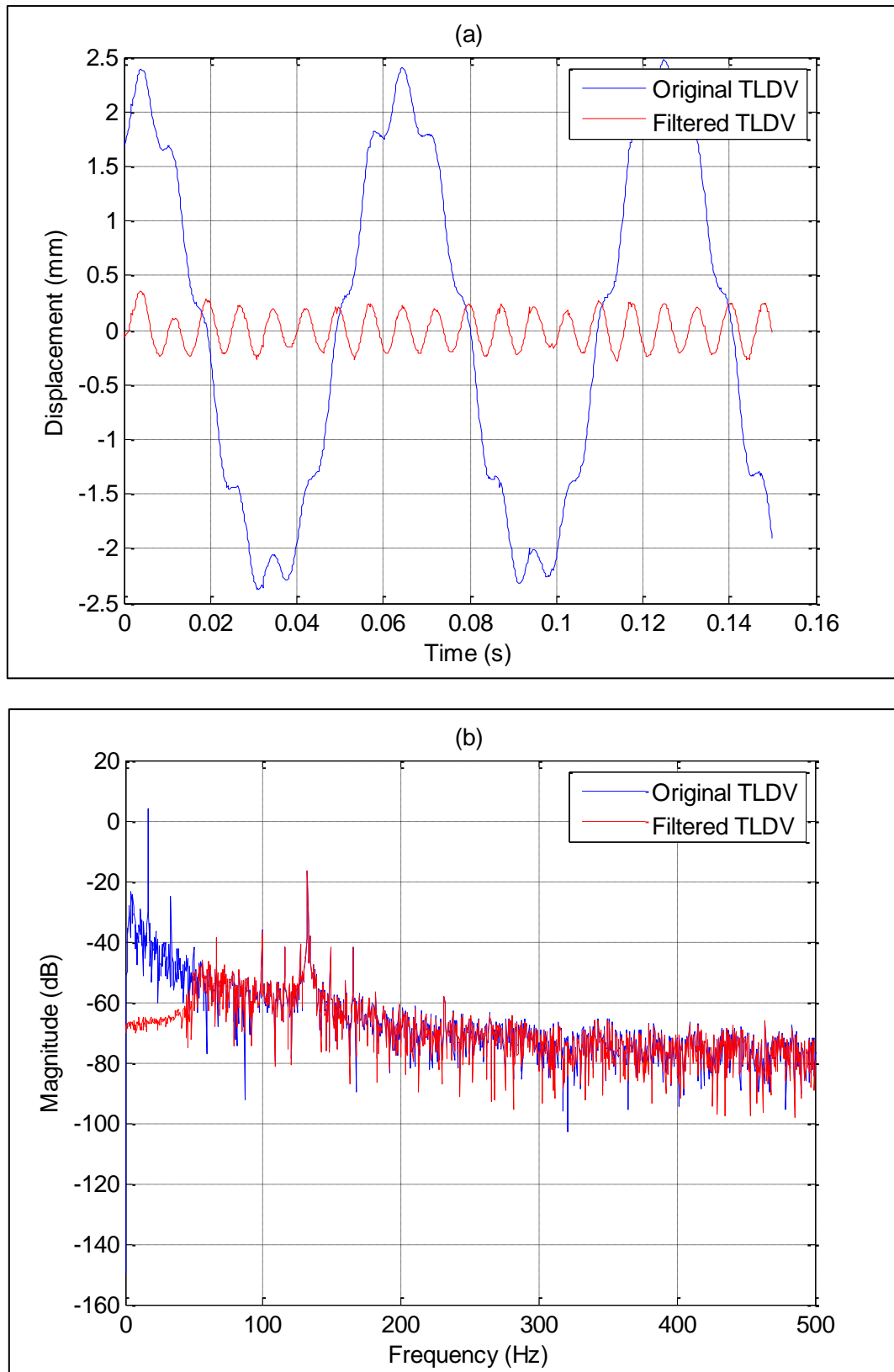
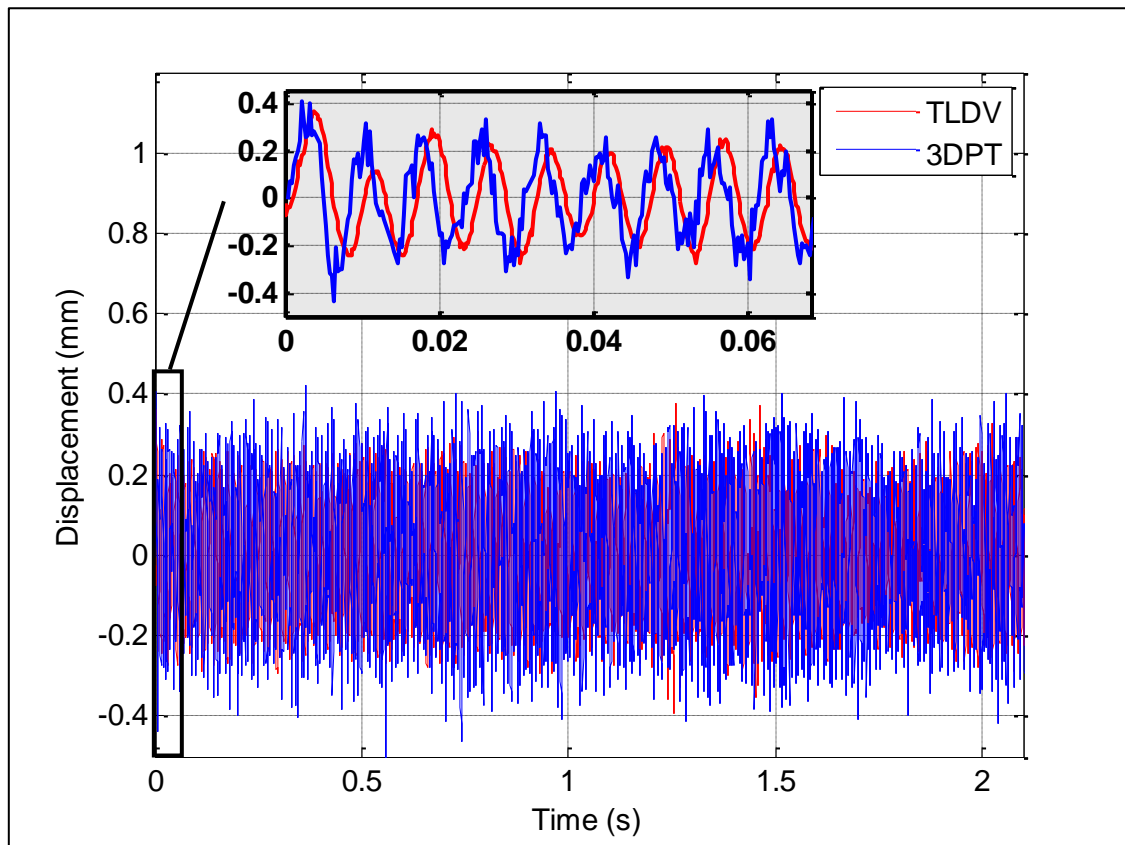


Figure 47: Original and filtered TLDV displacement profiles, (a) time domain signals (b) frequency domain signals

From the results presented in Figures 46 and 47, it can be concluded that an IIR filter can be successfully used to filter out the low frequency components due to misalignment between

the blisk and the instrumentation (high speed cameras and the Laser Vibrometer scanning head). Blisk true vibrations will not be discarded if the cut-off frequencies for the filter are set according to the rotor rotational frequency, as the frequency components due to misalignment are at the rotational frequency and its harmonics.

Presented in Figure 48 are the comparisons of the 3DPT and the TLDV displacement profiles, in the time domain.



**Figure 48: Correlation between 3DPT and TLDV displacement profiles (time domain)**

The displacement profiles captured were very similar to each other, with some amplitude variations. A time delay of approximately 2 ms can also be observed. Since a forward and reverse filtering approach was employed to filter out misalignment, no phase distortion resulting from the filtering process was expected. For this specific high speed imaging application, three factors are expected to contribute to the 3DPT time delay.

- Hardware trigger response time, which is the delay from the instance the cameras are externally triggered to the time an image is actually captured.
- Exposure time, as dictated by the set shutter speed.
- Sensor readout or inter-frame time, during which an image is transferred from sensor to storage prior to new image capture.

From the Photron SA4 cameras hardware specifications (Photron n.d), the general trigger response time is 45 ns, and the sensor readout 667 ns. As mentioned earlier, a shutter speed of 1/8000 s was set for the cameras, implying that the exposure time was 0.1250 ms. Adding these delays together, a compounded delay of 0.1257 ms was expected. From the 2 ms delay, it means that about 1.8743 ms delay in the 3DPT measurements still needed to be

accounted for. This amounts to 6.7474 frames, and is thus not negligible. For this investigation, images were the only data captured by the cameras. Post-processing of these images involved transferring them to a PONTOS system where 3DPT data could be extracted, under the assumption that the first image was captured at time 0 s. Thus without a definite time stamp of the instant the first image is captured after externally triggering the system, further investigation into the source of this delay could not be done.

The time delay between 3DPT and TLDV can however be rectified by recording the TLDV as voltage inputs using the cameras themselves. This would mean that the first TLDV measurement will be captured at the same time instant the first image is captured. The time delay noticed above is constant over the measurement duration, implying that by using the same system for capturing both measurements, no time delay will be expected. The resolution of the measured TLDV signal profiles would however be limited to the cameras sampling rate (3600 FPS in this case). As TLDV was being considered as a validating measurement technique to 3DPT recordings, oversampling of the data was necessary for improved Signal-to-Noise Ratio (SNR) and thus better TLDV recordings. Thus a separate system was used to capture TLDV readings, and not the cameras.

For the specific camera system used, a further investigation to check whether the hardware trigger response time is actually longer than the documented value will have to be conducted. The hardware trigger response is more likely to be the source of the delay as exposure time is dictated by the set shutter speed, and sensor readout inaccuracies are not expected since it was possible to capture images at the specified frame rate (no interference between the frame rate and the speed at which an image is transferred from sensor to storage).

Given in Figure 49 are the 3DPT and TLDV displacement profiles in the frequency domain.

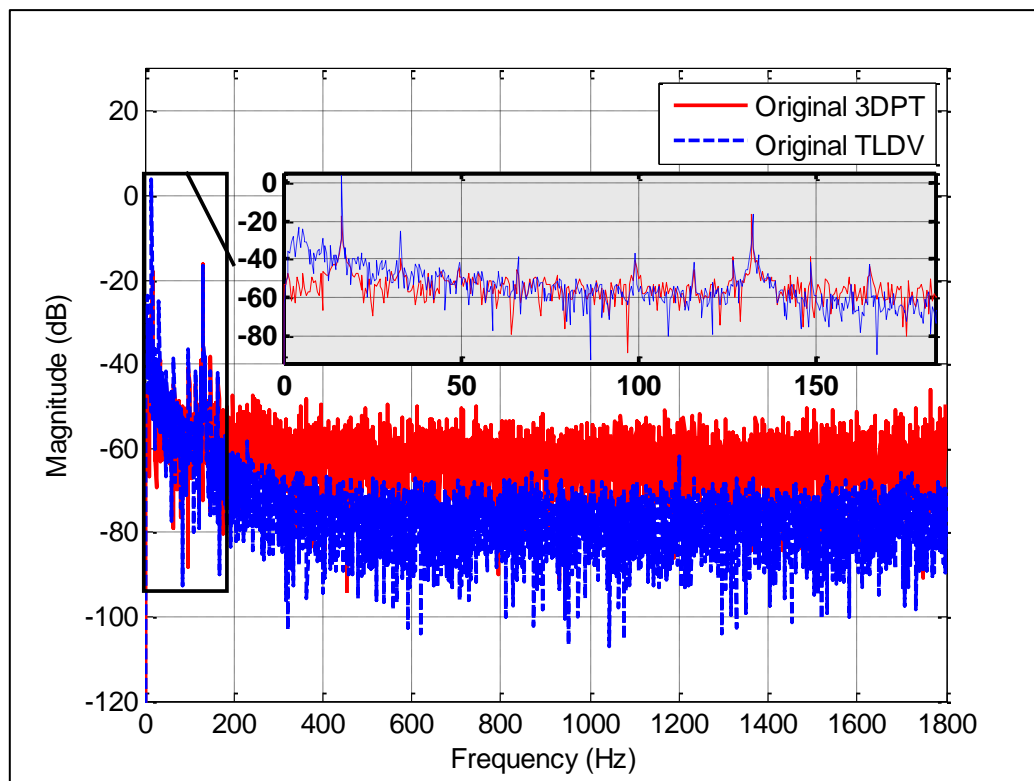


**Figure 49: Correlation between 3DPT and TLDV frequency domain displacement profiles, original data**

From Figure 49, it can be observed that the RMS magnitude peaks due to misalignment and blade vibration occur at the same frequency, for both 3DPT and TLDV. As explained earlier, the misalignment peak is at 16.6 Hz, corresponding to the blisk rotational frequency. The blade vibration frequency is at 132.2 Hz. Misalignment harmonics at 33.2 Hz, 49.8 Hz and 66.4 Hz can also be observed.

There is a more or less constant magnitude difference between the TLDV and the 3DPT data, noticeable at higher frequencies. This can be attributed to the fact that the 3DPT results captured had a lower signal-to-noise ratio, and so the noise effect was more apparent in the data. From Figures 46(a) and 48, it can be noticed that the time resolution of the 3DPT displacements is not as good as that of the TLDV measurements. Thus even though a frame rate of 3600 FPS was good enough for avoiding signal aliasing, a higher frame rate would have meant better time resolution and a higher SNR for the 3DPT. A higher frame rate could not be used for this investigation however, as SA4 Photron cameras have a maximum frame rate of 3600 FPS at maximum camera resolution, and maximum camera resolution was essential for the field of view to be large enough to capture the entire blisk.

Figure 50 shows how well the filtered 3DPT measurements correlate with the filtered TLDV measurements around the frequency band of interest.

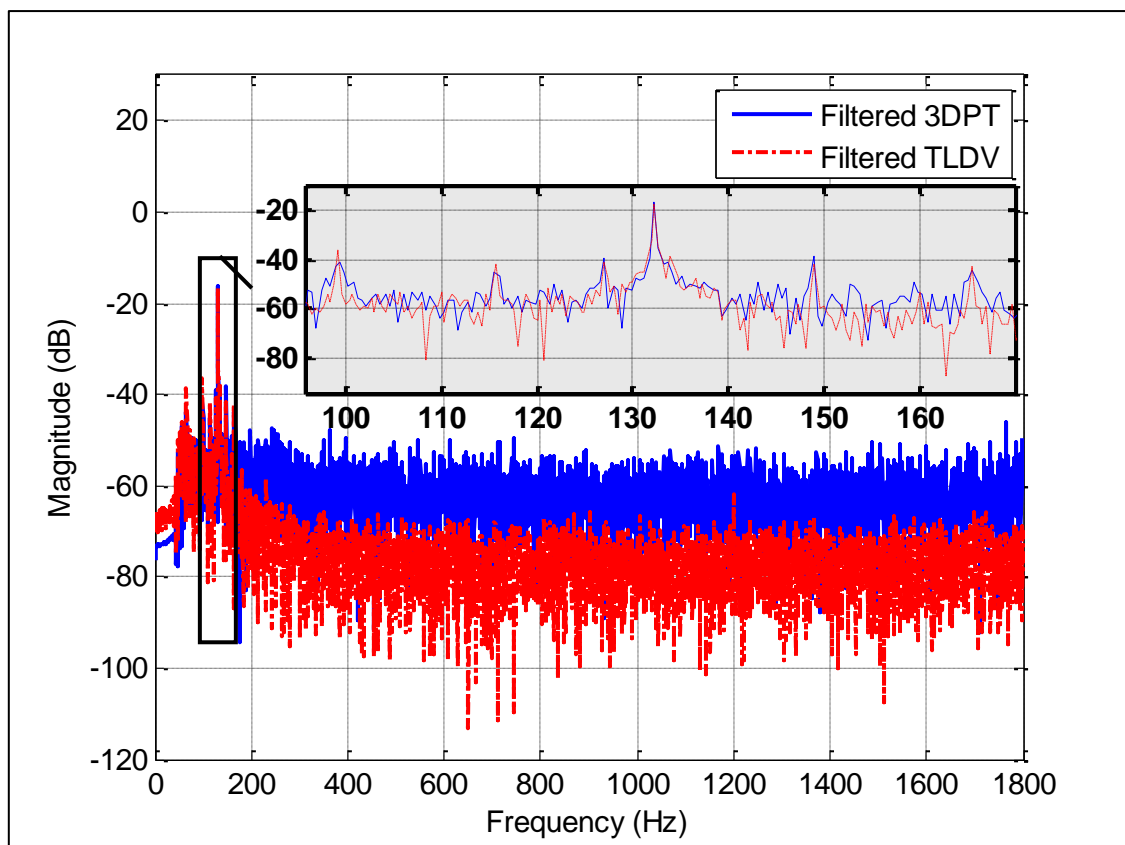


**Figure 50: Correlation between filtered 3DPT and TLDV frequency domain displacement profiles**

Figure 50 shows that the RMS magnitude peaks for both 3DPT and TLDV occur at the same frequency. At the blade vibration frequency (132.2 Hz), good correlation between the 3DPT

and TLDV systems can be observed. Slight discrepancies in the range 90 Hz to 150 Hz are observed, but the peaks in that range all occur at the same frequencies.

From the results presented in this section, it can be concluded that there is quite good correlation between the two non-contact methods of vibration analysis. Variations in the two sets of measurements are attributed to errors introduced due to misalignment effects. With proper use of filters and some signal processing, these errors can be eliminated to get acceptable information from measurements captured using the two optical non-contact techniques.

Although discrepancies due to the contact nature of accelerometers were completely avoided in this investigation through the use of TLDV, variations in the measurements are still observed at higher frequencies. Considering the investigation done by Warren et al. (2010), noise from slip ring systems, mass loading errors, accelerometer cross-axis sensitivities and optical system noise floors were mentioned as possible factors for these variations. This study illustrates that differences in the optical instrumentation noise floors certainly introduces discrepancies at higher frequencies.

After identifying the aspects of 3DPT that need to be addressed to acquire reliable dynamic measurements, the next step was to use this technique to analyse the online dynamics of a turbomachine. Investigations done in this regard are presented in the following chapter of this document.

## CHAPTER 4: USE OF 3DPT FOR ANALYSING THE DYNAMICS OF A ROTATING BLISK

### 4.1 INTRODUCTION

This chapter describes the use of a validated full-field non-contact measurement technique, 3DPT to analyse an online turbomachine. Different ODSs are analysed and animated using PONTOS, and the obtained results are presented. The effect of localized blade excitation is investigated, and how the results obtained can be expanded to the development of damage detection techniques using 3DPT captured ODSs described.

### 4.2 BLISK DYNAMIC ANALYSIS USING 3DPT

With a validated DIC measurement technique, a dynamic analysis of the blisk was then conducted. The ODSs of interest were those similar to the first three out-of-plane bending modes. Table 6 gives the rotational speeds at which the bending modes could be excited, as determined from the already developed numerical Campbell diagram.

**Table 7: Rotational speeds for ODS investigation**

| <b>Bending Mode</b>  | <b>Blisk modal frequency (Hz)</b> | <b>Rotational speed (RPM)</b> |
|----------------------|-----------------------------------|-------------------------------|
| First bending (0ND)  | 138.4 Hz                          | 1332.00                       |
| Second bending (1ND) | 861.8 Hz                          | 783.45                        |
| Third bending (2ND)  | 2409.1 Hz                         | 1417.11                       |

As mentioned earlier, a maximum frame rate of 3600 FPS could be set for the cameras. The blisk ODSs when the different bending modes were being excited can only be accurately captured if the sampling frequency (camera frame rate) is at least twice the blisk modal frequency, as per Nyquist sampling criterion. Thus looking at the modal frequencies given in Table 6, only the first two bending modes could be captured at 3600 FPS. In essence, accurate visualization and animation of blade responses at a particular frequency using photogrammetry software is limited by the set camera frame rate.

To visualize the mode shapes from 3DPT data, two rows of markers were placed on each of the blades, as shown in the Figure 51.

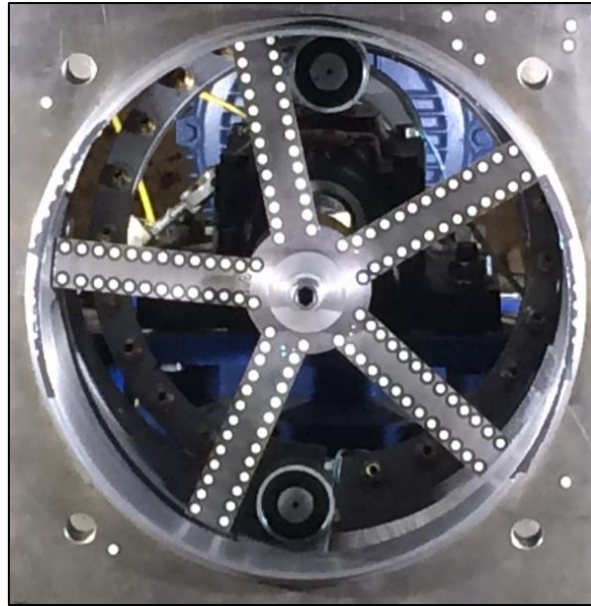


Figure 51: Mode shape investigation using 3DPT

The first bending mode of the blisk could be clearly captured when two electromagnets were exciting the blisk, running at 1332 RPM. Shown in Figures 52 and 53 are different forms of results that could be obtained from PONTOS. Figure 52 is a 3D plot of the displacement profiles recorded for one of the PONTOS analysis stages. Figure 53 is a 2D image illustrating how the displacement results can be superimposed onto the actual blisk image.

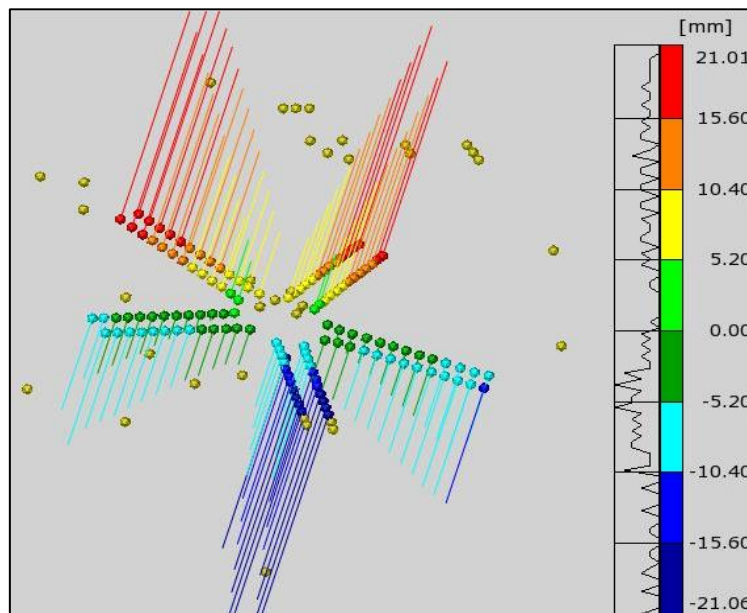


Figure 52: PONTOS 3D mode shape

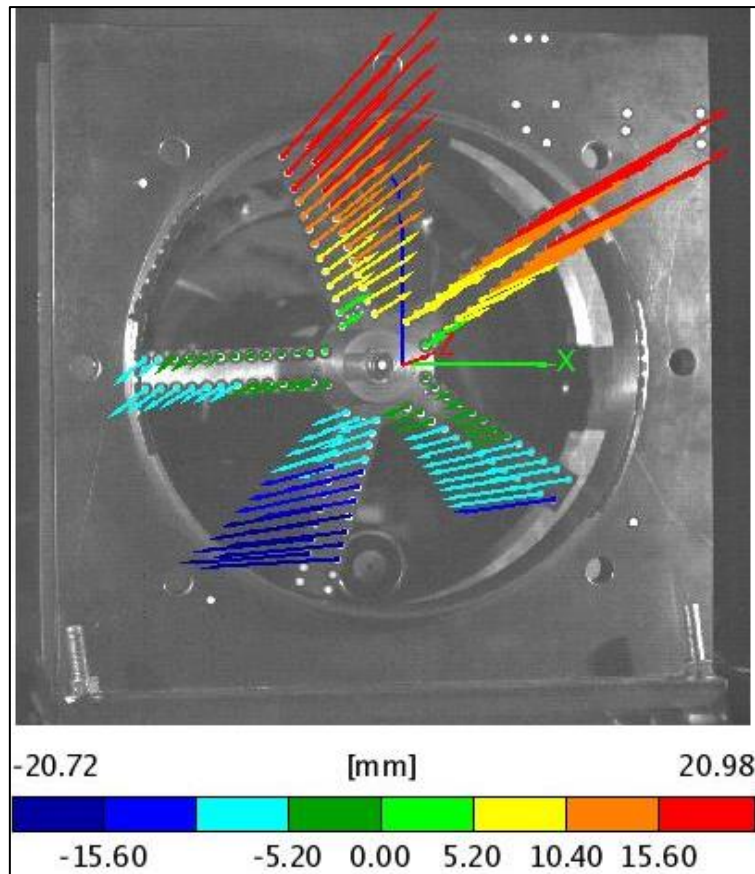


Figure 53: PONTOS 2D mode shape

As can be noted for each blade, the displacements gradually increase from the root to the tip of the blades. Three of the blades are in phase and entirely out of phase with the remaining two. This represents one of the first bending mode variations of the blisk. Different variations of the mode are obtained depending on the phases of the different blades relative to each other.

Investigations were also conducted to see if the second bending mode of the blisk could be captured using 3DPT. In an effort to do this, it was realised that the blades were too stiff and excitation using two electromagnets at a rotor speed highlighted above did not sufficiently excite the mode. Instead of there being clear nodal lines splitting blade motion in separate out-of-plane directions, the general first bending mode ODS effect was apparent in the second bending mode. Thus the stiffness of the blades resulted in responses being characterized by a general umbrella mode motion, with the nodal lines for the higher bending modes moving in and out of plane, instead of being entirely fixed. This was the case even though the excitation frequencies for the different modes were not too close to each other for there to be multiple mode excitations.

Thus because of the blades being generally stiff, excitation of out-of-plane blade bending modes resulted in responses dominated by the umbrella mode ODS, and clear development of nodal diameters on the blade for the second mode would require more excitation energy. This could not be accomplished since the motor only had a maximum rotational speed of 1500 RPM.

Visualization of the expected ODS was apparent in some of the blades for some of the analysis stages. Figure 54 shows a PONTOS stage for an analysis done at 783 RPM, with two electromagnets installed. A pure second bending mode was expected.

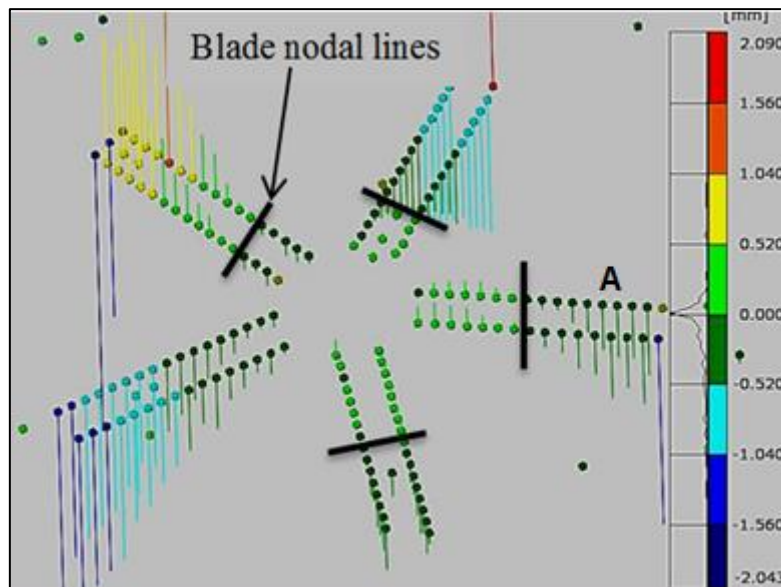


Figure 54: Second bending mode ODS (783.45 RPM)

From the results presented above, it can be observed that clear nodal lines due to the second bending mode are apparent in some of the blades. One of the blades, labelled as 'A' in Figure 54, has a clear pure second bending mode. The results in Figure 54 were for one of the PONTOS analysis stages.

Thus DIC can be successfully used to capture the ODSs of the blades of a turbomachine if a camera frame rate more than twice the response frequency of interest can be set. Also, sufficient blade excitation is necessary if distinct modes are to be visualized and clear nodal lines observed. By being able to capture and visualize ODSs similar to the expected mode shapes if excitation is implemented at the relevant mode excitation frequencies, it means that one can comfortably go on to analyse the actual full-field displacement profiles in an attempt to capture blade vibratory information otherwise not visible from ODS visualisation using PONTOS.

General excitation of the blades can be done with attention not being focused on initiating responses with ODSs similar to various mode shapes. Information from these displacement profiles is especially important when one considers a more practical scenario where a turbomachine is under operation, and blade vibrations are due to unknown excitation forces. Capturing ODSs in such a case, and using that information for damage detection and characterization in the system allows for the expansion of 3DPT to a full-field non-contact method for online condition monitoring of turbomachines.

The ODSs displacement information captured using 3DPT can be analysed to highlight irregularities in blade responses, as described in the following section. These response irregularities along a blade are actually what one would expect if damage is present. Since excitation was accomplished through the use of small electromagnets, blade excitation was

thus localized, and irregularities in responses were thus expected for different points along the blades.

### 4.3 INVESTIGATION OF RESPONSE IRREGULARITIES ALONG A BLADE DUE TO LOCALIZED EXCITATION

To investigate the effects of localized blade excitation, and to determine if this form of excitation introduced irregularities that are similar to those expected from damage, markers were attached about 7.5 mm apart along the blades, and displacement profiles captured using the high speed cameras. A frame rate of 3600 FPS was used for these tests, and investigations were done for an arbitrarily chosen rotational speed of 766 RPM. At this rotor speed, visualization of the blisk response using PONTOS indicated that the blisk ODS was similar to the first bending mode of the blisk. The electromagnets exciting the blades were mounted with their midpoints at about 90 mm from the roots of the blades.

Results were captured firstly when two electromagnets were being used and then when four of them were being used, for the same rotational speed. This was necessary to allow for implementation of a damage detection technique similar to the one suggested by Asnaashari & Sinha (2014). Displacement profiles were obtained for all the seventeen points along the length of the blade. Because these displacements were captured simultaneously, they could be compared to each other to detect response variations along the blade.

With the knowledge that the blades were vibrating out-of-plane at a frequency of about 132 Hz (first bending mode out-of-plane blade vibrational frequency), response information in the range 140 Hz (+/- 15%) was of interest. By analysing the features of the tone with the highest magnitude component in that frequency range when looking at the results in the frequency domain, signal characteristics representative of the out-of-plane vibrations of different points along the blade could be extracted. These features were the amplitude of the tone, the tone frequency, the phase of the tone, and also the basic RMS value of the tone. The phase of the tone is the frequency domain phase corresponding to the frequency of the highest frequency domain magnitude component within the frequency range of interest. Similar information can be obtained using the LabVIEW Tone Measurements Virtual Instrument (VI).

Given in Figures 55 to 58 are the signal properties obtained for each of the points along a blade. Also given is a plot of the basic RMS values of the responses of various points from root to tip of the blades.

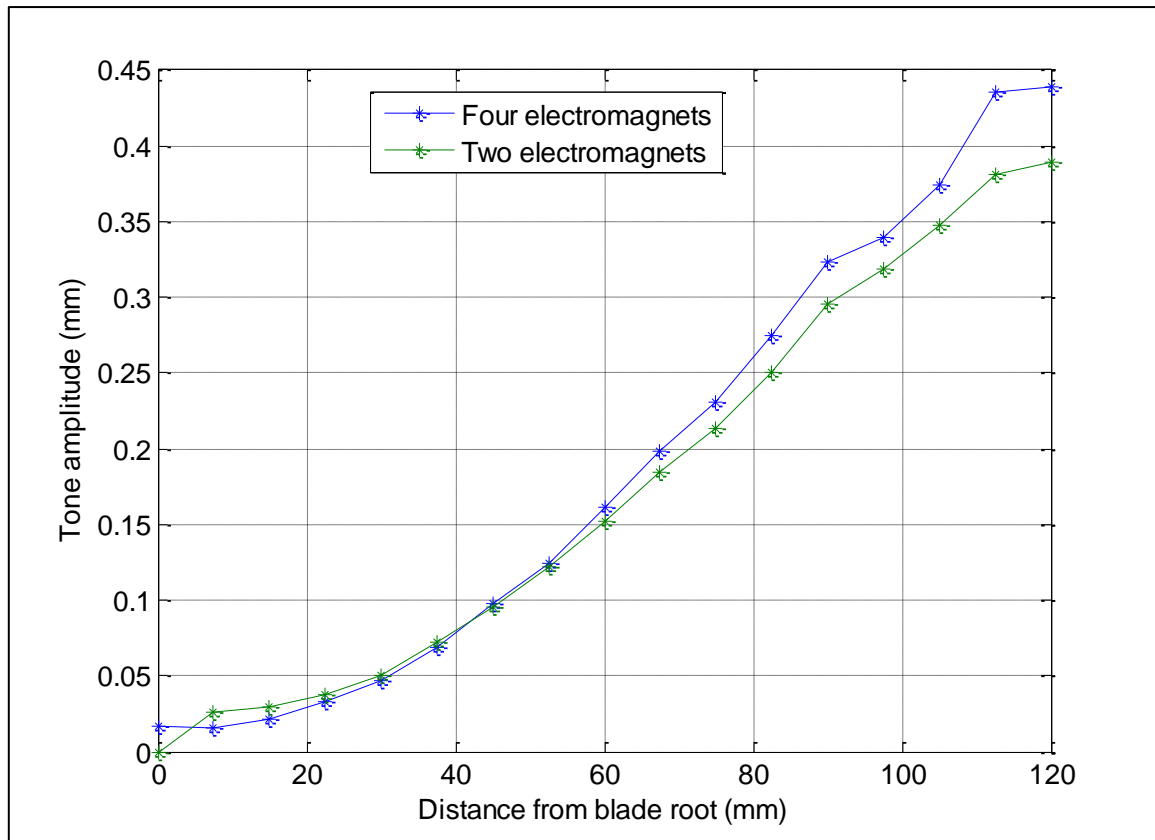


Figure 55: Tone amplitude variation

In the case of out-of-plane blade vibration similar to the blisk first bending mode, a smooth increase in the tone amplitude is expected from blade root to blade tip if there are no irregularities along the blade.

From Figure 55, it can be observed that the amplitudes of the measured signals increase moving along the blade. Between 80 mm and 100 mm however, the variation is not a smooth increase. This location corresponds to the distance from the blade roots where the electromagnets were mounted. Zero tone amplitude for a point closest to the root of the blade (two electromagnets excitation results) illustrates that excitation using two electromagnets could not give enough response for that point. This is noticed in the results presented below as well.

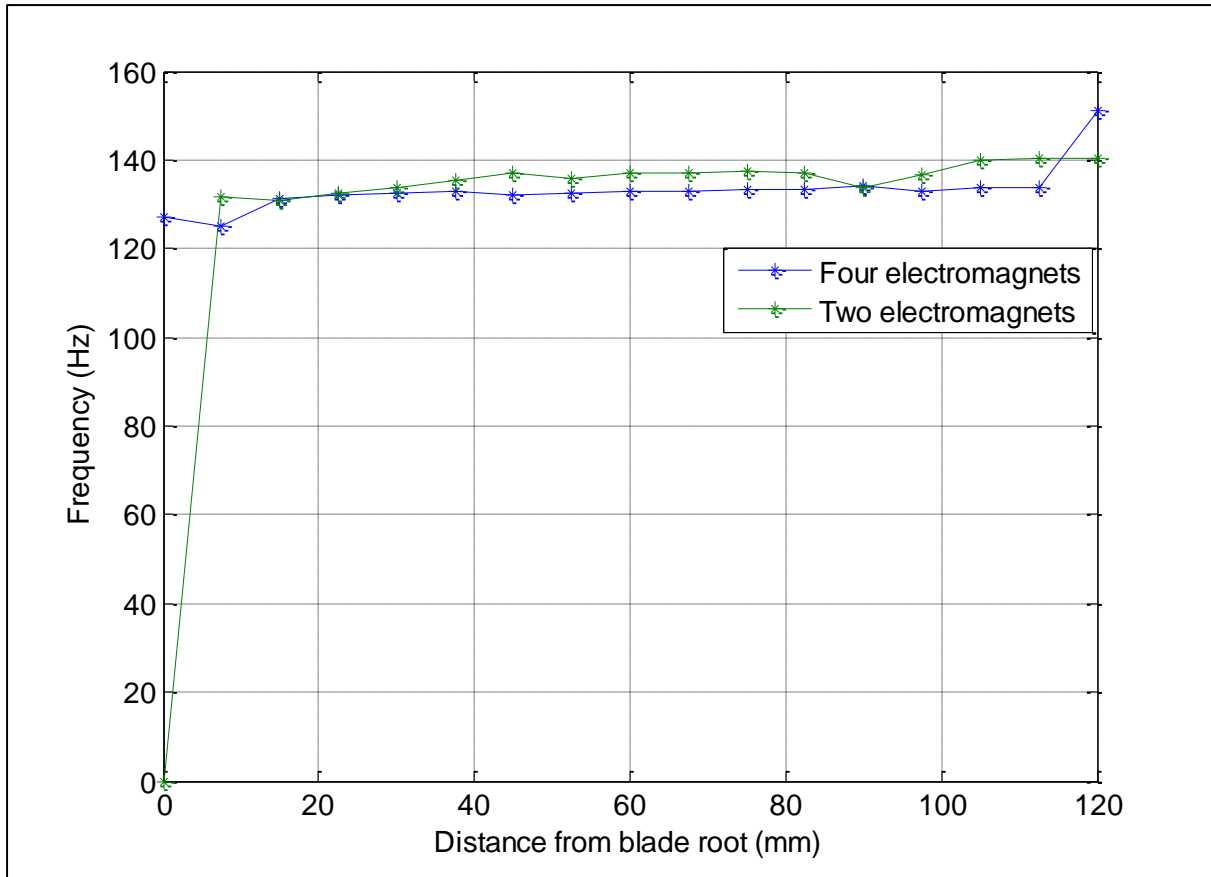
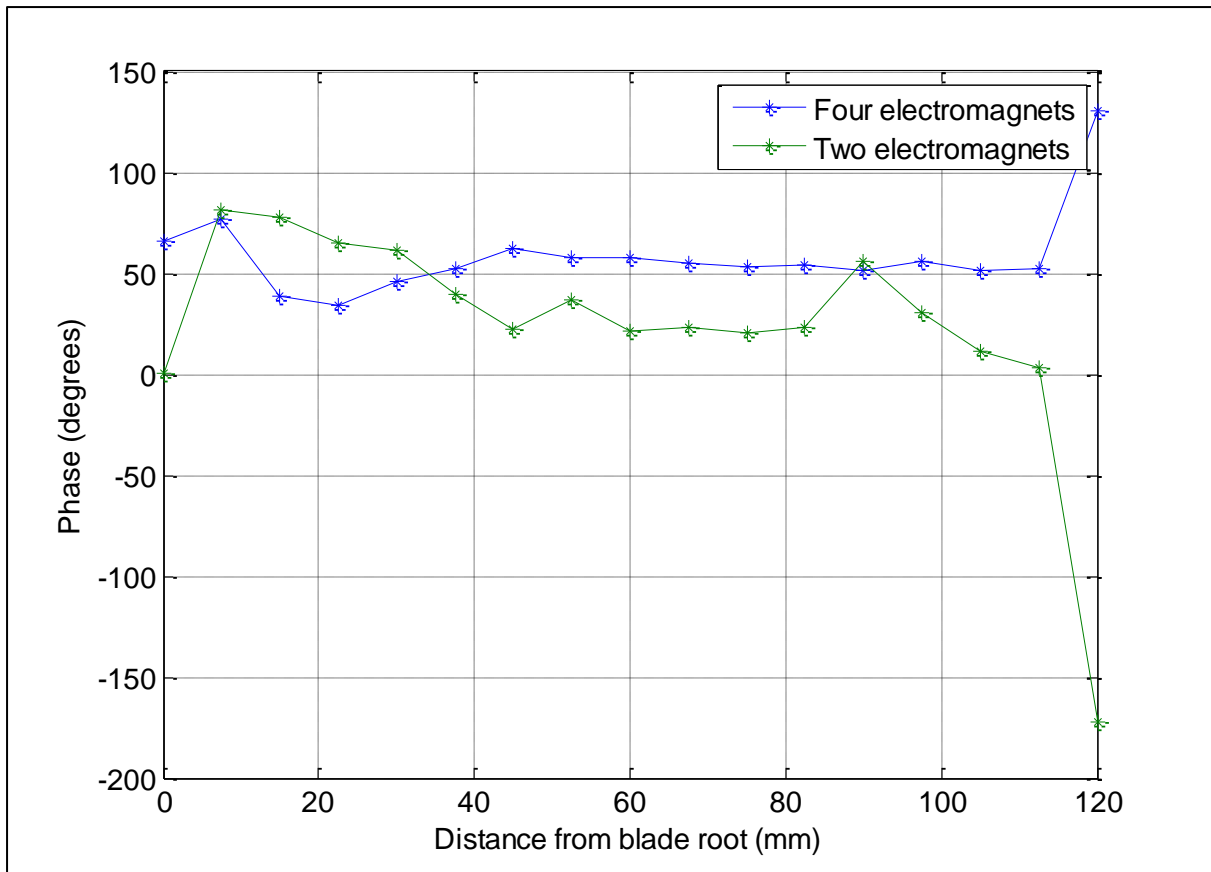


Figure 56: Peak frequency variation

As for the frequency, a similar out-of-plane blade vibration frequency is expected for all points along the blade. From Figure 56, it can be observed that the frequencies of the signals are fairly constant, but between 80 mm and 100 mm, a noticeable drop of about 3.4 Hz in the frequency occurred when two electromagnets were being used. Again, two electromagnets could not excite the blades enough for apparent responses for the point closest to the root of the blades



**Figure 57: Peak frequency phase variation**

Figure 57 shows discontinuities in phase variations at a number of locations, 80 – 100 mm included. The discontinuity at 80 – 100 mm is more noticeable for the two electromagnets excitation case.

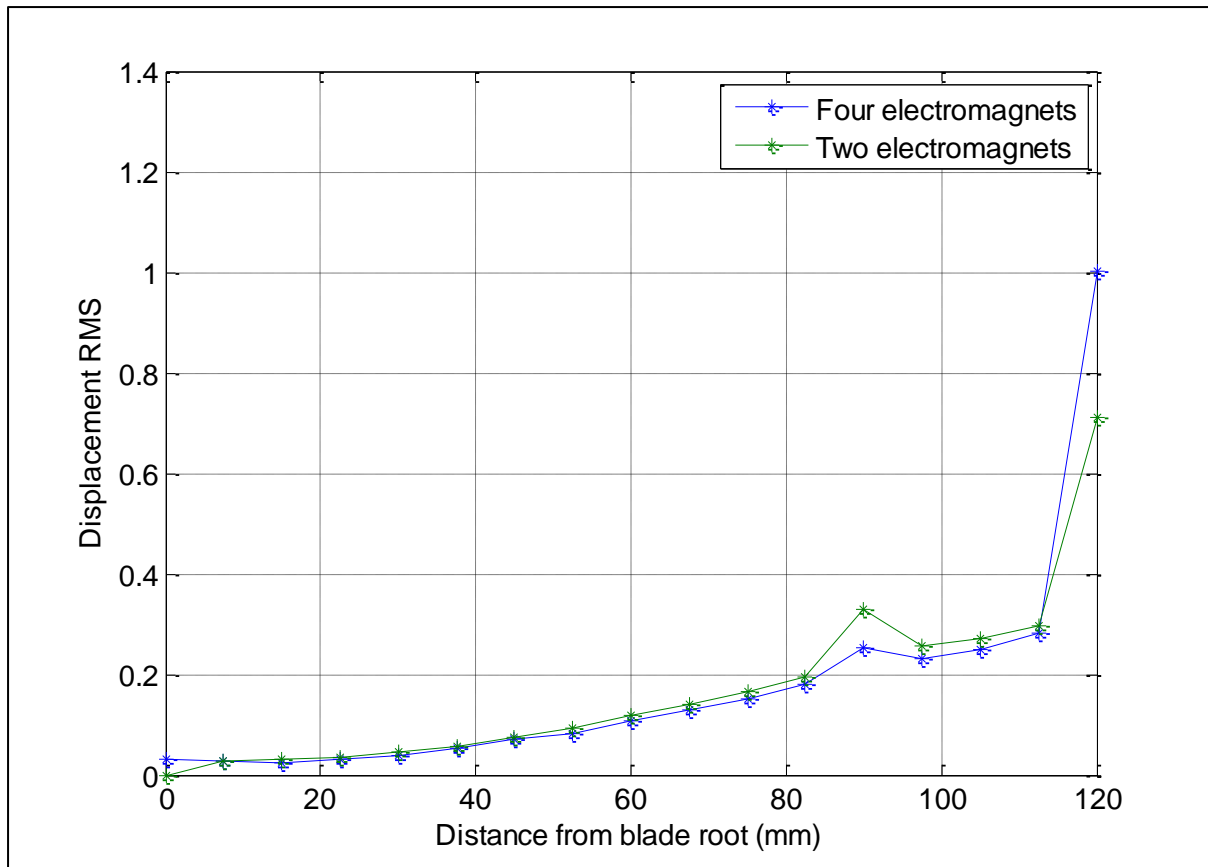


**Figure 58: Displacement profiles RMS values**

Figure 58 shows that the noticed discontinuity between 80 mm and 100 mm from root of blade is more apparent when RMS values of the signals were being considered. Similar to tone amplitude variation, it is expected that the RMS values of the out-of-plane displacement signals increase smoothly from root to tip of blades in the case of no damage. For an ODS similar to the first bending mode, the out-of-plane displacements obviously become more significant as one moves from the root to the tip of the blades.

From the results presented above, it is clear that the localized excitation of the blades resulted in irregularities in the responses of various points along the blades. Thus 3DPT was able to locate where along the blades the excitation was being implemented. Even though this was not damage, it did alter the blade local properties and thus the responses at those locations, something which is similar to the way damage is expected to affect blade response properties - locally. In the presence of a crack in a blade, the local material properties are expected to change. This will be a combination of mass and stiffness reduction, although stiffness reduction will generally be more apparent. The localized nature of damage in a blade and how it affects responses of points along a blade can thus be analysed by investigating the same localized nature of excitation of stiff blades using small electromagnets.

#### **4.4 USE OF ODSs TO DETECT IRREGULARITIES ALONG BLADES**

As mentioned in section 1.2.4a of the literature review, an approach to localize damage in cantilever beams by using ODSs and mode shapes has been proposed by Asnaashari & Sinha (2014). With displacements or accelerations measured simultaneously along a

damaged beam, these authors were able to localize damage by calculating the Residual-Operational Deflection Shape (R-ODS). As an extension of this work to rotating turbomachinery blades, and using non-contact full-field 3DPTDIC measurements instead of data from accelerometers, the applicability of the same approach for detecting irregularities along blades of a turbomachine due to localized excitation can be investigated.

Considering that scenario, Asnaashari & Sinha (2014) approach was then implemented to detect the 'damage' in the blades. R-ODSs were determined from the RMS values, amplitudes, frequencies and phases of the response signals of the points along the blade. Figures 59 to 62 show the results obtained.

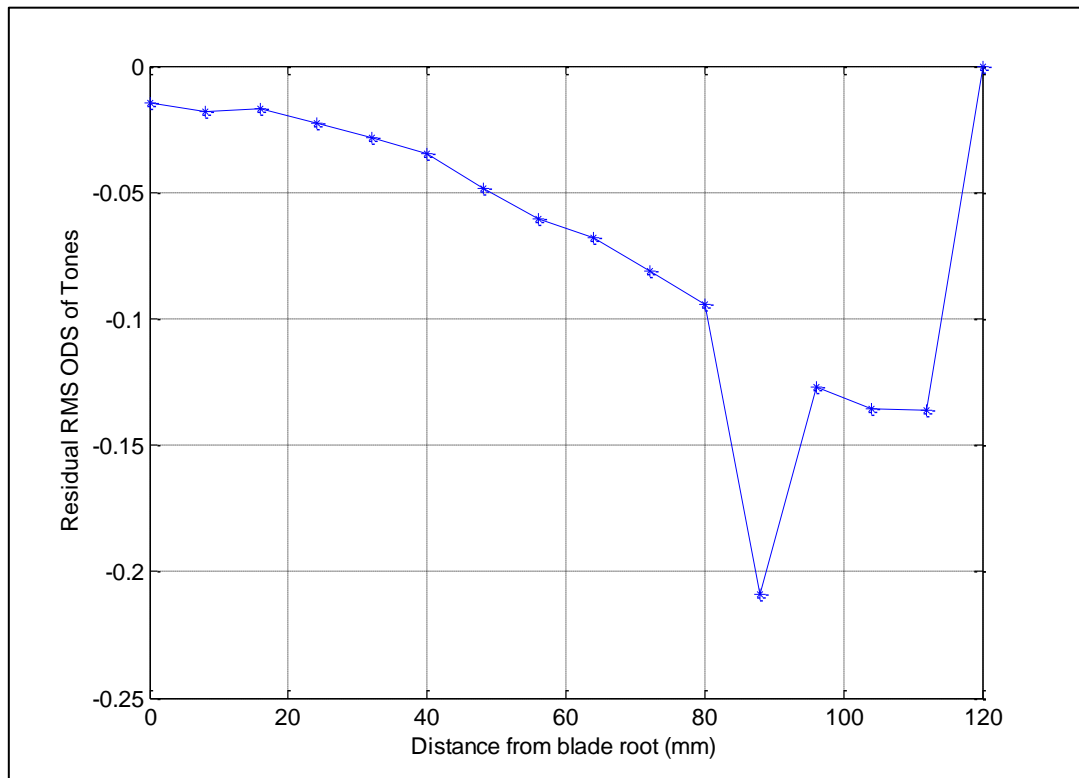


Figure 59: Damage as indicated by signal RMS value variation

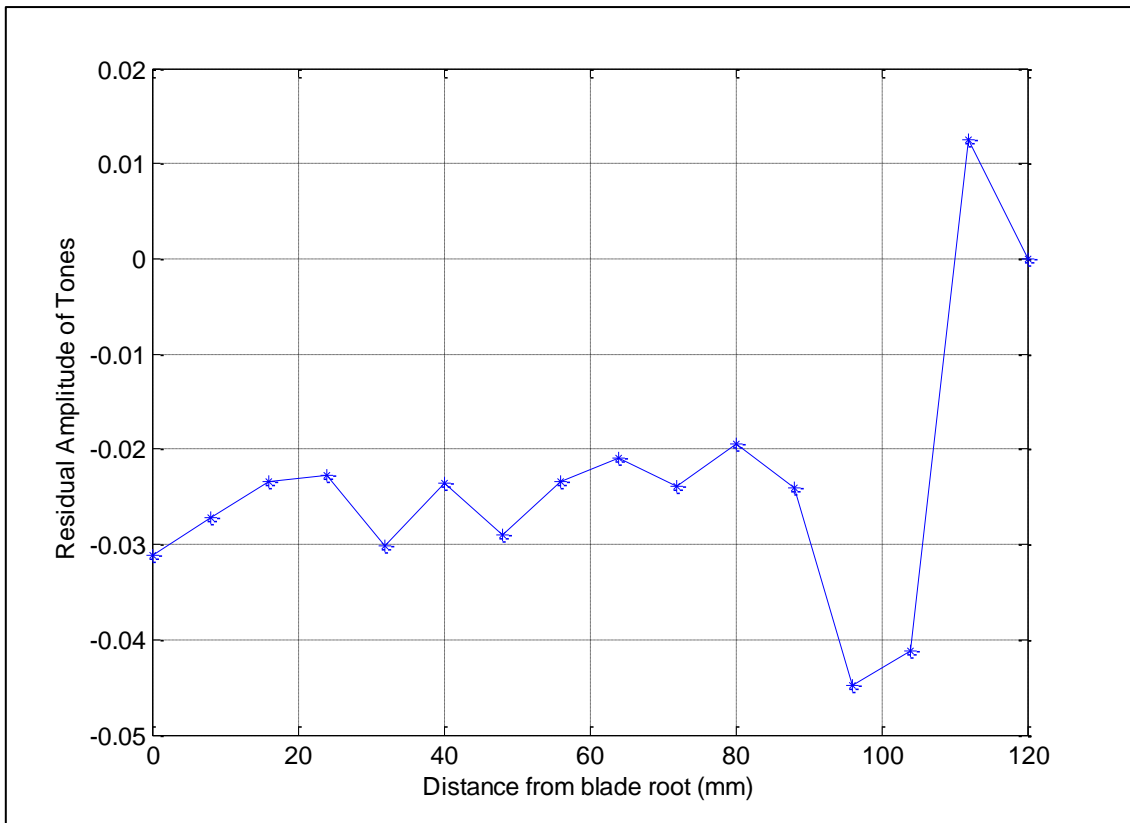


Figure 60: Damage as indicated by signal amplitude variation

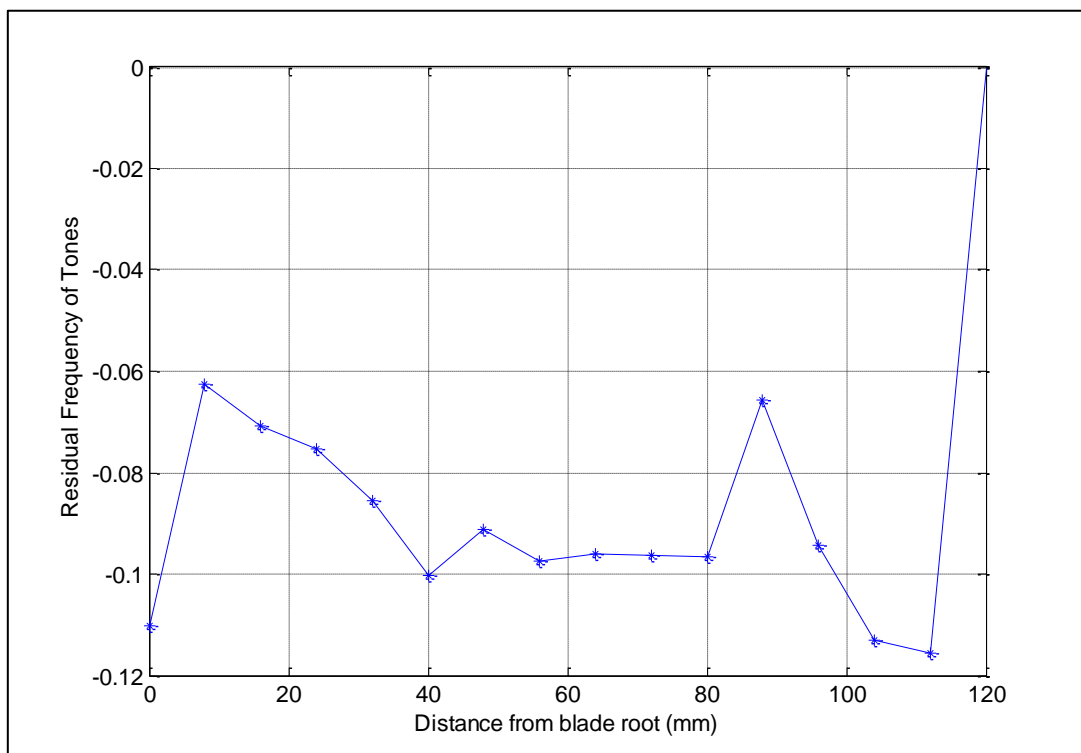
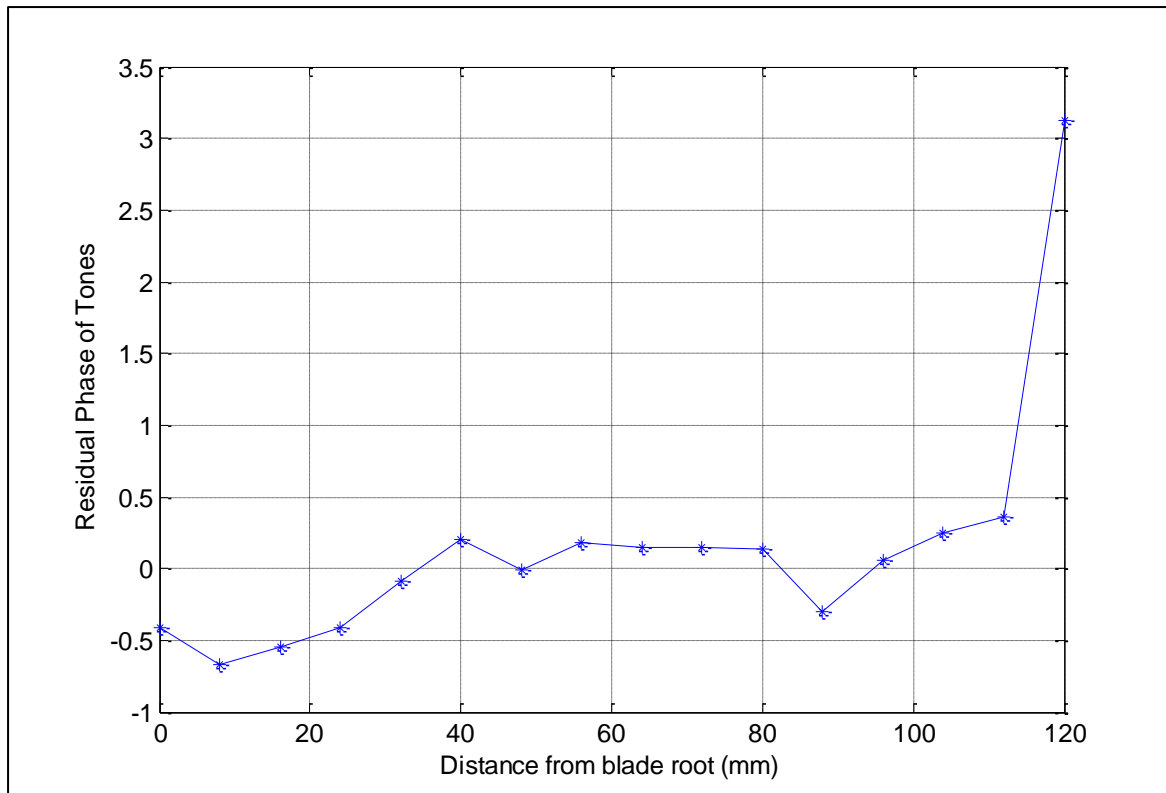


Figure 61: Damage as indicated by signal frequency variation



**Figure 62: Damage as indicated by signal phase variation**

The figures above illustrate that photogrammetry can in fact be used to detect irregularities in the responses captured along rotating turbine blades. These irregularities are exactly what one would expect in the presence of damage. R-ODSs calculated from displacement signals RMS values and amplitudes tend to localize these irregularities better than those from the frequency and phase signals. At 90 mm from blade root, all different signal properties investigated indicated the irregularity due to the localized excitation.

From the results presented in this chapter, damage investigation through the use of ODSs can be implemented for rotating turbomachinery blades. This can be better done using a non-contact full-field measurement technique, photogrammetry, since the effects of contact measurement techniques can be eliminated, and results easily captured for a number of points along a blade simultaneously. Through the use of a combination of these different signal properties, more robust approaches can be used to accurately localize blade irregularities, in cases where there is actual damage in the blades.

## CHAPTER 5: CONCLUSIONS AND RECOMMENDATIONS

### 5.1 CONCLUSIONS

The focus of this study was to evaluate optical non-contact methods for online turbomachinery blade vibration analysis. Validation of photogrammetry measurements using another non-contact measurement technique was necessary. The applicability of photogrammetry as a measurement technique for characterizing the dynamics of a simple blisk was also investigated.

TLDV was successfully implemented to track a specific point on a blade of the rotating blisk. This made it possible to capture the out-of-plane motion of that specific point on the blade. Misalignments between the laser scanning head and the plane of the blisk were investigated and successfully compensated for to obtain accurate displacement measurements.

To establish the correlation between the TLDV and photogrammetry, a scanning LDV laser spot focused on a rotating blade was tracked using high speed cameras. Good correlation between the two non-contact methods was established both in the time and frequency domain. Discrepancies that could have been introduced if contact methods were to be used to establish the integrity of 3DPT results were avoided. Variations in the results captured using the two non-contact techniques were attributed to differences in the degree of misalignments of the separate systems to the plane of the blisk, differences in the noise levels of the captured data due to different sampling frequencies, differences in systems noise floors, and also differences in the responses of the separate systems to the same external trigger signal.

3DPT was then applied to the test rotor. The blades were excited at resonant frequencies and various out-of-plane mode shapes of the blades could be captured and animated using PONTOS. The first and second bending modes were easily identified visually from the software results. For this investigation, the number of out-of-plane bending modes that could be captured was limited to two, as a maximum camera frame rate of 3600 FPS could be set, and modal frequencies for the higher bending modes were greater than half this frame rate.

The effect of the localized nature of small electromagnets form of blade excitation was investigated using ODSs displacement profiles for points along a blade. Irregularities in variations in response characteristics of the different points were successfully captured using 3DPT. The localized nature of the excitation was then related to the expected localized nature of practical damage in blades such as cracks. A damage detection technique developed for non-rotating cantilever beams using a contact measurement technique was successfully implemented for rotating turbomachinery blades, using measurements from 3DPT. It was then concluded that photogrammetry can be used in conjunction with ODSs to detect and localize damage in rotating turbine blades.

From this study, the two optical measurement techniques can be successfully used to investigate the dynamics of turbomachinery blades. They are however largely limited to a laboratory environment, where the information captured is just as useful, for validating other more robust non-contact sensors for industrial use such as continuous microwave proximity

sensors. Wind turbines and helicopter rotor blades can still be analysed, but turbine blades present problems such as very limited line of sight.

## 5.2 RECOMMENDATIONS AND FUTURE WORK

One of the issues encountered when conducting this research was that the blades were too stiff for the responses to be captured easily. In designing the blisk, the aim was to develop a structure simple enough for developing working vibration analysis methods. The goal was to ensure that there were as few uncertainties in the captured results as possible. It is recommended that for further investigations, blisks that can be sufficiently excited are used. This will enhance the quality of the data captured, which will in turn result in the development of better approaches to analyse the data. These approaches can then be used to investigate turbomachines for condition monitoring purposes.

When performing damage detection using photogrammetry, it is recommended that non-localized excitation techniques be used, since electromagnets clearly affect the captured data. Including a stagger angle and some form of blade twist to enhance the aerodynamic effects on the blades can be considered. Using electromagnets extending over the entire blade length is also a viable option. Investigating the robustness of 3DPT -ODS damage detection and characterization in online blades when actual damage has been introduced can be done as an extension of this work.

Future work in photogrammetry and turbomachinery blades can be focused on applying the technique to analysing twisted blades and blades that have a stagger angle. Modal expansion strategies such as System Equivalent Reduction\Expansion Procedures can be implemented to obtain full-field FE ODSs of the blades from the limited photogrammetry measurements, since it will not be possible to capture the entire blade surfaces in this case. Using the DIC data, better FEMU can also be done for blades subjected to other excitation scenarios such as impact loading similar to that induced by bird strikes, from which damage development and progression models can be developed. Thus as a next step to damage detection and localization, damage severity quantification and blade remaining life can be investigated using photogrammetry.

## REFERENCES

- Alberti, A, Nigrelli, V & Pasta, S 2008. Surface measurement by digital image correlation technique. *Advanced Engineering*. 2(2):167–176.
- Asgari, B, Osman, SA & Adnan, A 2013. Sensitivity Analysis of the Influence of Structural Parameters on Dynamic Behaviour of Highly Redundant Cable-Stayed Bridges. *Advances in Civil Engineering*. 2013:1–11.
- Asnaashari, E & Sinha, JK 2014. Development of residual operational deflection shape for crack detection in structures. *Mechanical Systems and Signal Processing*. 43(1-2):113–123.
- Avitabile, P, Niezrecki, C, Helfrick, M, Warren, C & Pingle, P 2010. Noncontact Measurement Techniques for Model Correlation. *Sound & Vibration*. 44(January):8–12.
- Avitabile, P, Baqersad, J & Niezrecki, C 2014. Using digital image correlation and three dimensional point tracking in conjunction with real time operating data expansion techniques to predict full-field dynamic strain. In *AIP Conference Proceedings*. V. 1600. American Institute of Physics Inc. 3–22.
- Castellini, P & Paone, N 2000. Development of the tracking laser vibrometer: Performance and uncertainty analysis. *Review of Scientific Instruments*. 71(12):4639.
- Castellini, P, Martarelli, M & Tomasini, E 2006. Laser Doppler Vibrometry: Development of advanced solutions answering to technology's needs. *Mechanical Systems and Signal Processing*. 20:1265–1285.
- Chiariotti, P, Martarelli, M & Revel, GM 2014. Exploiting continuous scanning laser Doppler vibrometry (CSLDV) in time domain correlation methods for noise source identification. *Measurement Science and Technology*. 25(7).
- Chou, JS, Chiu, C-K, Huang, I-K. & Chi, K.-N. 2013. Failure analysis of wind turbine blade under critical wind loads. *Engineering Failure Analysis*. 27:99–118.
- Ciang, CC, Lee, J & Bang, H 2008. Structural health monitoring for a wind turbine system: a review of damage detection methods. *Measurement Science and Technology*. 19(12).
- Crammond, G, Boyd, SW & Dulieu-Barton, JM 2011. Speckle pattern characterisation for high resolution digital image correlation. *Applied Mechanics and Materials*. 70:261–266.
- Crocker, MJ 2007. *Handbook of Noise and Vibration*. Hoboken New York: John Wiley.
- Dantec dynamics.com. 2015. *Q-450 High-Speed DIC Measurement System | High-Speed Q-450 DIC System for Vibration Analysis and Transient Events - Dantec Dynamics*. Available: <http://www.dantecdynamics.com/q-450-high-speed-dic-vibration-analysis-and-transient-events> [2015, January 14].
- Diamond, D 2015. A Novel Technique for Estimating Synchronous Turbomachinery Blade Vibration From Blade Tip Timing Data. University of Pretoria.
- Doebling, SW, Farrar, CR & Prime, MB 1997. A Summary Review of Vibration-Based Damage Identification Methods. *The Shock and Vibration Digest*. 30(2):91–105.

Ewins, DJ 1984. *Modal Testing - Theory and Practice*. Letchworth, Hertfordshire, England: Research Studies Press.

Friswell, M & Mottershead, JE 1995. *Finite Element Model Updating in Structural Dynamics*. Springer Science & Business Media.

Halkon, BJ & Rothberg, SJ 2006a. Vibration measurements using continuous scanning laser vibrometry: Advanced aspects in rotor applications. *Mechanical Systems and Signal Processing*. 20(6):1286–1299.

Halkon, BJ & Rothberg, SJ 2006b. Vibration measurements using continuous scanning laser vibrometry: Advanced aspects in rotor applications. *Mechanical Systems and Signal Processing*. 20(6):1286–1299.

Helfrick, MN, Pingle, P, Niezrecki, C & Avitabile, P 2009. Optical Non-contacting Vibration Measurement of Rotating Turbine Blades. *Proceedings of the IMAC-XXVII*. (Dic):1–5.

Javad, JB, Lundstrom, T, Niezrecki, C & Avitabile, P 2013. Measuring the dynamics of operating helicopter rotors and wind turbines using 3D digital stereophotogrammetry. In *Annual Forum Proceedings - AHS International*. V. 3. 2250–2256.

Johansmann, M, Siegmund, G & Pineda, M n.d. *Targeting the Limits of Laser Doppler Vibrometry*. Available:  
[http://www.polytec.com/fileadmin/user\\_uploads/Applications/Data\\_Storage/Documents/LM\\_TP\\_Idema\\_JP\\_2005\\_E.pdf](http://www.polytec.com/fileadmin/user_uploads/Applications/Data_Storage/Documents/LM_TP_Idema_JP_2005_E.pdf) [2015, April 24].

Kumar, S, Roy, N & Ganguli, R 2007. Monitoring low cycle fatigue damage in turbine blade using vibration characteristics. *Mechanical Systems and Signal Processing*. 21:480–501. D

Kumari, S, Satyanarayana, DVV & Srinivas, M 2014. Failure analysis of gas turbine rotor blades. *Engineering Failure Analysis*. 45:234–244.

Kutz, M 2002. *Handbook of Materials Selection*. John Wiley & Sons.

LabVIEW. (2013). Austin Texas: National Instruments.

LeBlanc, B, Niezrecki, C, Avitabile, P, Chen, J & Sherwood, J 2013. Damage detection and full surface characterization of a wind turbine blade using three-dimensional digital image correlation. *Structural Health Monitoring*. 12:430–439.

Lomenzo, RA 1998. Static Misalignment Effects in a Self-Tracking Laser Vibrometry System for Rotating Bladed Disks by Static Misalignment Effects in a Self-Tracking Laser Vibrometry System for Rotating Bladed Disks. Virginia Polytechnic Institute and State University.

Lundstrom, T, Baqersad, J & Niezrecki, C 2013. Using high-speed stereophotogrammetry to collect operating data on a Robinson R44 Helicopter. In *Conference Proceedings of the Society for Experimental Mechanics Series*. V. 6. R. Allemang, J. De Clerck, C. Niezrecki, & A. Wicks, Eds. (Conference Proceedings of the Society for Experimental Mechanics Series). New York, NY: Springer New York. 401–410.

Luyckx, T, Verstraete, M, Karel, DR, Wim, DW, Johan, B & Victor, J 2014. Digital image correlation as a tool for three-dimensional strain analysis in human tendon tissue. *Journal of Experimental Orthopaedics*. 1(7):1–9.

Madhavan, S, Jain, R, Sujatha, C & Sekhar, AS 2014. Vibration based damage detection of rotor blades in a gas turbine engine. *Engineering Failure Analysis*. 46:26–39.

Di Maio, D & Ewins, DJ 2010. Applications of continuous tracking SLDV measurement methods to axially symmetric rotating structures using different excitation methods. *Mechanical Systems and Signal Processing*. 24(8):3013–3036.

Martarelli, M & Ewins, DJ 2006. Continuous scanning laser Doppler vibrometry and speckle noise occurrence. *Mechanical Systems and Signal Processing*. 20(8):2277–2289.

Matlab. (2012). Natick, Massachusetts: MathWorks.

Oberholster, AJ & Heyns, PS 2011. Eulerian laser Doppler vibrometry: Online blade damage identification on a multi-blade test rotor. *Mechanical Systems and Signal Processing*. 25(1):344–359.

Pan, B 2010. Recent Progress in Digital Image Correlation. *Experimental Mechanics*. 51(7):1223–1235.

Photron, FASTCAM SA4 Hardware Manual. Available at: <http://www.afs.enea.it/apruzzes/Videocamera/fastcam/> [Accessed July 1, 2015].

PONTOS. (2008). Braunschweig, Germany: GOM.

Rantatalo, M 2006. Non-contact measurements and modelling of milling machine tool vibrations. Luleå University of Technology.

Rastogi, P Ed. 1997. *Optical Measurement Techniques and Applications*. Artech House.

Rytter, A, Brincker, R & Hansen, LP 1991. Vibration Based Inspection of Civil Engineering Structures. *Bygningstekniske Meddelelser*. 62(4).

Siebert, T, Wood, R & Splitthof, K 2009. High speed image correlation for vibration analysis. *Journal of Physics: Conference Series*. 181.

Wang, W, Mottershead, JE, Siebert, T & Pipino, A 2012. Frequency response functions of shape features from full-field vibration measurements using digital image correlation. *Mechanical Systems and Signal Processing*. 28:333–347.

Warren, C, Niezrecki, C, Avitabile, P & Pingle, P 2011. Comparison of FRF measurements and mode shapes determined using optically image based, laser, and accelerometer measurements. In *Mechanical Systems and Signal Processing*. V. 25. 2191–2202.

Warren, C, Niezrecki, C & Avitabile, P 2011. Optical Non-contacting Vibration Measurement of Rotating Turbine Blades II. In *Society for Experimental Mechanics*. T. Proulx, Ed. (Conference Proceedings of the Society for Experimental Mechanics Series). New York, NY: Springer New York. 39–44.

Yoneyama, S 2006. Lens distortion correction for digital image correlation by measuring rigid body displacement. *Optical Engineering*. 45(2):023602.

Yoneyama, S & Murawasa, G 2012. Digital Image Correlation. In *Life Support Systems*. Available: <http://onlinelibrary.wiley.com/doi/10.1002/9781118578469.ch6/summary> [2013, July 18].

Zappa, E, Mazzoleni, P & Martinmanesh, A 2014. Uncertainty assessment of digital image correlation method in dynamic applications. *Optics and Lasers in Engineering*. 56:140–151.

Zucca, S, Di Maio, D & Ewins, DJ 2012. Measuring the performance of underplatform dampers for turbine blades by rotating laser Doppler Vibrometer. *Mechanical Systems and Signal Processing*. 32:269–281.

## APPENDIX A: MODAL 2 BLISK NATURAL FREQUENCIES AND DAMPING FACTORS

Table 8: Experimental natural frequencies and damping factors

| MODE | FREQUENCY<br>(Hz) | DAMPING FACTOR<br>(%) |
|------|-------------------|-----------------------|
| 1    | 141.59            | 0.22                  |
| 2    | 199.74            | 0.14                  |
| 3    | 871.53            | 0.06                  |
| 4    | 896.3             | 0.05                  |
| 5    | 1084.02           | 0.04                  |
| 6    | 1409.45           | 0.04                  |
| 7    | 1423.28           | 0.04                  |
| 8    | 1519.39           | 0.07                  |
| 9    | 1524.59           | 0.05                  |
| 10   | 2397.37           | 0.04                  |
| 11   | 2414.68           | 0.03                  |
| 12   | 2423.48           | 0.04                  |
| 13   | 2446.33           | 0.04                  |
| 14   | 2459.93           | 0.04                  |
| 15   | 2503.75           | 0.08                  |
| 16   | 3349.67           | 0.02                  |
| 17   | 3368.18           | 0.01                  |
| 18   | 3383.66           | 0.02                  |
| 19   | 3408.37           | 0.02                  |
| 20   | 4705.44           | 0.05                  |
| 21   | 4731.1            | 0.03                  |
| 22   | 4756.19           | 0.05                  |
| 23   | 4777.82           | 0.04                  |
| 24   | 4815.64           | 0.04                  |

## APPENDIX B: VARIATIONS OF MODE NATURAL FREQUENCIES WITH YOUNG'S MODULUS

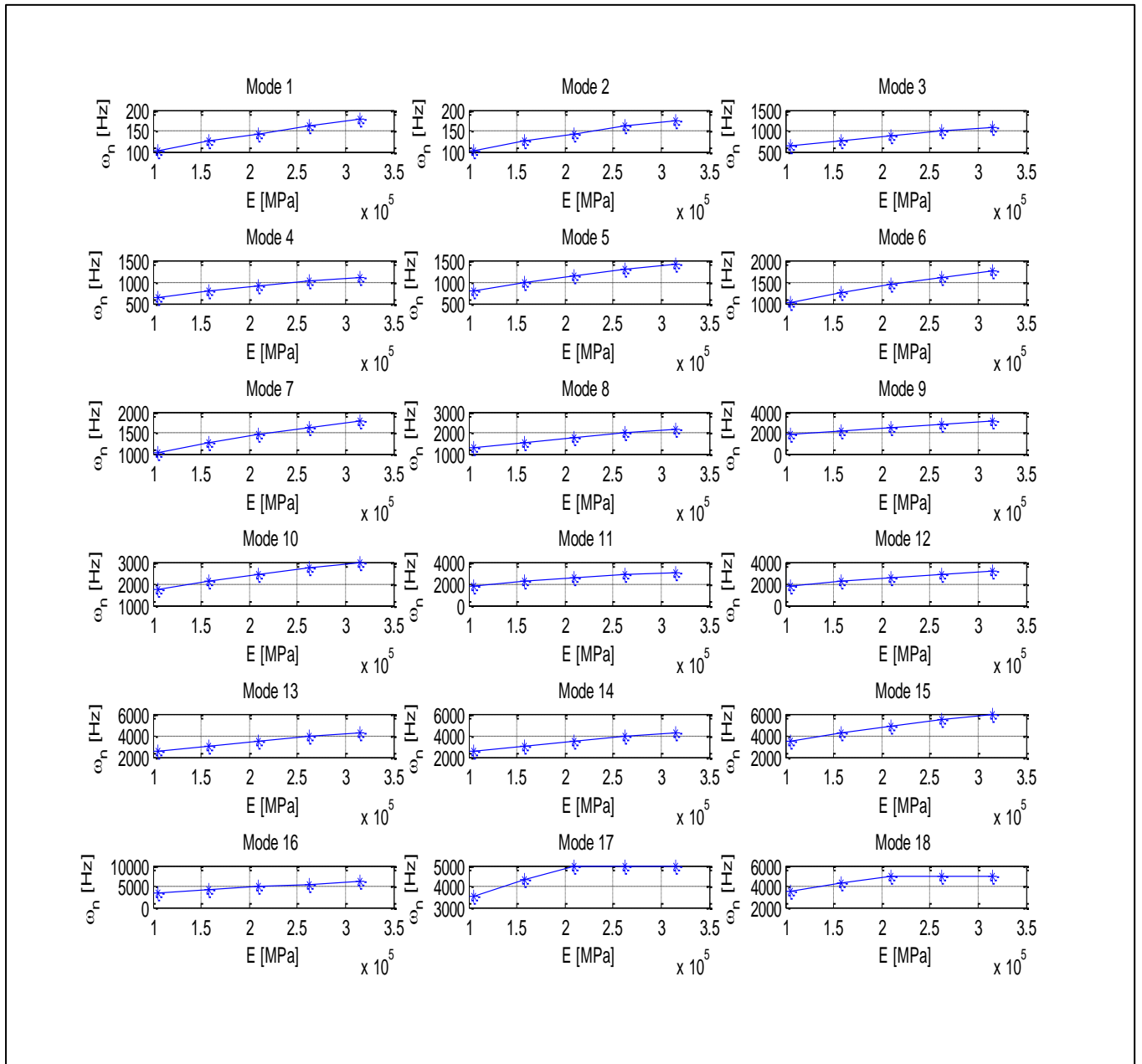


Figure 63: Variations of mode natural frequencies with Young's modulus

## APPENDIX C: VARIATIONS OF MODE NATURAL FREQUENCIES WITH DENSITY

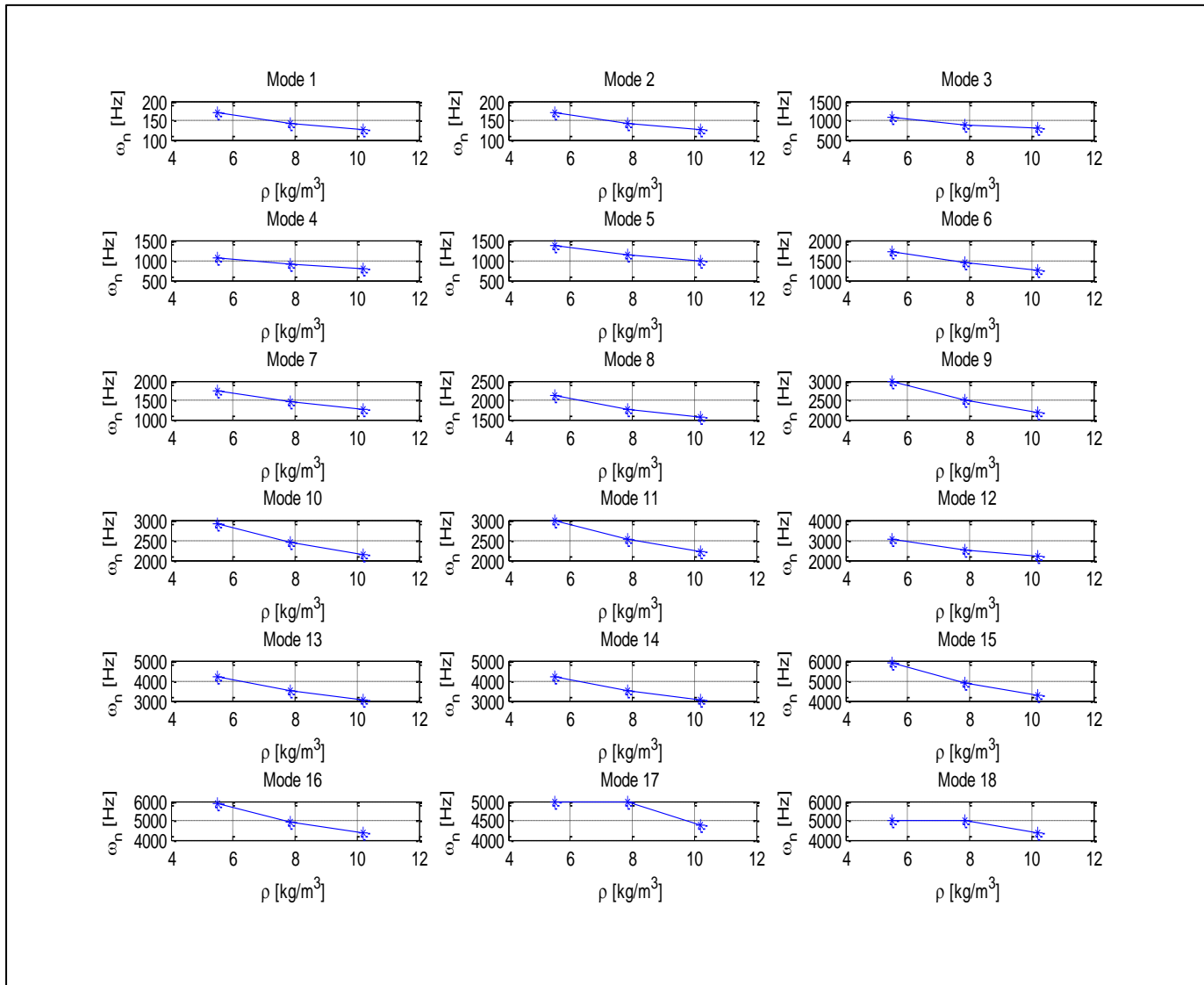


Figure 64: Variations of mode natural frequencies with density

## APPENDIX D: VARIATIONS OF MODE NATURAL FREQUENCIES WITH POISSON'S RATIO

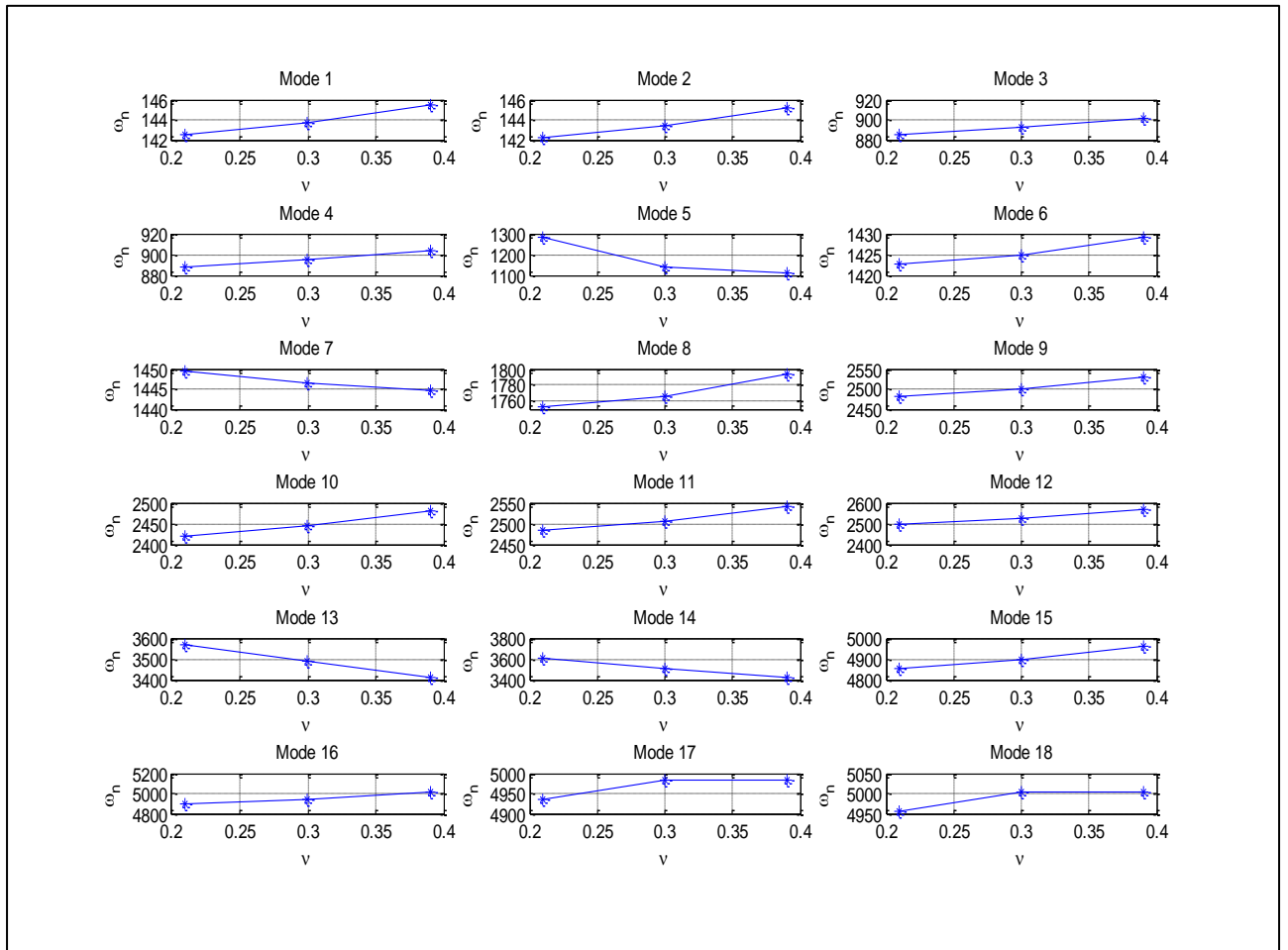


Figure 65: Variations of mode natural frequencies with Poisson's ratio